

Wetting Behaviour of Colloid-Polymer Mixtures in Confinement

Huzaifah Haritsah Abdul Razak

St. Hilda's College
University of Oxford

Supervisor: Professor Dirk G. A. L. Aarts

A thesis submitted for the degree of
Doctor of Philosophy

Trinity Term 2017

Abstract

We study the wetting behaviour of phase-separating colloid-polymer mixtures in confinement. The phase separation is due to the depletion attraction between the colloids mediated by the polymers and bears similarities to ordinary phase separation of oil and water. We use laser scanning confocal microscopy to investigate the behaviour of our colloidal mixture in the vicinity of different substrates, which serve as the confining walls. The glass walls used are chemically modified with two types of polymer, polyacrylamide and chitosan, and we also use clean glass as a reference. We find that the polymer grafting of the surfaces has a pronounced effect on the wetting behaviour. Here, we observe the formation of colloidal liquid droplets, which implies that the coated walls are partially wet. This geometry allows for the determination of the contact angle. The shape of the droplet is theoretically described by the interplay between gravity and interfacial curvature, with the contact angle entering as a boundary condition. The reconstructed interfacial drop profiles are then fitted to the theoretical model to quantitatively study its variation as a function of colloid-polymer state point, properties of the confining wall, and droplet size. We also visually observe Cahn's wetting transition from partial to complete wetting in three series of state points as we move closer to the binodal. This enables us to estimate the wetting transition line in our phase diagram. In addition, we disperse polyacrylamide-coated silica beads into our colloid-polymer mixtures to observe the wetting effects near curved surfaces. We generate theoretical plots based on the conditions of mechanical equilibrium, and compare to the experiments. Our studies shine light on partial wetting phenomena for systems where the interfacial roughness is comparable to the other relevant lengthscales in the system, such as the droplet size or the curvature of the surface.

Declaration

This thesis is submitted for the degree of Doctor of Philosophy in Physical and Theoretical Chemistry at the University of Oxford. No part of this thesis has been accepted or is currently being submitted for any degree, diploma, certificate or other qualification in this University or elsewhere. This thesis is wholly my own work, except where indicated.

To my parents.

And in the loving memories of

my grandfather, Ismail Busu (1923 - 2013).

Contents

Abstract **i**

Declaration **iii**

1 Introduction **1**

1.1 Colloidal systems with non-adsorbing polymers 3

1.2 Interfacial behaviour 5

1.3 Scope of the thesis 6

2 Experimental Systems, Techniques and Analysis **9**

2.1 PMMA-xanthan colloid-polymer mixtures 10

2.2 Surface modification 13

2.2.1 Polyacrylamide coating 13

2.2.2 Chitosan coating 13

2.3 Thermal capillary waves of PMMA-xanthan-water system 14

2.4 Confocal microscopy 19

2.5 Conclusion 23

3 Surface Modification **25**

3.1 Introduction 26

3.1.1 DLVO potential 29

3.1.2 Depletion interaction 32

3.2 Polyacrylamide modification 36
3.2.1 Background 36
3.2.2 Characterisations 39
3.3 Chitosan modification 42
3.3.1 Background 42
3.3.2 Characterisations 45
3.4 Different wettabilities (in confinement and at a single wall) 46
3.5 Conclusion 54

4 Contact Angle Measurement of Colloid-Polymer Mixtures in Confinement 57
4.1 Introduction 58
4.2 Theoretical background 59
4.3 Experimental section 61
4.4 Results and discussion 63
4.5 Conclusion 75

5 Wetting Transition in Colloid-Polymer Mixtures at Polymer-Coated Walls 77
5.1 Partial to complete wetting 78
5.2 Experimental systems 83
5.3 Qualitative results and discussion 85
5.4 Conclusion 92

6 Wetting of Colloid-Polymer Mixtures at Curved Surfaces 93
6.1 Binary liquids behaviour towards spherical particles 94
6.2 Theoretical background 96
6.3 Experimental systems 99
6.4 Results and discussion 101
6.5 Conclusion 105

Summary **109**

Appendix **113**

A Wetting transition in the vicinity of PAA-coated walls 113

B Wetting transition in the vicinity of chitosan-coated walls 113

Bibliography **123**

List of Publications **137**

Acknowledgements **139**

Chapter 1

Introduction

Wetting phenomena myriadly exist in nature and become part of our daily life. Imagine droplets of water beading up on leaves after the rain in spring, as shown in Figure 1.1. From as simple as how a child is fascinated by looking at small rain drops joining other drops to form bigger drops with trails of water on the car's window, the questions, motivations and solutions on wetting are endless. Even from the industrial and technological point of view, wetting plays a critically important role when surface characteristics draw the attention [1, 2]. Manifestations of the phenomena in technological processes are fairly discernible, for instance in oil recovery [3], deposition of pesticides on plant leaves [4], nanoprinting and microfluidics [2, 5], separation and analysis in molecular biology [6, 7, 8], as well as in microphase microfluidics including drug delivery and microreaction systems [9, 10, 11, 12].

A surface is said to be wetting when a liquid spreads on it uniformly to form a thin layer. However, this is not always the case as hydrophobic surfaces may have liquids beading on it. Having this occurrence, we can justify that the specific wettability can be characterised by measuring the contact angle of a liquid deposited on the surface of a solid substrate [13, 14, 15]. The contact angle, θ, is the angle formed by the solid-liquid interface and the liquid-gas interface measured from the side of the liquid. If the contact angle is zero, it is a complete wetting situation where the liquid spreads across the surface of the substrate, forming a thin layer of liquid. When dewetting or drying occurs, the contact angle lies between 90° to 180°. However, if the contact angle lies between 0° to 90°, the phase is known as partial wetting [1, 2]. In a partial wetting state, the area surrounding the droplet is not entirely dry as there is always a microscopically



Figure 1.1: Droplets of water beading up on a leaf after an afternoon rain in spring (picture taken at University Park, Oxford, April 2017).

thin layer of liquid adsorbed on the surface around the droplet. On the other hand, as for complete wetting, this liquid layer is macroscopically thick [2].

The specific contact angle is measured when the wetting system has reached equilibrium, which is a balance between the internal forces of the liquid, the gravity acting on it and the interfacial tension between the three phases in contact. On a flat, smooth and homogeneous surface, this equilibrium contact angle can be related to the three states interfacial tension by Young's equation (Equation 1.1), where γ is the interfacial tension between the phases, with S, L and G indicating the solid, liquid and gas, respectively [16]. From the equation, we can interpret that the contact angle on a solid surface can be altered by modifying the interfacial energy of the solid surface. Hence by performing surface modification, the chemical properties of the solid surface may change, and thus its wetting behaviour [2, 17].

$$\gamma_{SG} = \gamma_{SL} + \gamma_{LG} \cos\theta \tag{1.1}$$

It is also worth noting that the interfacial tension between the liquid and the gas phases can be modified by adding a surfactant to the system. Surfactants are frequently added to reduce

the surface tension, for example in regards to the formation of foams, emulsions or coating layers. This is a common practice in industrial processes, for instance, in food and cosmetics, agricultural chemicals and petroleum industry [18, 19, 20].

By understanding the fundamental aspects of wetting, we can tailor any desired wettability by virtue of industrial and technological applications. The wetting properties of bulk materials can be tuned by nanoscale coatings and many surface treatments have demonstrated the feasibility of these techniques. One of the convenient ways to change the surface chemistry of a substrate is by modifying it with a polymer. This can be done either with physical attachment or covalently bonded onto the surface. The silanisation and immobilisation of polymer monolayers on a solid substrate offer a chemically treated substrate with different wettability [21, 22]. This opens up an opportunity to experimentally study not only complete and partial wetting, but also the transition between the two phenomena. For a more detailed description on the solid substrate surface modification, please refer to Chapter 3 of this thesis.

1.1 Colloidal systems with non-adsorbing polymers

A colloidal system is about size and structure, and is always associated with surfaces or interfaces. It consists of particles termed as a dispersed phase with a dimension between 1 nm to 1 µm, that is dispersed in another phase or solvent, known as the dispersion medium or the continuous phase. Depending on the type of the dispersed phase and the dispersion medium, a colloidal system can be classified into aerosol, emulsion, sol, foam or gel. We recognise these colloids in our daily encounter in the form of fog, milk, mayonnaise, toothpaste, and styrofoam, among others [19, 23, 24].

The size of the particles that forms the dispersed phase is in the submicron region, but still small enough to experience Brownian motion. This random motion is named after the botanist, Robert Brown, who in 1827 discovered the fidgety motion of pollen grains suspended in water observed under the microscope [25]. This phenomenon was later theoretically explained by Einstein from the perspective of the diffusion coefficient, D, and the mobility of Brownian particles, μ, which are related as $D = \mu\ k_B T$, where k_B is Boltzmann constant and T is the absolute temperature of the fluid in which the Brownian particles are immersed [25, 26, 27]. Following the Stokes relation of the mobility for a spherical particle with radius R_c, in a solvent

of viscosity η, the diffusion coefficient can be written as:

$$D = \frac{k_B T}{6\pi\eta R_c}. \tag{1.2}$$

Einstein's theory was based on the justification that if heat is erratic motion of atoms, the thermal motion of fluid molecules must be conveyed to the particles immersed in it, resulting in the jiggling motion of the particles. The particles large enough in size can then be observed directly [27]. This theory was later experimentally proven with the observation under the optical microscope by Perrin [27, 28, 29].

The visible manifestation of the molecular nature of the solvent shines light unto the unprecedented explanation between kinetic theory of gases and colloidal particles under the influence of gravity. The expression of the sedimentation equilibrium that depends on the particle's buoyant mass, the gravitational force, Boltzmann's constant and the absolute temperature exhibits similarity to the distribution of gas molecules. This correlation supports the idea of colloids that behave as big atoms [30, 31]. In contrast to their atom counterparts however, colloidal particles possess smaller diffusion coefficient due to their size that is larger, and this implies the slower dynamic of the particles. At this slow timescale, it is possible to track the particles individually. The advantage of being huge in size also enables the particles to be observable in real time using optical microscopy, and the utilisation of laser scanning confocal microscopy (LSCM) allows the acquisition of three dimensional images. Colloidal particles also demonstrate a distinct difference from their atomic equivalent in terms of their inter-particle interactions. These interactions are considerably easy to be tuned to consequently alter the phase behaviour of the system. This is feasible by changing the electrical charge of the surface by modifying the particle surface, or by the addition of small particles or inert polymers into the colloidal suspensions to induce a depletion interaction [31, 32, 33, 34].

The interactions of two analogous colloids involve the balancing of the long-range Van der Waals attraction interaction and the short-range electrical double layer repulsive force, or widely known as the DLVO theory. The theory that has been beautifully presented by Derjaguin, Landau, Verwey and Overbeek can be held accountable for the stability of colloidal suspensions. The common practice in tuning the DLVO interactions between the colloidal particles is by salt addition into the colloidal suspension. However, it is also interesting to explore another pathway which involves adding free non-adsorbing polymers with a radius of gyration R_g. The

addition of this third component into the colloidal suspension with the colloid radius R_c acts as a depletant that induces the depletion interaction. This interaction can be understood by the rule of thumb that there is a repulsion between the polymer chains and the colloidal particles that arises due to the entropically unfavourable reduction in the free volume of the polymers. This repulsion leads the colloidal particles to be pushed closer together with the formation of the overlap volume region which is restricted to the polymers. The attraction between the colloidal particles through the polymer-colloid repulsion consequently may lead to the phase separation of the colloidal suspension into a colloid-rich polymer-poor phase (colloidal liquid phase) in coexistence with a colloid-poor polymer-rich phase (colloidal gas phase) [9, 31, 35]. Please refer to Chapter 3 of this thesis for further explanation on the DLVO theory and the depletion interaction.

1.2 Interfacial behaviour

Sharing similar phase behaviour with their atomic and molecular counterparts, colloidal suspensions are well-accepted as a good model system to study the interfacial behaviour of the molecular gas-liquid interfaces. Due to their advantages in terms of size and inter-particle interactions, colloids display larger timescale that make it possible to visually observe its slower dynamics in real-time and to tune its properties to encourage phase transition.

In the colloid-polymer mixtures, the phase separation of the system happens due to the entropy-driven attraction between the colloids that is mediated by the non-adsorbing polymers. This isotropic fluid that phase-separates into colloidal 'liquid' and 'gas' shows resemblance with the liquid-gas phase transition in atomic and molecular systems. However, due to the larger size of the colloids as compared to atoms or molecules, the colloidal system possesses an ultralow interfacial tension that can be related as:

$$\gamma \sim \frac{\epsilon}{\sigma^2} \sim \frac{k_B T}{d^2}, \tag{1.3}$$

with ϵ the strength of the molecular interactions and σ the diameter of the molecules. As for the colloidal system in which the attraction between colloids is entropic, the ϵ is of the order of $k_B T$. The colloidal particle diameter, d, is in µm, and this gives the colloidal system a lower interfacial tension that is nN/m, as compared to the atomic or molecular interfacial tension of

mN/m [32, 35, 36, 37].

An ultralow interfacial tension leads the colloidal system to open up an opportunity to understand the interface better. As a consequence of a low interfacial tension, there is an increase in the thermal roughness, projected by the thermal capillary waves:

$$L_T = \sqrt{\frac{k_B T}{\gamma}}. \tag{1.4}$$

The interfacial fluctuations that is scaled up to the order of microns from subnanometer allows the characterisations of the colloid-polymer system to be visually observed with optical microscopy [32]. Some useful interfacial properties can be obtained from the colloidal systems, such as the characteristic lengthscale of the interface fluctuation parallel to the plane, the capillary length:

$$L_c = \sqrt{\frac{\gamma}{\Delta\rho g}}, \tag{1.5}$$

as well as the typical decay time of the waves, the capillary time:

$$\tau = \frac{L_c \eta}{\gamma}, \tag{1.6}$$

where $\Delta\rho$ is the mass density difference between the two phases, g is the gravitational force and η is the sum of the viscosity of each phase [33, 38].

1.3 Scope of the thesis

In this thesis, we use colloid-polymer mixtures as a model system to study their wetting behaviour at substrates of different wettabilities. This prototype of colloid-polymer mixtures is scrutinised from the perspective of its phase separation and wetting affinity towards substrates modified with two different grafted polymers, as well as a clean glass substrate as a control. We essentially aim at observing the partial wetting behaviour of the mixtures, and understanding the possible interactions in the system, that lead to wetting transitions and variation of the contact angle.

We begin by introducing our colloid-polymer mixtures and the modified substrates that

might have the capability to exhibit partial wetting with the mixtures. We outline the synthesis and preparation of the colloids and polymers used to make up the mixtures. We then analyse the physical properties of the colloids using dynamic light scattering and scanning electron microscope prior to preparation of the colloid-polymer mixtures. We also show the protocols of the surface modification of glass slides using two different types of polymer that act as the confining walls, as well as the preparation of our sample slides. Apart from that, an example of a thermal capillary waves analysis is done to find the capillary length of a mixture that is used for the contact angle measurement in the following chapter. This chapter is incomplete without the mention of the use and basic principles of laser scanning confocal microscope that make all of the experimental observations possible. The confocal images provide qualitative and quantitative analyses for the following chapters.

In Chapter 3, we highlight on the aspects of polymer self-assembly and surface modification techniques used to coat the glass walls in order to change the wetting properties of the substrates. We also give the background of the two different types of polymer used to form a thin polymer monolayer on the substrates. Besides that, we present the physicochemical characterisations to measure the polymer brush thickness and the charge of the polymer coating. To physically probe the success of the coating, we employ our colloid-polymer mixtures to observe the interaction with the modified glass walls. Prior to that, it is in this chapter that we illustrate the possible interactions that might happen in our colloidal systems. We also demonstrate how the depletion mechanism is thought to be the central interaction in our entropy-driven colloid-polymer system. In the final section of this chapter, we review the theoretical and simulation work on the interplay between the colloids and the penetrable hard sphere polymers, and between the entities and a hard wall, as well as an experimental attempt of the theory and simulation. We finally display a promising qualitative observation of our colloid-polymer mixtures in the vicinity of polymer-coated walls with partial wetting behaviour and formation of either colloidal liquid droplets or colloidal gas bubbles that will be the base for further analysis in the following chapters.

Chapter 4 focuses on the contact angle measurement of our colloid-polymer mixtures confined between chemically-modified asymmetric glass walls. We show that as the colloidal liquid phase partially wets the coated walls, colloidal liquid droplets formed enable us to quantitatively measure the contact angle. So, in this chapter, we basically perform the image analysis of the droplets by reconstructing the confocal images we obtain by using an in-house software proto-

col. Prior to that, we come up with a theoretical framework of the shape of the droplet that take into consideration the interplay between gravity and interfacial curvature, with the contact angle fixed as a boundary condition. We demonstrate the fitting of the interfacial drop profiles attained from the reconstructed image to the theoretical model.

In Chapter 5, we explore the possibilities of our colloid-polymer mixtures to exhibit wetting transition phenomena by exploiting the modified walls as the confining walls. We look into the interesting aspect of wetting when we move closer to the critical point, where we observe a transition from partial to complete wetting. We also briefly explain the prediction that has been made about the first order and continuous or critical wetting transition. To experimentally show the phenomena, we present qualitative results of wetting transition that we acquire from confocal images of our colloid-polymer mixtures that are scanned along their dilution lines.

In Chapter 6, we take a step further by modifying silica micro beads and study the wetting behaviour of our colloid-polymer mixtures in the vicinity of the polymer-coated silica particles, as well as clean silica beads as a control. We analyse the deformation of the colloidal liquid and colloidal gas interface by the silica particles existence that sediment to the bottom of the wall. The contact angle formed by the deformation of the interface enables us to quantitatively understand the affinity of the colloidal liquid phase towards the coated and clean silica beads. We come up with a theoretical framework to calculate the contact angle of curved surfaces, and subsequently fit our experimental data to the theory.

In the summary, we conclude the findings that we acquire from the qualitative observations and quantitative measurements of our work. We also give some suggestions on future outlook.

Chapter 2

Experimental Systems, Techniques and Analysis

ABSTRACT

In this chapter, we introduce our colloid-polymer system consisting of PMMA colloids and xanthan polymer to study the wetting behaviour of colloid-polymer mixtures. We look at the interfacial phenomena of the system by thermal capillary waves analysis to determine a number of important interfacial parameters. This system is studied on surface-modified glass walls to understand the wetting behaviour. Two different polymer coatings will be discussed, one of chemically modified chitosan and the other of polyacrylamide. Finally, we will introduce the main technique of the work, which is laser scanning confocal microscopy.

2.1 PMMA-xanthan colloid-polymer mixtures

An aqueous suspension of fluorescently-labelled poly(methyl methacrylate) (PMMA) particles was prepared via the first part of the emulsion polymerisation method presented by Kumacheva et al. [39]. Approximately 0.4 g potassium persulphate (Sigma) was dissolved in 140 ml deionised water at 80 °C under nitrogen atmosphere for 30 min under vigorous stirring. Subsequently, 6 g of methyl methacrylate monomer (Fluka) was added and the mixture was continuously stirred for another hour. The rhodamine dye solution was previously prepared based on the work by Bosma et al. [40] and 0.7 ml of this dye solution was then added to the polymer emulsion. This emulsion was stirred for another hour and left to cool before the PMMA colloids recovery.

A dynamic light scattering (DLS) measurement showed the low polydispersity of the spherical PMMA colloidal particles with a radius of 110 nm. From scanning electron microscope (SEM) images, these colloidal particles were observed to be monodisperse with a diameter of 220 nm (Fig. 2.1). With a density of 1.17 g/mL and refractive index of $n_{PMMA} = 1.49$, these PMMA particles have a refractive index mismatch with the solvent used ($n_{water} = 1.33$), and hence multiple scattering might have an effect on the system. The difference in refractive indices might also influence the Van der Waals interaction between the particles that can lead to irreversible aggregation of the colloidal particles when they are not fully screened. However, the particles are charge-stabilised, and hence irreversible aggregation has not been observed in the system.

A solution of xanthan polymer (SKW Biosystems) with a molecular weight, M_w, of 4.0×10^6 g/mol, radius of gyration, R_g, of 264 nm and persistence length of 120 nm was prepared as described in [41]. 0.2 g of the xanthan powder was stirred in 100 ml deionised water together with 0.1 M NaCl to screen the double layer repulsion, and 2 mM sodium azide (NaN_3) to control bacterial growth. The solution was heated to 85 °C before it was slowly cooled down for further 15 hr under stirring.

The xanthan polymer solution was then added to the PMMA colloidal suspension to form a colloid-polymer phase separating mixture. The coexistence of this colloid-rich polymer-poor phase (liquid phase) and colloid-poor polymer-rich phase (gas phase) was controlled through different state points in the experimental phase diagram as shown in Figure 2.2. The phase diagram was originally constructed by Dr. E. Jamie [42, 43], and we used the phase diagram to esti-

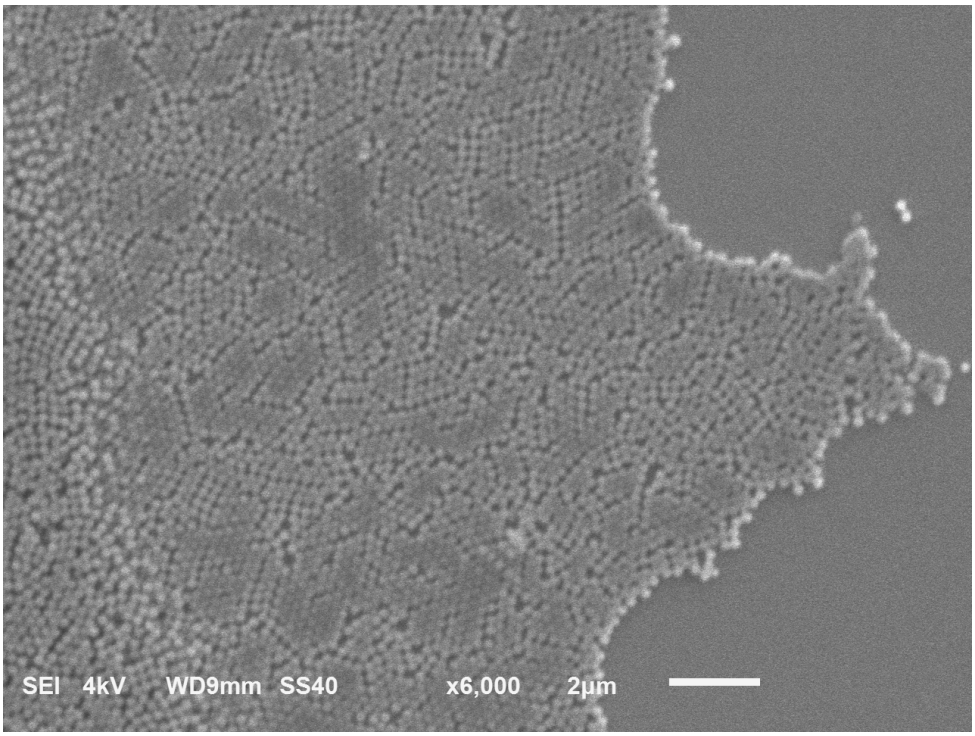


Figure 2.1: Scanning electron microscope (SEM) image of PMMA particles.

mate the suitable fluid-fluid separating state points for our work. We subsequently constructed our own phase diagram based on the concentrations of our samples. The concentrations of the mixtures are given in terms of the volume fractions of the colloid, $\phi_c = \frac{4}{3}\pi R_c^3 n_c$ and polymer, $\phi_p = \frac{4}{3}\pi R_g^3 n_p$, where the R_g of the polymer is treated as the radius of interpenetrable polymer spheres, and n_c and n_p are the number densities of the colloids and polymers, respectively. The phase separation of the colloid-polymer mixtures was observed by visual inspection and under the confocal microscope. Along the dilution line of a state point, we could observe a limiting point where the mixture did not phase-separate as the concentration was decreased. This defined the location of the binodal, and is marked with a solid black line in the phase diagram, see Figure 2.2.

The colloid-polymer phase separation can be directly visualised from its sample bottle. However, to observe it with the confocal microscope, we prepared the sample sandwiched between two glass slides with a sample thickness of about 10 µm such that the system is confined as shown in Figure 2.3. This method of slide preparation is used throughout the experiments, except when stated otherwise.

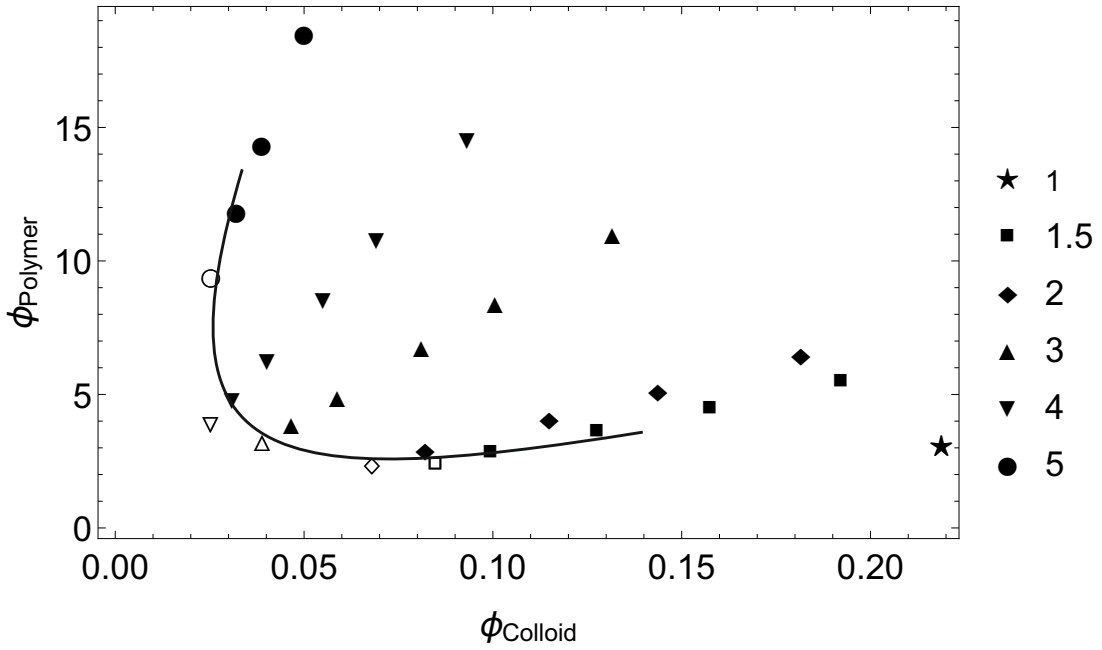


Figure 2.2: Phase diagram of PMMA-xanthan-water system. The filled symbols are the points of the two-phase region, and the open symbols are the points where the samples are not phase separating. The thick black line represents the approximate position of the binodal. The state points are labelled with 1, 1.5, 2, 3, 4 and 5.

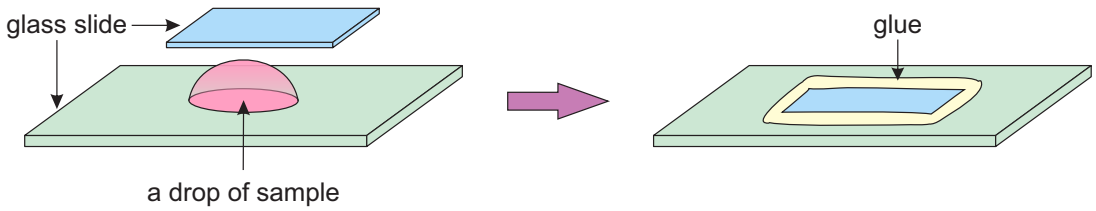


Figure 2.3: A drop of PMMA-xanthan mixture sandwiched between glass slides.

2.2 Surface modification

2.2.1 Polyacrylamide coating

The polyacrylamide (PAA)-modified glass surface was prepared using the method described in [44] and [45]. In the cleaning step, the glass slides were rinsed and sonicated with hot water containing 0.5% detergent (Hellmanex), then they were rinsed with ethanol and finally with 0.1M NaOH. The slides were subsequently soaked in a mixture of 98.5% ethanol, 1% acetic acid and 0.5% of the silane coupling agent, 3-(trimethoxysilyl) propylmethacrylate (TPM) for 15 min to initiate the polymerisation on the glass wall. After a final rinsing, the glass slides were immersed in a 2% w/v aqueous solution of acrylamide for another 15 min. 105 µl of tetramethylethylenediamine (TEMED) and 210 mg of ammonium persulfate (APS) were added to the acrylamide solution to catalyse the polymerisation of the polyacrylamide brush that was covalently attached to the glass surface. The slides were stored in the solution of polyacrylamide and used within weeks. Each slide was rinsed and air-dried immediately before use.

The same method was used to coat 0.1 g silica microbeads (JGC Catalysts & Chemicals Ltd.) of 5 µm in diameter. They were also washed and rinsed repeatedly via centrifugation prior to adding to the colloid-polymer mixtures for further analysis.

2.2.2 Chitosan coating

The chitosan-3-isocyanatopropyltriethoxysilane (chitosan-ICPTES) hybrid was synthesised according to the technique described by Silva et al. [46] prior to its attachment to the glass wall. In the first part of the synthesis, 1 g of chitosan powder was dispersed under stirring in 10 ml of dimethylformamide (DMF) before 1.52 ml of ICPTES added to the dispersion. The flask was sealed and the dispersion was stirred at 105 °C under nitrogen atmosphere for 48 hr. In the second part of the reaction, a mixture of acetic acid-ethanol (AA-EtOH) was added to the dispersion of chitosan with the ratio of ICPTES:AA:EtOH 1:3:6. The mixture was stirred in a sealed flask for 24 hr at room temperature in an inert atmosphere. Subsequently, the hybrid product was recovered by repeated centrifugation with methanol. The solvent was then evaporated and the solid yield was allowed to dry overnight in an oven at 60 °C. Figure 2.4 shows

the proposed scheme for the synthesis of the chitosan-ICPTES hybrid [46]. For polymer attachment to the glass wall, this powder-like functional hybrid was later dissolved in 8% v/v acetic acid at 80 °C and a plasma-cleaned glass slide was immersed in the solution for 3 hr under a low speed stirring. The chitosan-coated glass slide was rinsed with distilled water and air-dried immediately before use.

Further details of both polymer-coated walls will be given in the next chapters.

2.3 Thermal capillary waves of PMMA-xanthan-water system

Thermal capillary waves of the colloid-polymer-water system can be measured to determine a number of important parameters such as the capillary length L_c, the interfacial tension γ and the capillary time τ.

We have prepared a sample mixture at statepoint $\phi_c = 0.04$ and $\phi_p = 14.6$ to observe the fluctuations of the interface. This sample was sealed in a custom made glass cuvette with the viewing glass thickness of approximately 0.15 mm and left undisturbed overnight for it to reach equilibrium in an unconfined environment. The interface fluctuations of the phase separated sample were then imaged for 5000 frames in real time using laser scanning confocal microscope (LSCM).

Figure 2.5(a) shows a snapshot of phase-separated colloid-polymer interface with the fluorescently-labelled colloidal particles making up most of the liquid phase appear bright at the bottom of the system. As marked by the red line, the difference in the pixel intensity allows us to identify the position of the interface fluctuations at equilibrium. This can be done by fitting the intensity profile along the column of pixels using a tangent hyperbolic function to indicate the interface (Fig. 2.5(b)).

From the initial analysis of the intensity profile, we can deduce some quantitative information from the thermal capillary waves by studying its height distribution function, and subsequently through the height correlation functions in both space and time. The height distribution function can be expressed as:

$$g_h(x,t) = \langle [h(x',t') - \bar{h}(t')][h(x'+x,t'+t) - \bar{h}(t'+t)] \rangle \tag{2.1}$$

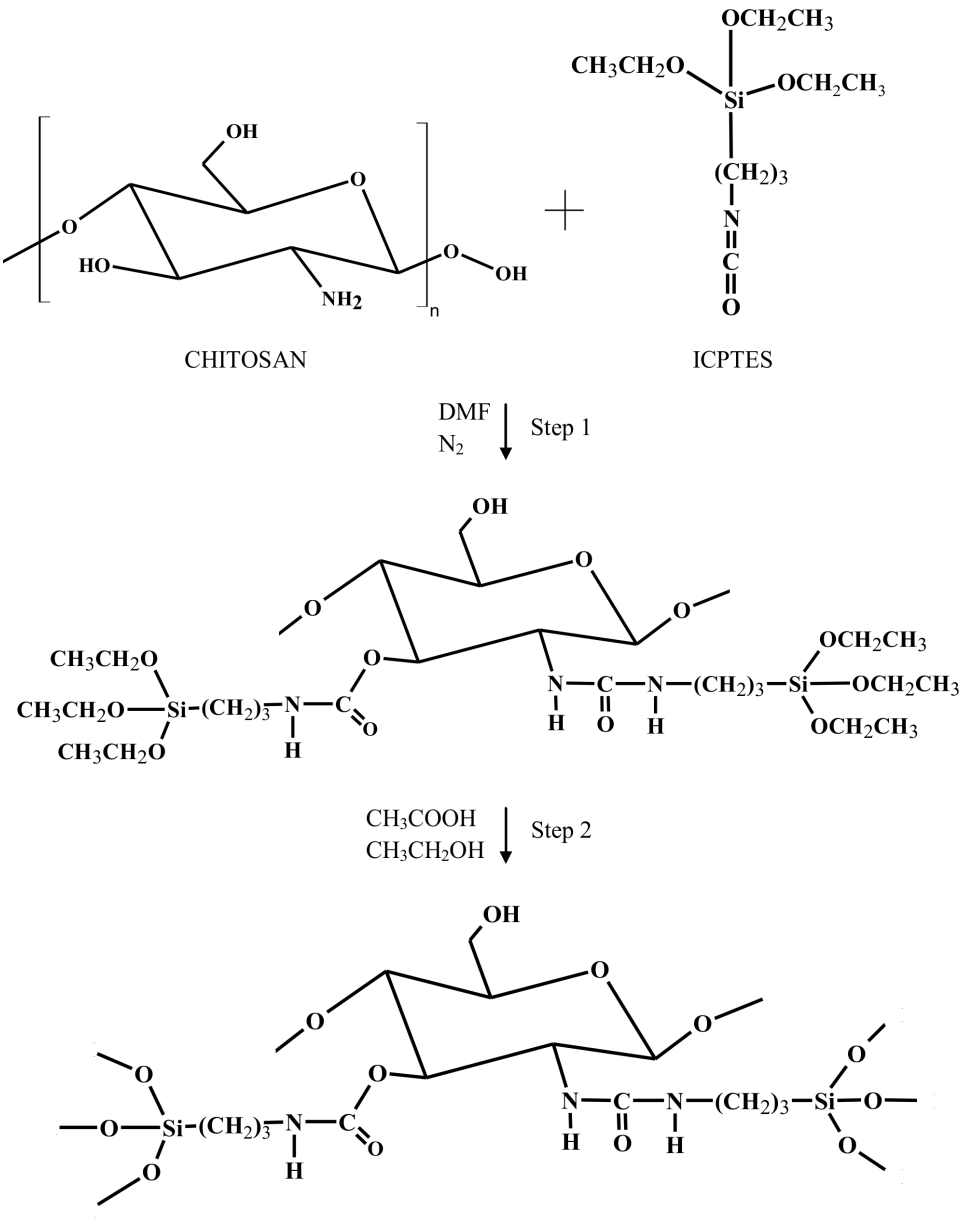


Figure 2.4: Proposed scheme for the synthesis of the chitosan-siloxane hybrids [46].

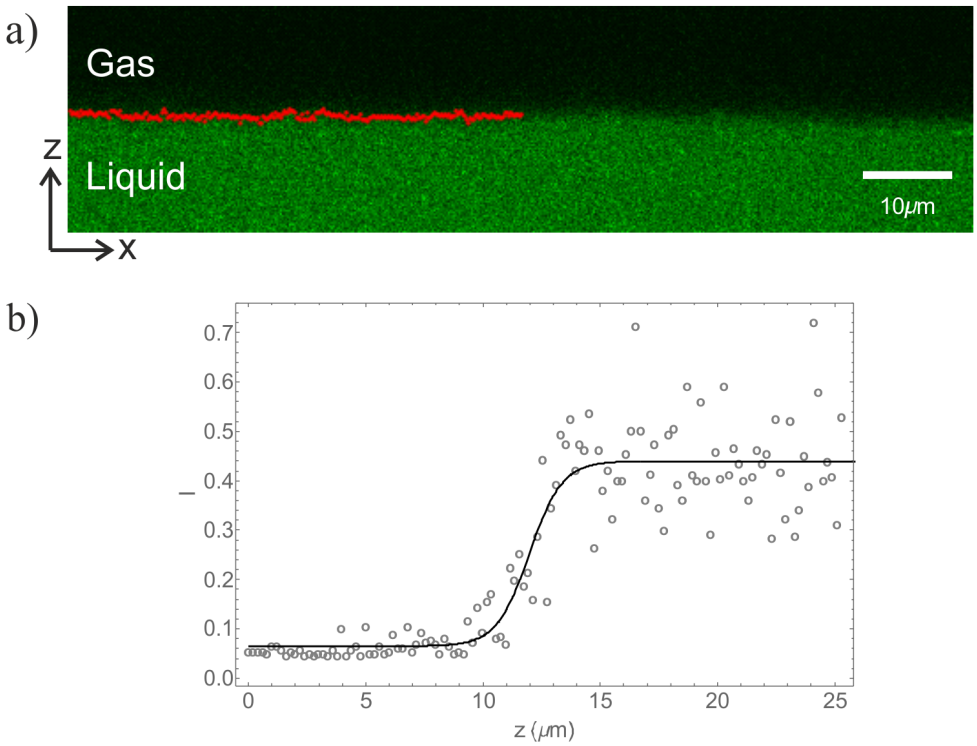


Figure 2.5: (a) An LSCM image of phase-separated colloid-polymer interface. The lower part of it is the colloid-rich polymer-poor (liquid) phase, and the upper part is the colloid-poor polymer-rich (gas) phase. The red line is the position of the interface. (b) Fitting the intensity profile of a column of pixels with a *tanh* function. The intensity is measured from the colloidal gas phase towards the colloidal liquid phase.

where the angle brackets denote averages over primed quantities, x is the coordinate along the interface, and t is the time. (For each frame, the height h is defined with respect to the average height at that time $\bar{h}(t)$, so that it is possible to eliminate any systematic drift in the interface position) [34].

As suggested by von Smoluchowski in 1908, the rough interface that we could observe between two distinct phases (two liquid phases in this case) is related to its thermal motion which gives rise to statistical fluctuations of the local interface position [47]. According to Mandelstam (1913) [48], this rough interface is attributable to the thermally excited capillary waves. The amplitude of these fluctuations is known as the thermal roughness, L_T, and equals $\sqrt{k_B T/\gamma}$ where γ is the interfacial tension between the two liquids, k_B is the Boltzmann constant and T is the absolute temperature. From the capillary wave spectrum that was first derived by Mandelstam, each Fourier component $\mathbf{q}$ of the interface has a mean square amplitude given by:

$$\langle |h_{\mathbf{q}}|^2 \rangle = \frac{k_B T}{\gamma L^2} \frac{1}{q^2 + L_c^{-2}} \tag{2.2}$$

where $\langle |h_{\mathbf{q}}|^2 \rangle$ is the thermal average, L is the lateral system size, q is the absolute value of the wave vector $\mathbf{q}$, and L_c is the capillary length which is the parallel in plane lengthscale of the fluctuations along the interface and defined as:

$$L_c = \sqrt{\frac{\gamma}{\Delta\rho g}} \tag{2.3}$$

where $\Delta\rho$ is the mass density difference between the two phases and g is the gravitational force.

Figure 2.6(a) shows the height distribution of the fluctuations with the open circles representing experimental data fitted to the Gaussian (the full line) as also reported in other work [32, 49]. The width of the distribution reflects the roughness of the interface.

Further derivations of this initial expression also enable us to obtain useful interfacial properties from the height correlation functions in both space and time by Fourier transforming Equation 2.2 to obtain the static and dynamic correlation functions. The static correlation function can be expressed as:

$$g_h(x, 0) = \frac{k_B T}{2\pi\gamma} K_0 \left(\frac{x}{L_c} \right) \tag{2.4}$$

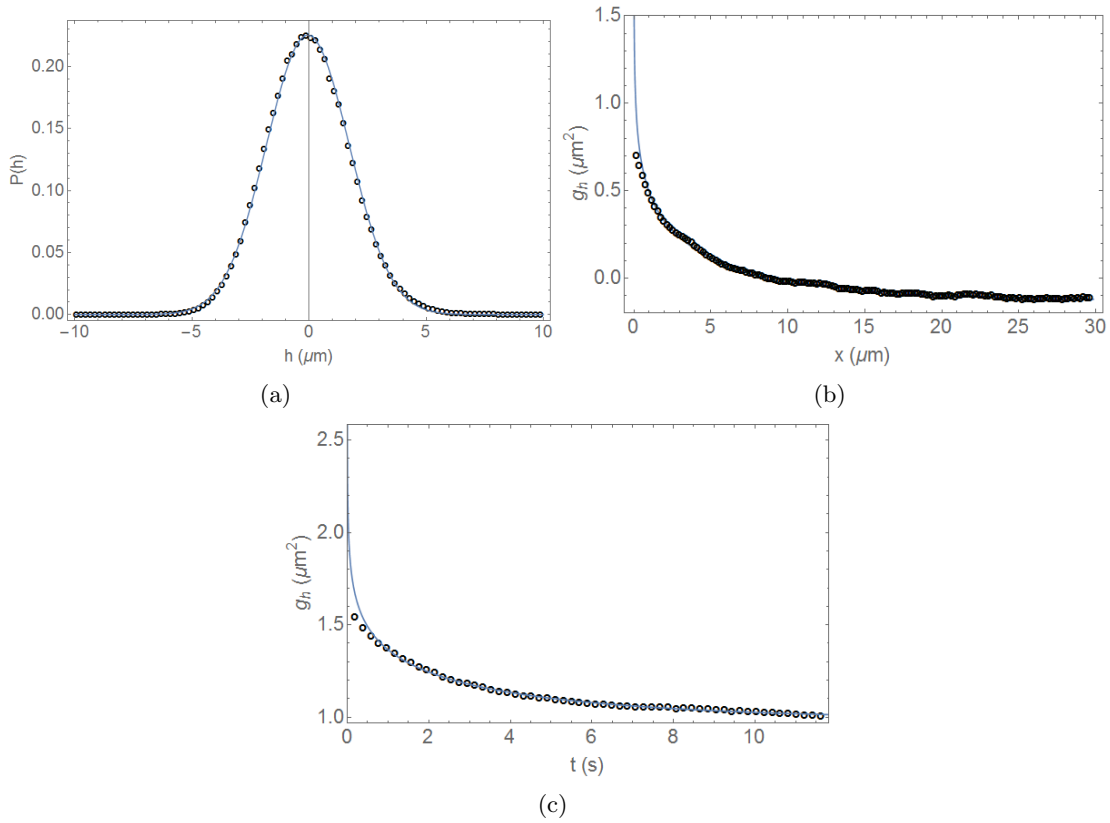


Figure 2.6: (a) Height distribution, (b) static and (c) dynamic correlation functions of the interface fluctuations of the PMMA-xanthan-water system. The open circles represent experimental data, and the full lines in (a) represent a Gaussian fit, and capillary waves theory for (b) static and (c) dynamic correlation function.

where K_0 is the modified Bessel function of the second kind. Figure 2.6(b) shows the result for the static correlation function $g_h(x, t = 0)$. The open circles represent the experimental data and the full line represents the fit to the capillary wave theory from Equation 2.4 which give the interfacial tension of the system to be 71×10^{-9} N/m and capillary length of 12 µm. These fits are similar in the order of magnitude to the previously reported experiments [32, 35, 49, 50].

From the aspect of the fluctuation time, the dynamic correlation function $g_h(x = 0, t)$ can be derived as well. In theory, each mode of the wave vector $\mathbf{q}$ decays exponentially as $\exp[-t/2\tau_q]$ in the overdamped regime with:

$$\tau_q = \tau \frac{qL_c}{1 + q^2 L_c^2}. \tag{2.5}$$

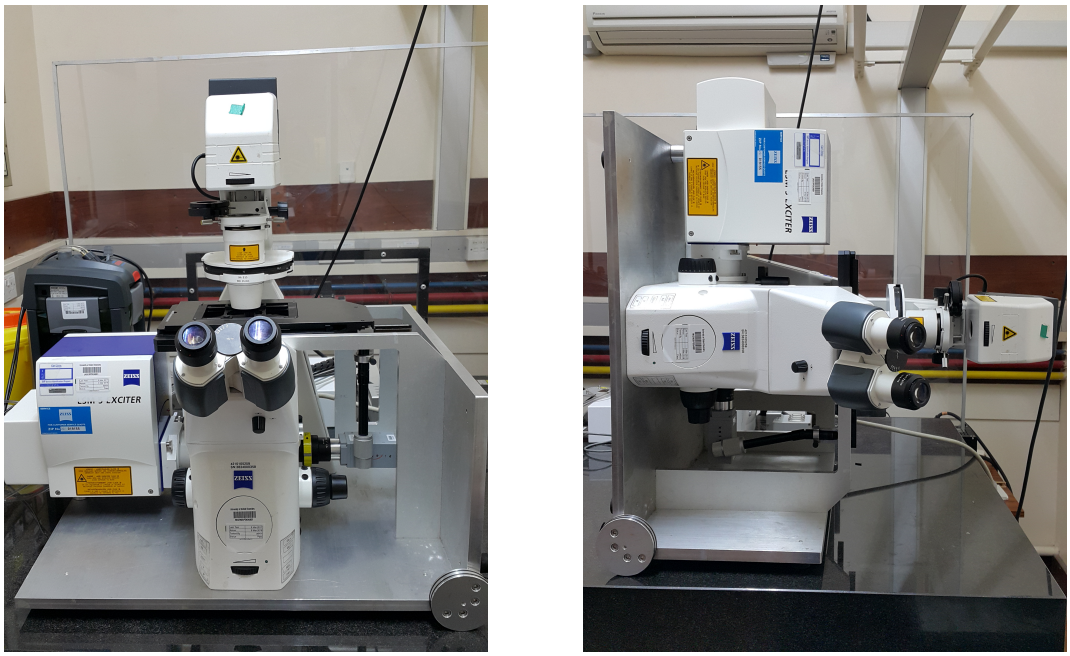
Here, the decay time of the waves, or the capillary time, τ, equals $L_c\eta/\gamma$ and η is the sum of the viscosity of the two phases. By Fourier transforming Equation 2.2, the dynamic correlation function can be expressed as:

$$g_h(0, t) = \frac{k_B T}{(2\pi)^2 \gamma} \int_{\bar{q}_{min}}^{\bar{q}_{max}} \mathrm{d}\bar{q}\, \frac{\bar{q}}{1 + \bar{q}^2}\, e^{-\omega_q t} = \frac{k_B T}{\gamma L^2} K_0 \left(\frac{t}{\tau} \right). \tag{2.6}$$

Figure 2.6(c) shows the experimental results of the dynamic correlation function represented by the open circles, while the full line curve is the fit to the theoretical expression of Equation 2.6. From the fitting, we obtain the interfacial tension to be 93×10^{-9} N/m and the capillary time of 8 s, and it is again comparable to the previous work [32, 35, 49, 50]. Furthermore, the interfacial tension obtained from the static and dynamic measurements lie reasonably close together.

2.4 Confocal microscopy

Microscopy is a very convenient technique to understand the behaviour of our colloidal systems. We observed the morphology and kinetics of phase separation of our colloid-polymer mixtures using a Zeiss Exciter LSM 5 laser scanning confocal microscope (LSCM) with 543 nm laser source. This instrument was fitted to a rolling table which allows the samples to be viewed on a plane perpendicular or parallel to gravity (Fig. 2.7).



(a) (b)

Figure 2.7: Inverted laser scanning confocal microscope positioned to view the sample in the plane (a) perpendicular and (b) parallel, to gravity.

The fundamental principles of optical microscopy involve the transmission of light from the light source through the examined sample with different contrast created by different entities in the sample as the light passes through it. The transmitted light is subsequently focussed by the objective lens onto a detector for recording. This is a very convenient way of analysing samples with objects of a size of the same order as the wavelength of visible light. This then enables real-time and real-space imaging of the specimen. In addition, the ease of sample preparation at room temperature and atmospheric pressure promotes its common usage. However, optically dense samples such as biological specimens and colloidal suspensions are more difficult to be imaged due to multiple scattering from the light that travels through the samples which leads to blurriness of the images [51].

This is where confocal microscopy came into play when Marvin Minsky [52] first invented the principles of the confocal scanning microscope in 1955 when he was attempting to produce clear and sharp images of the unstained brain neural networks while working at Harvard University. This evolution of the optical microscopy greatly reduces the problem of multiple scattering, and hence provides images with better contrast and resolution.

Two major improvements in this system over conventional optical microscopy is the use of

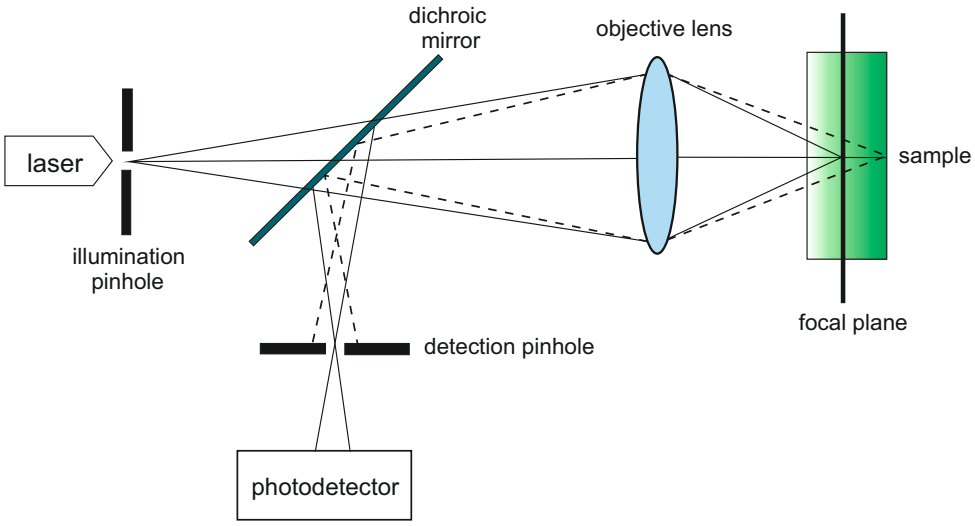


Figure 2.8: Schematic diagram of the confocal optical system. The solid lines indicate the in-focus light path, and the dashed lines indicate the out-of-focus light path [53].

a pinhole to control the signal emitted back from the sample, and the sectioning illumination of the sample to minimise scattered emission. Figure 2.8 depicts the principles of a confocal optical system [53]. A laser source, which is usually used as the illumination light, passes through a pinhole to create a thin laser spot. The light is directed by a dichroic mirror and focussed onto the focal plane within the sample by the objective lens. The sample that is fluorescently labelled gets excited by the laser light and as a result, the fluorophores emit light that is focussed onto the dichroic mirror by the same objective lens. The incoming light is reflected by the dichroic mirror, and only in-focus light passes through a pinhole that is placed in the conjugate focal plane before reaching the photodetector. The out-of-focus light is blocked by the detection pinhole as represented by the dashed line in the diagram. The sectioning of the sample in the xy focal plane allows a complete 2D sample imaging. Combined with the strong illumination from the laser source used, this ability also enables the construction of 3D images from different focal depth scans [51, 54, 55].

The contrast and resolution of the images recorded by confocal microscope are greatly enhanced with the setup of having the light focussed twice by the objective lens. This special feature of confocal microscope over its conventional counterpart can be demonstrated by the *point-spread-function* (PSF). The PSF can be understood as the probability that a photon reaches a certain point in space, which is reaching the detector at a coordinate (ρ,ζ) [56]. The ρ and ζ are dimensionless optical coordinates in the focal plane and along the optical axis

respectively, and correspond to the real distances r and z by:

$$\rho = r(2\pi NA/\lambda) \tag{2.7}$$

$$\zeta = z(2\pi NA^2/n\lambda) \tag{2.8}$$

where λ is the wavelength of the entering light, n is the refractive index of the medium, and NA is the numerical aperture of the objective. NA is defined as $NA = n \sin \alpha$, with α being the half angle of the maximum cone of light that can enter or leave the objective. The corresponding PSF functions are given by:

$$p(\rho, 0) = \left(\frac{2J_1(\rho)}{\rho}\right)^4 \quad \text{PSF for a point in the focal plane} \tag{2.9}$$

$$p(0, \zeta) = \left(\frac{\sin(\zeta/4)}{\zeta/4}\right)^4 \quad \text{PSF for a point along the optical axis} \tag{2.10}$$

where J_1 is the Bessel function of the first kind. Those equations are the square of the PSF of the conventional optical microscope as the incoming light is focussed twice by the same objective lens.

Figure 2.9(a) shows the plot of Equation 2.9 of the confocal point in the focal plane (blue solid line) as compared to the conventional microscope (red dashed line). The distribution patterns are projected by the Airy disk, which is the light intensity distribution of the distance from the axis, and the radius can be quantified by where the PSF first reaches zero. The radius of the Airy disk is related to the wavelength of the laser and the numerical aperture of the objective lens, with smaller aperture giving larger PSF and bigger radius size, and thus decreasing the resolution. It can clearly be seen from the smaller width of the confocal microscopy radial PSF as compared to conventional microscopy, as well as negligible subsidiary peaks, implying that the resolution is significantly increased in the confocal microscope as the light is focussed more on the central peak.

The ability of a microscope to distinguish two luminous objects at a certain distance determines the level of resolution. This is measured by the Rayleigh criterion, which states that the two points can be resolved when the maximum of one point is just above the first minimum of the second point, and this can be achieved when the intensity drop between the maxima is at least 26%. Figure 2.9(b) shows the PSF intensity profiles for both the confocal and optical

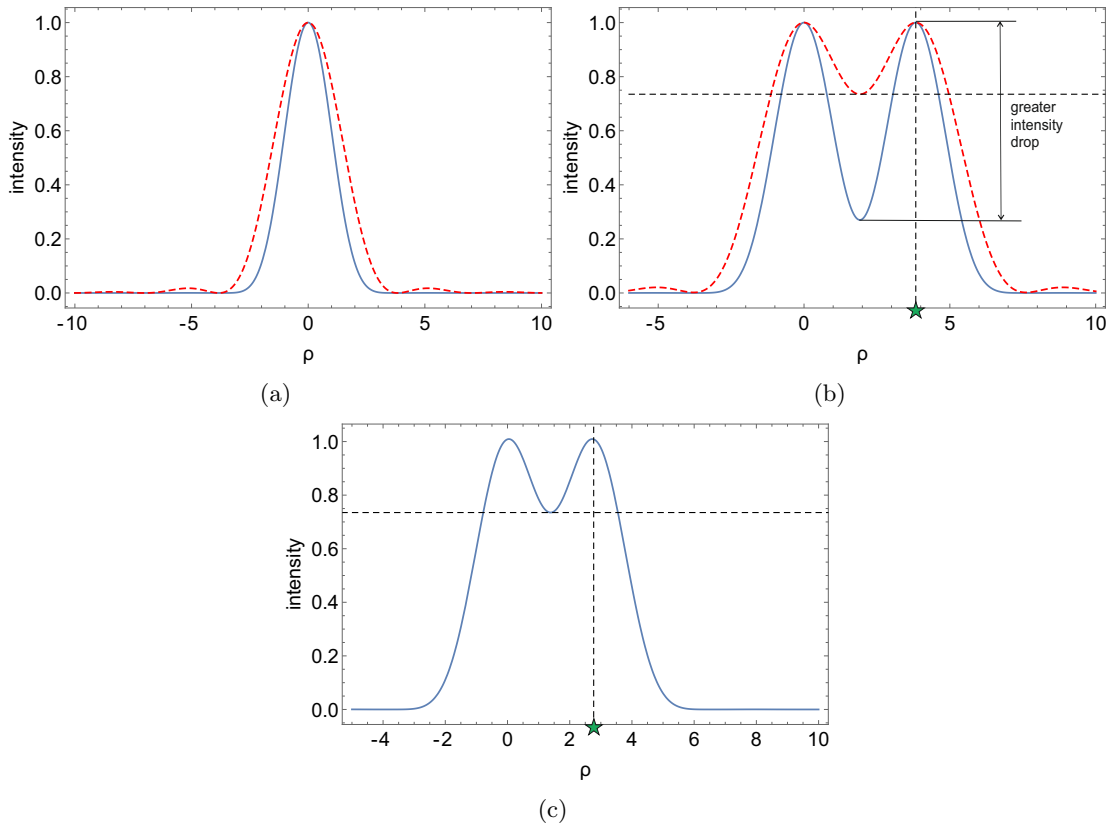


Figure 2.9: (a) Comparison of the radial PSFs of optical (red dashed line) and confocal (blue solid line) microscopy, (b) PSF intensity profile of two similar points for optical (red dashed line) and confocal (blue solid line) microscopy. The star denotes the Rayleigh distance of the optical microscopy. The confocal microscopy shows a greater intensity drop than its optical counterpart, proving its better resolution, and (c) PSF intensity profile of two similar points separated by distance corresponding to confocal microscopy Rayleigh criterion. Note the lower Rayleigh criterion marked by the star at the same intensity dip as the optical microscopy.

microscopy for two objects that are separated by the distance corresponding to the Rayleigh criterion of the optical microscopy which is 3.83 at its focal plane. The confocal microscopy shows a greater intensity drop than its optical counterpart, proving its greater contrast. In addition to that, the Rayleigh criterion for confocal microscopy at the focal plane which is 2.77 demonstrates the better resolution for laser scanning confocal microscopy, as shown in Figure 2.9(c) [56, 57].

2.5 Conclusion

In this preliminary chapter, we have shown the preparation of the colloid-polymer mixtures and introduced the system that will be used throughout the thesis. We have successfully synthesised

fluorescently-dyed colloidal PMMA and prepared xanthan solution that acts as the depleting agent in the system. From these two main constituents, we have prepared a series of mixtures to construct the phase diagram in order to study the wetting behaviour, which is the main objective of the thesis.

To vary the interfacial behaviour of the colloid-polymer mixtures with the hard walls, we have changed the surface chemistry of the wall substrates by performing surface modification with two types of polymer. The success of the surface modifications will be the topic of the next chapters.

We have also observed the thermal capillary waves of the colloid-polymer mixtures and obtained relevant interfacial parameters. All the observations were made possible by the use of laser scanning confocal microscope.

Acknowledgements

Dr. Lia Verhoeff is thanked for the tips and tricks of the colloidal and polymer syntheses and observations, as well as the discussion on the capillary waves analysis. We also thank Dr. Martin Grossel for stimulating discussion on the surface modifications.

Chapter 3

Surface Modification

ABSTRACT

In this chapter, we qualitatively observe the wetting behaviour of the colloid-polymer mixtures in the vicinity of polyacrylamide-coated and chitosan-coated walls. The interactions of the PMMA colloids and xanthan polymers with the grafted polyacrylamide and chitosan polymer brush coated on a hard wall are probed under confinement and in bulk, by means of LSCM. Importantly, we observe partial wetting behaviour. These qualitative observations form the basis of the following chapters.

3.1 Introduction

Wettability of a surface is characterised by the degree with which a droplet wets the surface, which is determined by the intermolecular interactions with the liquid droplet deposited on it, and the surrounding phase [13, 14, 15]. The wettability of a surface is usually quantified via the observed contact angle formed by the liquid droplet. From a wetting point of view, we can control the formation of the liquid droplet, by modifying the surface properties. The switching of wettability of a surface is feasible through different ways of chemical modifications.

The silanisation [58, 59] and immobilisation of polymer monolayers on the solid substrate is a promising way in changing the surface chemistry, and hence the resulting contact angle [21, 22]. The chemical modification of hydroxyl terminated substrate, which is silicon and glass, has been widely demonstrated with self-assembled monolayers [59, 60]. Zisman and his co-workers have first reported the formation of the self-assembled monolayers in the 1940s [61, 62]. However, in 1980, Sagiv [63] studied the formation process of the monolayers, their layer thickness, and the structural differences, and the research involving these monolayers systems have been growing ever since [59, 60].

Self-assembled monolayers (SAM) are ordered molecular assemblies formed spontaneously on a solid surface by adsorption of an active surfactant [60]. Among various types of SAM, organosilanes have attracted much attention due to their versatility to be covalently bonded to glass or silicon surfaces at one end, and to other organic functionalised entities at the other end, as shown in Figure 3.1. This head group of the silane agent serves as an anchor to the substrate with its alkyl chain adding stability to the monolayer via Van der Waals interactions, and the terminal end of this layer could be grafted with another polymer of interest that determines the chemical functionality of the overall system [59, 60, 64].

Manipulation of these organosilanes is an effective way in constructing dense SAM on hydroxylated silica and silicon oxide substrates [65, 66, 67]. It usually changes the surfaces from hydrophilic to hydrophobic, and hence a measurement in contact angle is a convenient preliminary analysis to test this hypothesis [21, 68, 69, 70]. However, as the organosilanes only serve as an intermediary between a glass surface and a compatible polymer, the wettability of the glass surface depends on the chemistries of the top layer polymer.

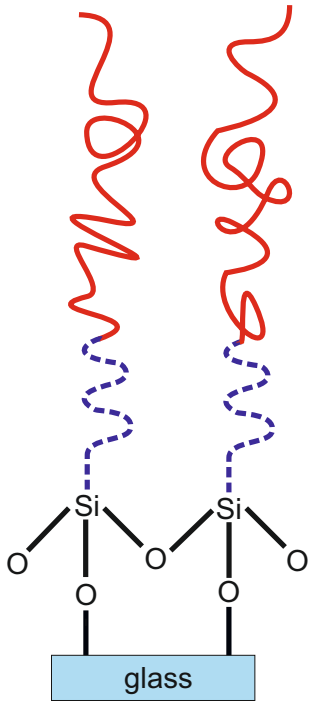


Figure 3.1: Attachment of silane and polymer to glass substrate. The dashed blue curly line represents the silane agent bonded to glass substrate, and the solid red curly line represents the polymer that is attached to the organosilane.

The attachment of this polymer onto a glass or silicon substrate can be prepared by two different techniques, namely 'grafting-to' and 'grafting-from' methods. The 'grafting-to' method involves reaction of preformed end-functionalised polymer chains with the substrate surface having complementary functional groups to form polymer brushes [71, 72]. On the other hand, the 'grafting-from' method manipulates the *in situ* polymerisation of a surface substrate functionalised with initiators. Both techniques generate covalently attached polymer brushes onto the substrates and are termed chemisorption, as opposed to polymer physisorption which only has weak interactions between any individual segment of the polymer and the substrate, with possibility of simultaneous contacts between them [71, 72, 73]. The major advantage of the 'grafting-to' method is the straightforward synthesis and possible characterisations of the preformed polymer that results in well-defined polymer chains prior to surface attachment. The polymer anchoring can be performed from a solution or a melt, and in general, a concentrated polymer solution gives a higher grafting density on the surface. The grafting density depends on the grafting time, and the termination of the grafting process as well as the removal of the residual ungrafted polymer chains can easily be controlled [72, 74]. However, this method has a major shortcoming from the grafting density point of view. The immobilisation of the polymer

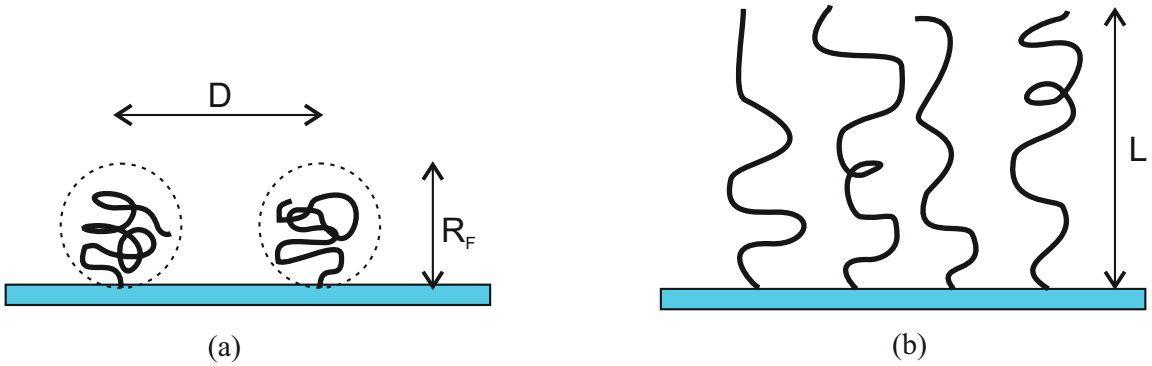


Figure 3.2: Polymer grafting in a good solvent of (a) low grafting density forms mushroom regime, and (b) high grafting density forms polymer brush.

molecules is impeded by the existence of the previously attached and residual ungrafted polymer chains on the substrate surface. This hindrance is more pronounced in a thick dense polymer brush. In contrast, the 'grafting-from' method offers higher grafting density with more uniform anchoring of polymer chains, and results in a thicker layer of polymer brushes. This is due to the nature of this method that prepares the substrate surface with initiators prior to *in situ* polymerisation with the monomers of interest [71, 72].

The properties of this polymer brush on a solid substrate is influenced by the grafting density and the solvent of the system. In real, non-ideal solvents, the size of the polymer chains can be larger or smaller than the unperturbed radius, R_g [73]. Assuming that the polymer chains are in a good solvent, the R_g of the deformed chain configuration is given by the Flory formula $R_F \approx aN^{3/5}$, where a and N are the monomer size of the polymer and the degree of polymerisation, respectively [75, 76]. At low grafting density or low surface coverage where the distance of the grafting point, D, is greater than its radius of gyration, or R_F in this case, the polymer chain is isolated and does not overlap with its neighbours, and this occurrence is known as the mushroom regime (Fig. 3.2(a)) [75, 76]. Contrary, when the distance of the grafting point is shorter, which means that the grafting density is higher, the polymer coils start to interact with its neighbouring chains. The chains overlap with one another, and the excluded volume interactions cause them to be repulsive towards each another. This leads the chains to stretch and thus increase its length, L, and the chains are said to be in the brush regime (Fig. 3.2(b)) [75, 76].

Upon grafting of polymer onto a solid substrate, the substrate is considered to have been coated with a thin layer of polymer. To physically probe the efficiency of the polymer coating,

the straightforward approach is by measuring the water contact angle of the modified surface. However, in our work, we employ the colloid-polymer mixtures to understand the wetting behaviour of the mixtures with the solid surface. The interaction between the polymer-coated walls, which can be termed as soft walls, with our colloid-polymer mixtures can be understood by first identifying possible interactions that might occur between them. In the most simple systems, these colloidal particles experience a range of attractive and repulsive inter-particle forces between each other as well as with a larger particle or a surface. The balance of these attractive and repulsive forces in a system is described by the Derjaguin, Landau, Verwey and Overbeek (DLVO) theory [77, 78]. However, in more complex systems, a number of other non-DLVO forces such as hydration, steric, hydrophobic, bridging and depletion forces may further influence the interaction of colloidal particles [73, 79].

3.1.1 DLVO potential

The DLVO potential is the sum of two inter-particle forces, the attractive Van der Waals (VdW) force and the repulsive electrical double layer force. The Van der Waals force is intrinsic in colloidal systems. On a microscopic scale, the Van der Waals force originates from the interactions between the instantaneous dipoles generated by fluctuating electron clouds. These dipoles also generate electromagnetic fields that interact, and induce the formation of instantaneous dipoles within atoms in the neighbouring particles. This polarisation of atoms leads the intermolecular interaction between the dipoles to be attractive. This adds up to an attractive force between macroscopic particles. Treating the attraction between two colloidal particles as an interaction between two plates, the Van der Waals potential energy can be written as:

$$U = -\frac{A_H}{12\pi z^2} \tag{3.1}$$

where A_H is the Hamaker constant and z is the distance between the two plates. A similar calculation can be carried out for two identical spherical particles of radius R_c separated by a distance z, provided that $z \leq R_c$, as shown below:

$$U = -\frac{A_H R_c}{12z} \tag{3.2}$$

This equation indicates that Van der Waals force can be manipulated by the changes in the particle size. For two colloidal particles of identical materials in a colloidal suspension, this long-range interaction is always attractive. The intriguing part of understanding this system is that this colloidal suspension remains stable despite of the attractive interaction between the particles. This is due to the repulsive electrical double layer force that counterbalance the attractive force in the system [73].

The system that is made up by a solution that consists charged surface particles can influence the overall ions in the surrounding medium. The counter-ions are attracted to the charged surface and the co-ions are repelled away from the surface. The attraction of the counter-ions towards the charged surface is key in maintaining the charge neutrality of the surface and a short distance towards the solution. The decaying distribution of the counter-ions away from the charged surface is called the electrical double layer. The decay length of the potential is known as the Debye length, κ^{-1}. It depends inversely on the square root of the ionic strength of the solution, ($I = \frac{1}{2}\sum_i n_i z_i^2$). The Debye length is a measure of the distance from the surface at which the ions in the solution can be unevenly distributed by the presence of the charged surface. The Debye length is then given by:

$$\kappa^{-1} = \sqrt{\frac{\epsilon_r \epsilon_0 k_B T}{2e^2 I}} \tag{3.3}$$

where ϵ_r is the dielectric constant of solvent, ϵ_0 is the permittivity of free space, $\sum_i$ is the sum of all ions, z_i^2 is the charge of ions, e is the charge of electron, and n_i is the number density of ions in bulk solution. The size of the Debye length depends solely on the properties of the solution, and not on the surface charge or its potential [73, 79].

The Debye length is also known as a shielding distance as it shows the distance over which the charged surface is shielded by the ions from the bulk. As the Debye length is proportional to the square root of reciprocal of the ionic strength, we understand that the larger the concentration of ions, the more they screen the charged surface, and hence results in a thinner Debye length. With a thinner Debye length as the ionic strength increases, the effect of the charged surface can be compromised. On the other hand, low ionic strength or low salt concentration gives a longer Debye distance. The longer the Debye distance, the stronger the electrostatic effects extending into the solution. The charged surface and associated ions generate an electrical potential at the surface region known as the zeta potential, Φ. At low potential condition, below

about 25 mV, the potential Φ in the limit of $x \to 0$ is given by:

$$\Phi = \Phi_0 e^{-kx} \tag{3.4}$$

where Φ_0 is the potential at the surface. This equation applies to symmetrical 1:1 electrolytes, such as NaCl, and Φ_0 is determined by the surface charge density, σ, as follows:

$$\Phi_0 = \frac{\sigma}{\epsilon_r \epsilon_0 \kappa} \tag{3.5}$$

In a case where we have two similarly charged particles brought into a close distance in such a way that the diffuse double layers of those particles overlap, the concentration of ions between the surfaces increases. An increase in the osmotic pressure in the overlap region results in a repulsive inter-particle force [73].

The net-balance interaction between the Van der Waals attractive force and the electrical double layer repulsive force is the reason for the charged particles in a solution to maintain being well-dispersed. The interplay between this long-range attractive force and the short-range repulsive force is what is known as the DLVO theory. The potential of force and the electrolyte content in the solution resolve for the two minimal points, known as the primary and secondary minimum, and separated by a maximum which is known as the energy barrier [80]. At low potential state, the particles are said to be in the attractive primary minimum, where they can coagulate and often irreversibly bound, and being unstable in the solution. This long-range Van der Waals force also creates a secondary minimum at a certain larger distance with a higher potential condition, and this usually more pronounced in a more concentrated electrolyte solution. At this point, the particles flocculate if the minimum is deeper than $k_B T$, and these loosely bound particles can easily be redistributed into the solution by perturbation, and this system will be stable. At intermediate separations, when the maximum point or the energy barrier is high enough, the interacting particles experience the double layer repulsion as the primary minimum is far beyond reach. Increasing the electrolyte concentration or decreasing the surface charge will reduce this double layer repulsion and destabilise the suspension of these particles [73].

3.1.2 Depletion interaction

Similar to an increase of salt concentration in a suspension of colloidal particles to tune the DLVO interactions between the particles, it is also interesting to discover the interactions between the particles when the system is made more complex by the addition of non-adsorbing polymers into the solution. This can be attributed to the nature of the polymers which are known to be entropic materials, fluctuating, and do not favour confinement. The addition of non-adsorbing polymers to a colloidal suspension can manipulate the interaction between the colloids and thus control the phase behaviour of the system. This interaction may lead to a 'gas-liquid like' phase separation which is analogous to that observed in the gas-liquid phase transition in the molecular system described by the Lennard-Jones potential [81]. This entropy-driven interaction between colloids and non-adsorbing polymers was first described by Asakura and Oosawa in 1954 [82, 83], and further detailed by Vrij 20 years later [80], and this interaction is sometimes known as Asakura-Oosawa-Vrij (AOV) model. The addition of non-adsorbing polymer with the radius of gyration, R_g, to the suspension of colloids with the radius R_c leads to a condition known as the depletion interaction. This is the region where the entropic nature of the polymers form a depletion zone around the colloids in which the centre of mass of the polymer coils are entropically excluded [84].

In general, the existence of the colloidal particles reduces the free volume of the polymers, as the added polymer chains lose configurational entropy when they get close to a hard wall or a hard particle. This entropically unfavourable reaction hinders the polymer coils to be in the depletion zone of the colloidal hard particles. If two of the zones overlap, there is a region called the overlap volume in which no polymer chains can penetrate. This causes imbalance in the osmotic pressure which encourages the polymers to push the particles together. This potential of effective attraction between colloidal particles can be described as:

$$U(r) = -\Pi V_{overlap} \tag{3.6}$$

where Π is the osmotic pressure of the polymer solution, which in turn depends on the concentration of the polymer that affect the effective attraction strength, and $V_{overlap}$ is the overlap volume that depends on the R_g of the polymer as the polymer size determines the depletion zone thickness. Hence, from this equation, we understand that these interactions are highly

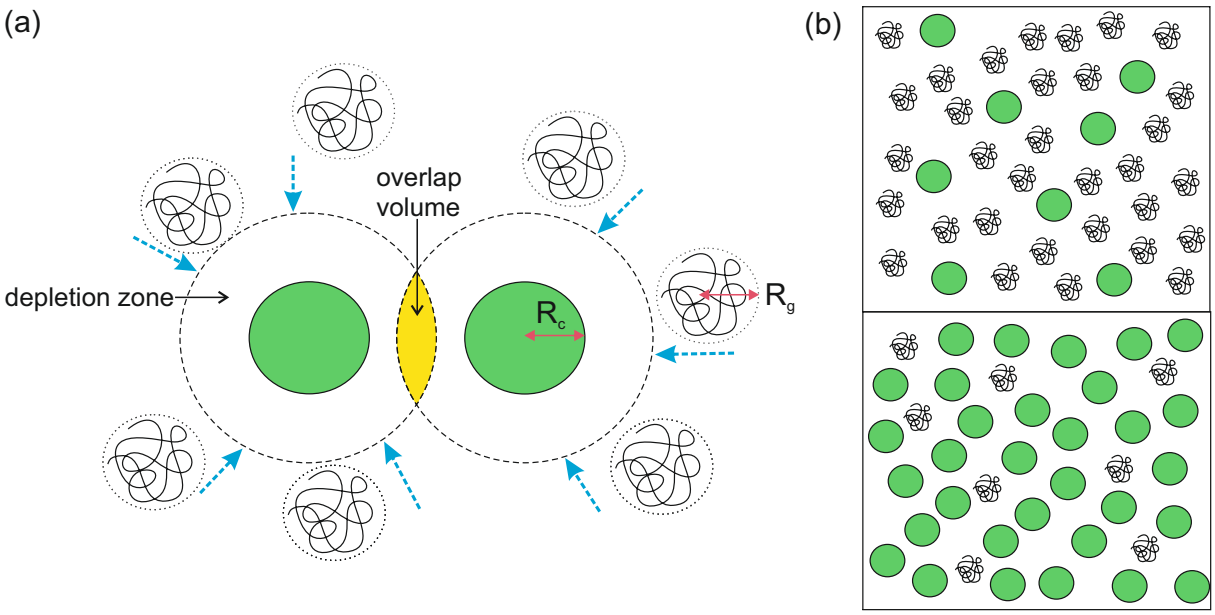


Figure 3.3: (a) Schematic diagram of the depletion interaction between two colloidal particles of the radius R_c surrounded by polymer coils of the radius of gyration R_g. (b) The phase separated colloid-polymer mixture with the colloid-rich polymer-poor phase (lower phase) in coexistence with colloid-poor polymer-rich phase (upper phase).

controllable. With the right concentration of both components, a fluid-fluid demixing transition may lead to a colloid-rich polymer-poor phase (a liquid phase) in coexistence with colloid-poor polymer-rich phase (a gas phase) (refer to Fig. 3.3). This is the kind of colloid-polymer mixtures that we use throughout this thesis with different colloid-polymer concentration combination as shown in the phase diagram in Chapter 2 of this thesis. However, the phase diagram of such phase behaviour is dependent on the colloid-polymer size ratio, $q = R_g/R_c$, as theoretically and experimentally shown by Lekkerkerker et al. [84] and Ilett et al. [85] respectively.

To understand the depletion interaction in more details, we can consider having two colloidal spheres with each sphere having a diameter of $2R_s$, with the thickness of the depletion zone around the sphere is Δ_s. The osmotic pressure of the polymer depletant solution can then be determined using $\Pi = n_b k_B T$, where n_b is the bulk number density. When two depletion zones overlap that results in an overlap volume, $V_{overlap}$, there will be an imbalance in the osmotic pressure that pushes the two colloidal spheres together, and this can be expressed in the

form of the AOV attractive depletion potential as:

$$\begin{aligned} W_{dep}(h) &= \infty && h < 0 \\ &= -\Pi V_{overlap}(h) && 0 \leq h \leq 2\Delta_s \\ &= 0 && h \geq 2\Delta_s \end{aligned} \tag{3.7}$$

The overlap volume for a sphere against a wall can be explicitly expressed using the volume of a spherical cap as follows:

$$V_{overlap} = \frac{\pi}{3} h^2 (3a - h) \tag{3.8}$$

where $a = R_s + \Delta_s$ and $h = \Delta_s + \Delta_w - z$, which can be determined from Figure 3.4. Similar to how two colloidal hard spheres interact with one another, this figure represents the depletion interaction between a colloidal hard sphere with a hard wall. For an ideal system that interacts with a hard wall, the range of the depletion interaction varies with Δ_s, and the strength of the interaction increases with the concentration of the polymer, and thus with the osmotic pressure. At low concentration of polymer, the depletion thickness, Δ_s, is approximately the radius of gyration of the polymer. With the possibility to modify the concentration of the polymer, the distance of the colloidal sphere with the hard wall, z, can also be controlled. The minimum and maximum value of the separation between the colloid surface and the wall over which the depletion is felt, are $z_{min} = 0$ and $z_{max} = \Delta_s + \Delta_w$ respectively [31, 85].

From Equations 3.7 and 3.8, we can deduce the overlap volume in its dimensionless form to project the AOV depletion interaction potential, W_{dep}, between a colloidal hard sphere with a hard wall. Figure 3.5 shows a plot of this interaction in an ideal polymer solution by assuming that $\Delta_s \approx R_g$ and $\Delta_w \approx R_g$. From the potential plot, we can see that the minimum potential value is achieved when the colloidal sphere touches the wall, with δ representing the distance of the sphere to the wall, z [31, 86, 87].

A similar approach is applicable to the interactions between a hard sphere and a polymer-coated wall, or a soft wall. The polymer coating on the wall can decrease the depletion interaction between the colloidal particles with the wall, or maybe even negate the interaction completely. Hence, instead of having the colloidal particles wetting the wall, the polymers from the colloid-polymer mixture are then showing affinity towards the polymer-coated wall. It is useful to know

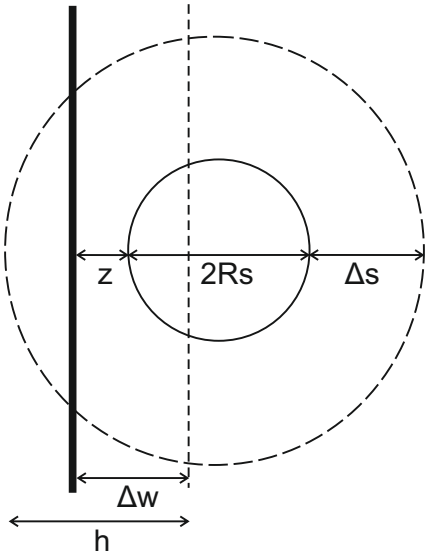


Figure 3.4: The theoretical wetting model for a hard wall. The thick black line is the wall, whilst the dashed lines represent the depletion zones of the wall and the colloidal hard sphere.

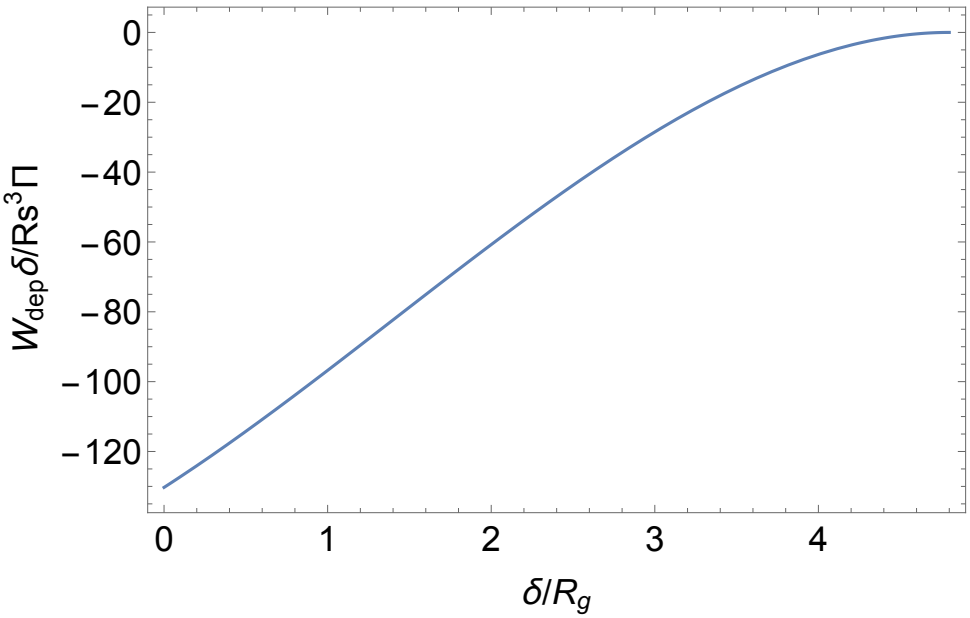


Figure 3.5: The interaction potential of a colloidal sphere against the ratio of the polymer brush thickness, z, with the radius of the colloidal sphere.

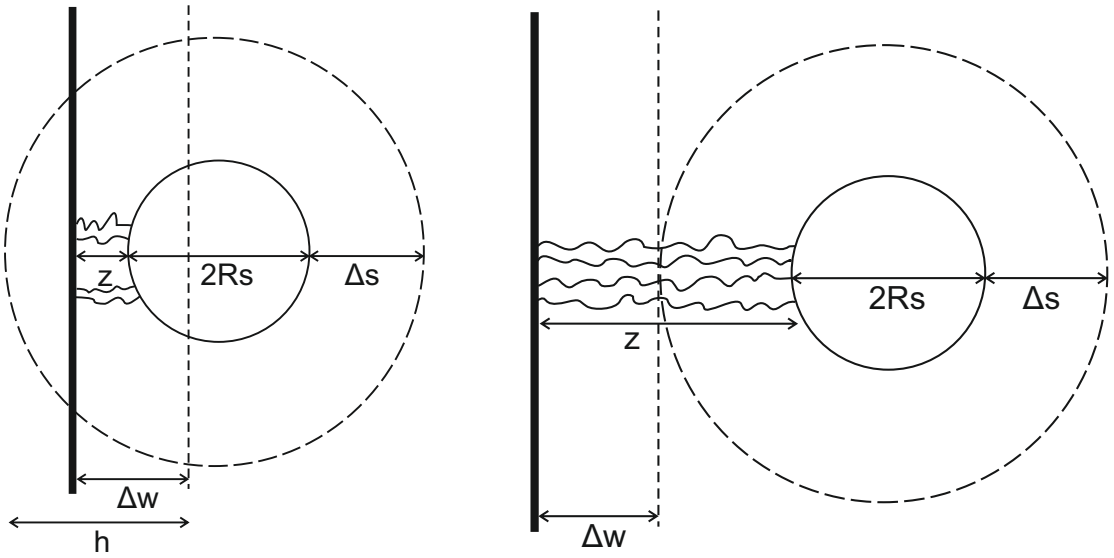


Figure 3.6: The interaction between a colloidal sphere with a soft wall with (a) a shorter polymer brush configuration attached to the wall, and (b) the furthest or maximum distance the colloidal hard sphere could be in contact with the soft wall.

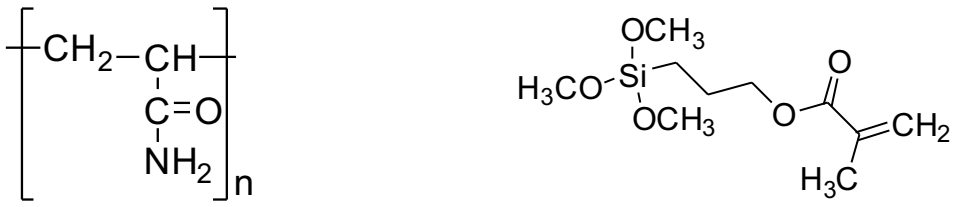
that even though the colloidal sphere is restricted from the wall by the polymer brush attached, here we assume that the polymer coils from the colloid-polymer mixture can still interpenetrate the polymer brush at the wall. In this case, the distance of the colloidal sphere to the soft wall, z, is determined by the thickness of the polymer brush as shown in Figure 3.6 (a) and (b). Having a range of the polymer brush thickness coated on the wall, we can treat the scenario as two different cases, which is when (a) $z < \Delta_w$ and (b) $z > \Delta_w$.

Having discussed the possible interactions that might happen in our colloid-polymer system, and also their interactions with either a hard wall, or a polymer-coated wall, thus in this chapter, we are observing the contact angle formation of the colloid-polymer mixtures qualitatively. The quantitative measurement of the contact angle will be discussed in the next chapter.

3.2 Polyacrylamide modification

3.2.1 Background

Polyacrylamide is a synthesised product of acrylamide monomers (Fig. 3.7(a)). It is an uncharged, water-soluble, hydrophilic polymer and well-known for its excellent permanent capillary



(a) (b)

Figure 3.7: Chemical structures of (a) polyacrylamide, and (b) the silane agent, 3-(trimethoxysilyl)propyl methacrylate (TPM).

wall coating [88, 89, 90, 91, 92, 93]. Polyacrylamide coating was first introduced by Hjertén in 1985 in coating electrophoresis glass tubes with a thin layer of linear polyacrylamide to avoid adsorption of solutes onto the inside wall of electrophoresis chambers [94]. This coating technique prepares glass or silicon substrates with covalently bonded polyacrylamide onto its surface. It involves two major steps in changing the chemistries of the surface, (i) the silanisation of the surface by a silane coupling agent to structure an anchoring base, and (ii) polymerisation of acrylamide with the silane coupling agent to form covalently bonded polymer chains on the surface [90, 91, 95, 96, 97, 98, 99].

In order to attach the polyacrylamide to the glass surface, we use 3-(trimethoxysilyl) propylmethacrylate (TPM) as the silane coupling agent (Fig. 3.7(b)). TPM has been shown to effectively create an anchoring building block that covalently bonded to the glass surface through the silanol group [100, 101, 102, 103, 104, 105]. This organosilane acts as an intermediary to link between the glass substrate and polyacrylamide that we use to form polymer brush in modifying the glass surface chemistries, as shown in Figure 3.8 [106]. Polyacrylamide coating prepared via this route exhibits permanent coating capability as it is chemisorbed onto the glass substrate.

Some physicochemical characterisations can be done to polyacrylamide-coated glass or silicon substrates to justify the success of the coatings. Apart from contact angle measurements that can be considered as a preliminary test, the formation of polyacrylamide brushes on the substrates can also be measured. Known to be a hydrophilic polymer, polyacrylamide can be anticipated to decrease the contact angle of a substrate used as a host in the grafting procedure. For instance, Fundeanu et al. (2008) measure the water contact angle of silicone rubber substrate grafted with polyacrylamide brushes via a steps-protocol of atom transfer radical polymerisation (ATRP). They first hydrophilise the silicone rubber surfaces with ultraviolet/ozone (UVO) to increase the reactivity of the surfaces by the formation of hydrophilic species such

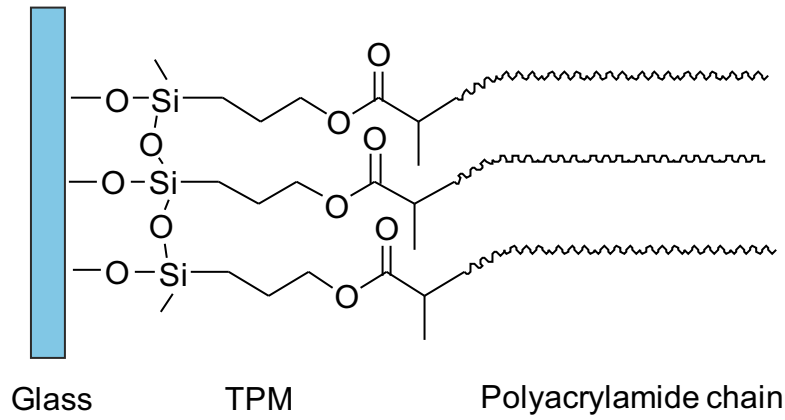


Figure 3.8: Proposed schematic diagram of the attachment of organosilane TPM to the glass substrate on one end, and to polyacrylamide on the other end.

as −OH groups and to mediate attachment of initiator. This step reduces the contact angle of the silicone rubber surfaces from 109° to 53°. Subsequently, the surfaces undergo aminosilanisation using aminopropyltriethoxysilane (APS), and the contact angle increases to 75°. Upon silanisation, the surface is treated with an initiator for polymerisation, 4-(chloromethyl)benzoyl chloride (CMBC), and the contact angle then decreases to 68°. Consequently, the grafting of polyacrylamide onto the surfaces as the final step of the coating induces a further decrease in water contact angle to 28°. The water contact angles of polyacrylamide brushes attached to silicone rubber remain stable for at least one month [107].

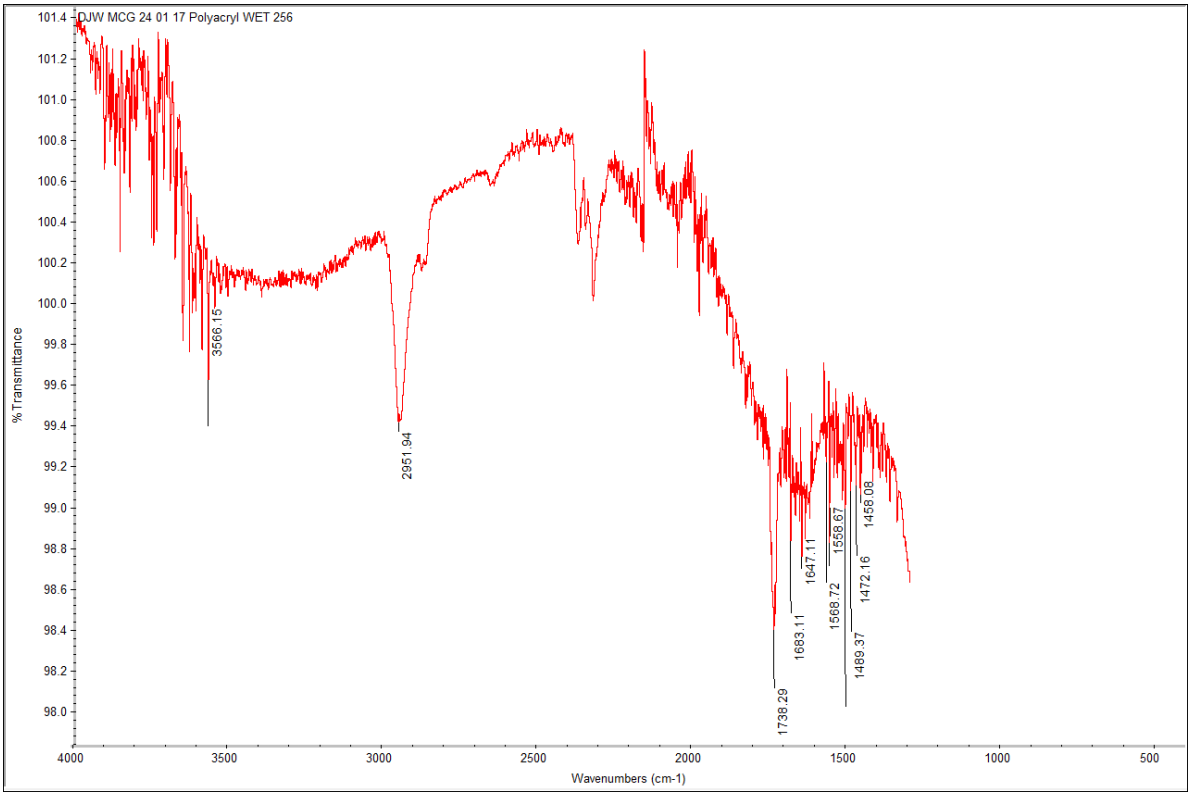
Apart from contact angle measurements, we can also observe the formation of a polymer brush onto a substrate by measuring the brush thickness. For example, Cringus-Fundeanu et al. (2007) reported on polyacrylamide brushes grown from silicon substrates by grafting from atom transfer radical polymerisation (ATRP) and the dry state of the brushes were found to be 20 nm from ellipsometry measurement [108]. Another study by Wu et al. (2002) shows that depending on the grafting density of the polymers at the substrate, the anchored chains can form either mushrooms or brushes configuration. Combination of a good solvent for polyacrylamide (i.e. water), and low grafting density, the anchored chains are independent of the grafting density and hence are in the mushroom regime, with a thickness of about 15 nm. On the other hand, in the brush regime, the chains are more crowded and thus repelling one another, and this leads the brush thickness to be higher with values ranging between 15−30 nm. The wet state thickness of the brushes can be measured using variable angle spectroscopic ellipsometry (VASE) [109].There is another report by the same research group of Wu et al. (2003) that studies the

mushroom-to-brush transition using ellipsometry as one of the tools to understand the polymer assemblies on a flat silica surface. The wet polyacrylamide thickness is measured from a sample placed in a custom-designed solution cell upon incubation of more than five hours, and evaluated using a graded effective medium approximation model based on linear combination of the optical constants of the deionised (DI) water used and polyacrylamide/DI water mixtures. It is found that the dry state thickness of the polyacrylamide brush can reach up to 4 nm, and the wet state thickness is in the range of 15−30 nm [110].

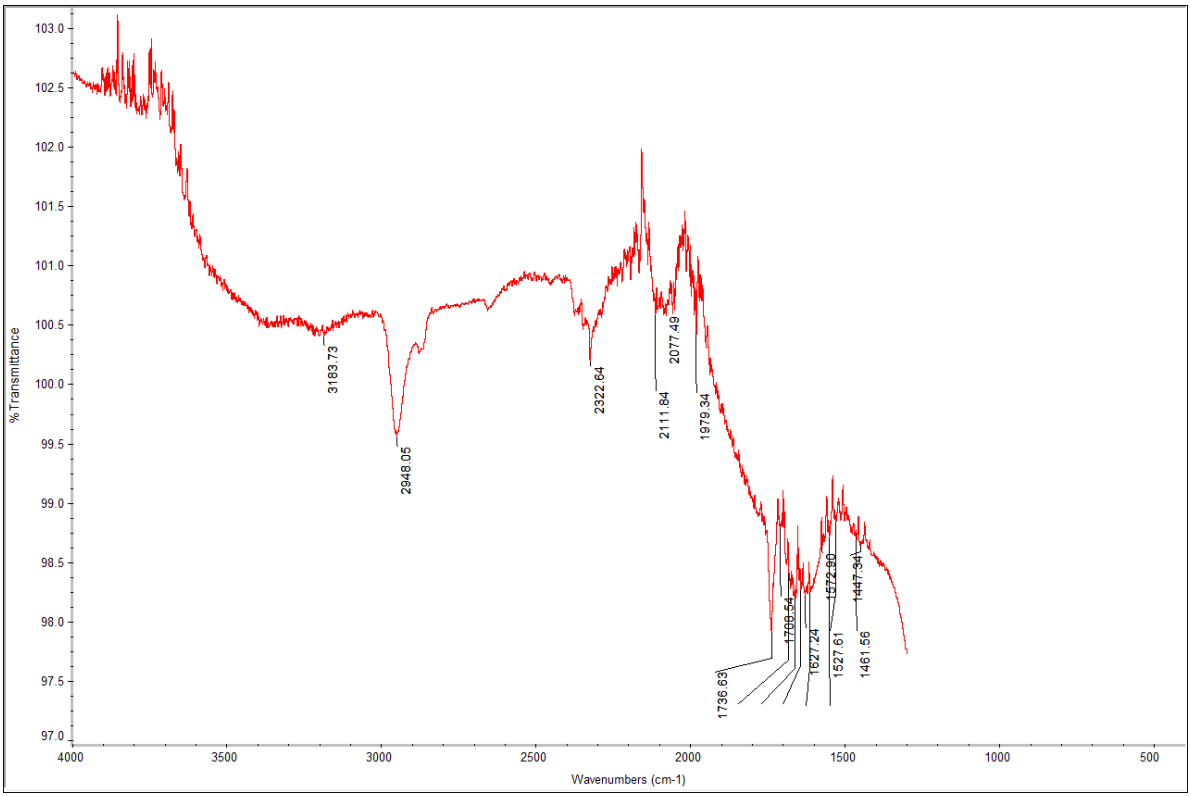
3.2.2 Characterisations

One of the chemical characterisations that we have done on our polyacrylamide-coated substrates to determine the effectiveness of the coatings towards our colloid-polymer mixtures is the Fourier transform infrared (FTIR) analysis. Figure 3.9 shows the FTIR spectra corresponding to the polyacrylamide attached to the glass walls in wet and dry states. Both states exhibit similar peak positions even though the wet state gives stronger spectra than the dry sample. This similarity implies that any drying attempt during the coated wall utilisation will not change its chemical characteristics. The carbonyl groups (C=O stretching) could clearly be seen present in both samples with bands around 1620 − 1640 and at about 1735 wavenumbers. We could also observe a strong intense peak of C−H stretching at about 2950 wavenumber. However, the N−H band that is expected to be seen in the spectra is masked by the strong broad O−H peak for both of the samples. This is due to the presence of water in the wet state sample even after nitrogen drying. Nonetheless, the signature of the amine group in polyacrylamide molecule is still visible in the dry state sample with a weak band of N−H stretching at 3183 cm^{-1}. These absorption peaks are evidence that polyacrylamide has been successfully grafted to the glass substrates similar to reports elsewhere [111, 112].

Besides that, we have also measured the surface charge or the zeta potential by analysing the electrophoretic mobility of the polymerised acrylamide to further confirm the polymer charge. Uncharged or neutral polyacrylamide can be synthesised to consist only the amide functional groups, $-CONH_2$, which do not dissociate in aqueous solutions. However, charged polyacrylamides are feasible to be synthesised based on the intended applications in which the polyelectrolyte characteristic of the polymer is of interest. This is due to the capability of the functional groups attached to the amide groups of the polymer to dissociate [93, 113]. Anionic poly-



(a)



(b)

Figure 3.9: FTIR spectra of polyacrylamide on the glass walls in (a) wet, and (b) dry states.

acrylamides are prepared with a significant degree of hydrolysis of the pendent amide groups, resulting in the formation of carboxylic acid $-$COOH [93]. On the other hand, cationic polyacrylamides are synthesised from the copolymerisation reaction of acrylamide monomers with functional groups that contain quartenised amine groups [113]. Our zeta potential measurement using Malvern Zeta Sizer gives an average value of -2.43 mV, and this can be considered as neutral. We suspect that this very small negative value charge can be attributed to the charge of the sulfate group from the ammonium persulfate initiator used in the polymerisation.

Measurement of the polymer brush thickness is also a useful way in understanding the coating behaviour. Dr. Benoit Loppinet and Antonio Giuliani (IESL-FORTH, Greece) have measured the thickness of the grafted polyacrylamide brushes using variable angle spectroscopic ellipsometry (VASE). The ellipsometry measurement gives the dry thickness of the polymer brush to be 2.5 nm averaged over a few spots on the polyacrylamide-coated silicon wafer. This dry thickness may enable us to calculate the grafting density of the polymer onto the substrate. The grafting density, σ, can be determined by $\sigma = (h\ \rho\ N_A)/M_w$ where h is the brush thickness (2.5 nm), ρ is the density of the brush composition (1.11 g/cm^3), M_w is the molecular weight (typical M_w taken for estimated calculation, 150000 g/mol), and N_A is the Avogadro's number. The grafting density for polyacrylamide onto silicon wafer is then found to be 1.1 x 10^{-2} molecules/nm^2 in our system. Taken the work by Wu et al. (2002) as a comparison, they have reported on the relation between the grafting density and the chain length [109]. They found that at low grafting density, the wet thickness is independent of the grafting density, and hence the chains are in the mushroom regime. On the other hand, the wet brush thickness increases with increasing grafting density, and thus falls into the brush regime. The intersection between the two regimes occurs at grafting density $\approx$ 0.065 chains/nm^2 [109]. We therefore expect our system to be in the mushroom regime.

Our low grafting density value may not be very surprising, considering the high M_w of the polymer and the low value of the dry brush thickness. It is also known that the 'grafting-to' method of covalent attachment not only curtails the grafting density of the polymer, but may not support dense polymer brushes formation as the attachment of polymer chains may be hindered by the existence of the previously attached and the non-grafted chains on the substrates due to the repulsive forces between the chains [72, 74, 108]. However, this low grafting density and probably random brush attachment is not critical in our case as the preliminary contact angle

test has proven the efficacy of the coating layers. To understand the brush thickness behaviour in our system, it is more useful to obtain the wet thickness of the brush at full stretch as this polymer coating is paired with our aqueous colloid-polymer mixtures. Unfortunately, Antonio did not manage to get the measurement for the wet state thickness using total internal reflection fluorescence (TIRF) microscopy. However, for estimation convenience, we may want to speculate that the wet brush thickness value is not far from the literature which is about 15 nm. This speculation is fair to be made considering that our polyacrylamide mushroom layer is placed in its good solvent which is water, and in the low grafting density, the polymer wet thickness is independent of its grafting density (neglecting the polyelectrolyte solvent of the system that is influenced by salt concentration, pH, and so forth).

3.3 Chitosan modification

3.3.1 Background

Chitosan is a derivative of the alkaline partial deacetylation of chitin, which is an abundant natural polysaccharide from the shells of crustaceans such as shrimps and crabs. The degree of deacetylation of chitosan which usually ranging between $50-90\%$ dictates the physicochemical characteristics of the chitosan, for instance in terms of its solubility, viscosity, ion-exchange capacity, and reactivity of the amino group in its molecules [114, 115, 116, 117]. Due to its versatility, this linear natural polymer with a large range of molecular weight has attracted much attention especially in biomedical applications for its biocompatibility, non-toxicity and biodegradability with biological activities in accordance to its pH-responsive behaviour [118, 119, 120, 121].

Chitosan has a repeating unit of β-(1,4)-linked glucosamine, and hence it consists a large amount of hydroxyl and amino groups in the molecules (Fig. 3.10(a)). Similar to chitin, it also exhibits insolubility in pure water, but it is generally soluble in acidic solvents with pH less than 6.5 such as acetic, hydrochloric, formic and lactic acids [121, 122, 123, 124, 125]. Solubility of chitosan in acidic solvents promotes the formation of the NH_3^+ from the predominantly amino group in its backbones, and that determines the highly charged polycationic chain of the solution [122, 126]. On the other hand, the amines of chitosan become deprotonated at high pH, and

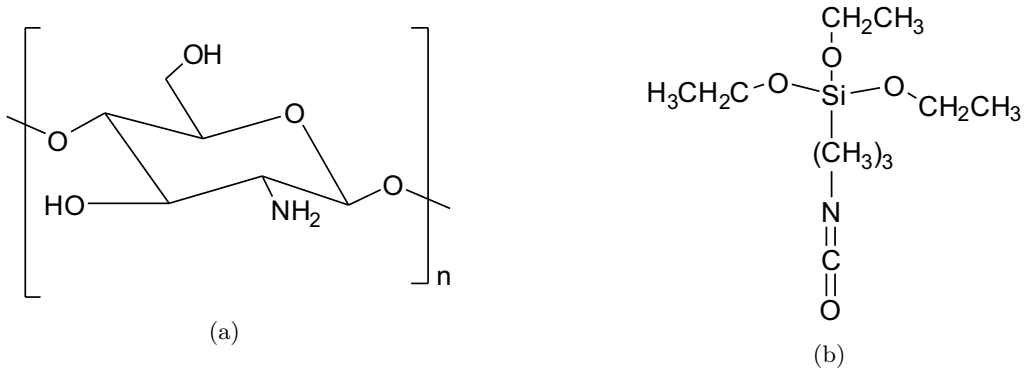


Figure 3.10: Chemical structures of (a) chitosan, and (b) the silane agent, 3-isocyanatopropyltriethoxysilane (ICPTES).

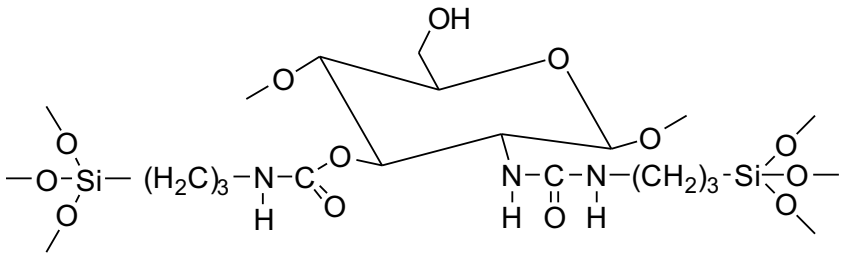
the polymer loses its charge and becomes insoluble. At this state, the electrostatic repulsions of chitosan molecules are reduced, and this allows the formation of inter-polymer networks such as fibers, films, or hydrogels. This soluble-insoluble transition occurs at a pH range of 6.0 and 6.5, which is near neutral and particularly a convenient range for biological applications [127, 128].Owing to the presence of reactive hydroxyl and amino groups in the chitosan molecules, further chemical modifications by substituents grafting can be employed to fully utilise this potential polymer in which surface properties of materials is of interest [114, 125, 127, 129].

Chemical modifications of chitosan can tune its natural properties according to our needs. This modified polymer changes the interaction between its surface and the surrounding that is in contact with it. This can be done by grafting or immobilising other macromolecules to the surface of chitosan [125, 127, 128]. One possible way of materialising this is by attaching a functionalised silane coupling agent to the reactive hydroxyl and amino groups of chitosan. The coupling of chitosan with a silane agent stipulates stronger covalent chemical bonds between the organic and inorganic moieties [130].

There are a few ways of understanding the application of chitosan in changing the surface chemistry of a substrate. Apart from chitosan immobilisation on glass or silicon substrates, preparation of chitosan films are also popular in the biomedical research and applications. One of the most convenient preliminary tests of the surface characteristics is by measuring the changes in contact angle. Having a hygroscopic nature, chitosan tends to swell in water, and changes a surface to be more hydrophilic. For instance, an experimental work done by Hoven et al. (2007) shows that surface hydrophobicity of chitosan films decreases upon the addition of charged moeities. The reactions between the amino group of chitosan with two different reagents, methyl

iodide and 5-formyl-2-furan sulfonic acid, produce positively charged and negatively charged chitosan surfaces, respectively. By monitoring the reaction of amine group of chitosan with the reagents as a function of time and reagant concentration, they come to a conclusion that the hydrophobicity of chitosan surface decreases with a longer reaction time [131]. Lü et al. (2009) has shown that immobilisation of chitosan on silicon substrate has significantly decreased the contact angle of the silicon surface by the hydrophilic molecules of chitosan [132]. Another study by Lee et al. (2012) shows that grafting of chitosan and quarternary ammonium modified chitosans on silicon wafers decreases the contact angle of the silicon surfaces, which is making it to be more hydrophilic [121].

Measurement of polymer brush layer grafted on glass or silicon substrates is also imperative in understanding the polymer response towards pH, solvent, temperature or ionic strength [133, 134]. For chitosan which is a pH-responsive polysaccharide that dissolves in low pH, the brush thickness can have a large range depending on the molecular weight of the chitosan, its solubility and can also depend on the multilayers that form on the substrate. A study by Lee et al. (2011) measures the thickness of the chitosan (M_w = 60000 g/mol) brush using quartz-crystal microbalance with dissipation (QCM-D) and in situ spectroscopic ellipsometry (SE). The dry thickness of the chitosan is found to be 6 nm (SiO_2 thickness = 1.6 nm), and when it is swelled up in different pH (3.25, 5.01, 7.17, and 8.30), the thickness can be in the range of $30-80$ nm [133]. Another study by Boddohi et al. 2008 uses Fourier transform surface plasmon resonance (FT-SPR) and variable angle spectroscopy ellipsometry (VASE) to measure the thickness of chitosan/heparin (molecular weight values measured by gel permeation chromatography are 289000 g/mol and 14400 g/mol respectively) polyelectrolyte multilayer (PEM) assembly. The glass substrates used are coated with a chromium adhesion layer (<1 nm), followed by gold (45 nm), before the gold surfaces are annealed. The annealed gold surfaces are then modified with a self-assembled monolayer (SAM) of 11-Mercaptoundecanioc acid 95% (SAM thickness = 1.7 nm) to prepare the surface with carboxylic acid groups suitable for adsorption of a polycation of chitosan. The chitosan/heparin PEM is done by alternating the pair to obtain a total of 10 layers (5 bilayers) at four different pH values (4.6, 5.0, 5.4, and 5.8) and three different buffer ionic strengths (0.1, 0.2, and 0.5 M). Taking only the first bilayer of the PEM, the chitosan contribution of the layer thickness is in between $1-3$ nm [134] .


OH
O
O
O

Besides the brush thickness measurement, the zeta potential analysis also proves another characteristic of chitosan which is positively charged in low pH environment with +650 mV in average, resulting from the highly charged polycationic chains of NH_3^+.

3.4 Different wettabilities (in confinement and at a single wall)

Having the different substrates lining up on stage, it is intriguing to observe the play between our mixtures of PMMA colloids and non-adsorbing xanthan polymers with those substrates. The wetting behaviour of the colloid-polymer mixtures in the vicinity of a hard wall has been sufficiently studied through theoretical calculations, simulations, and even proven by experiments [36, 38, 135, 136, 137, 138, 139, 140, 141, 142, 143, 144]. The understanding of the interplay between the colloids and the penetrable hard sphere polymers, and between these entities with the hard wall trigger more complex questions on the possible interactions between the colloid-polymer mixtures and substrates that exhibit non-hard wall characteristics [139, 140].

From the depletion mechanism, we understand that the interaction between the PMMA colloids and the unmodified hard wall is more favourable than the interaction between the xanthan polymers and the wall. The non-adsorbing xanthan polymers that act as a depleting agent in the system promote the entropically-driven attraction interaction between PMMA colloids and the hard wall. Hence, we anticipate the wetting of the unmodified hard wall by the fluorescently-labeled PMMA colloids, which can be observed by the formation of a fluorescent layer on the wall by a confocal microscope. This strong colloid-wall attraction has been illustrated by Aarts et al. [135] which shows the potential configurations of two colloids near a hard wall, whether it is a colloid-colloid interaction, colloid-wall interaction or colloid-colloid-wall interaction. As described in Section 3.1.2 (Fig. 3.4), the interaction depends on the overlap volume, in which the attractive interaction between the two colloids, or between the colloid and the wall, is greater if the overlap volume between them is larger [135, 138].

Theoretical work by Brader et al. [136, 137] has shown that entropic depletion interaction as set out by Asakura-Oosawa is responsible in the hard wall being completely wet by the colloidal liquid phase when the colloid-polymer mixture is left to equilibrate near the hard wall. They have performed detailed calculations using a density functional theory to explain the change in the colloid density profile near the hard wall as a function of non-interacting polymers for

the effective one-component Hamiltonian at $q = 0.1$ [137]. Prior to that, Dijkstra et al. [141] have approached the issue with computer simulations for the same colloid-polymer size ratio by integrating out the degrees of freedom of the non-adsorbing ideal polymer coils such that an effective one-component system (the colloidal hard sphere) is obtained. Keeping in mind of the theoretical treatment that the non-adsorbing polymer coils are ideal polymers, Brader et al. [136] have also presented the existence of the wetting transition in the colloid-polymer system when the mixtures are interacting near the hard wall. The entropic depletion interactions induced the colloidal liquid phase to completely wet the wall just above the critical point, before the wall is partially wet by the colloid-rich phase further from the criticality [136]. This AOV model is in a qualitative agreement with the Monte Carlo simulations by Dijkstra and Van Roij [142].

In theoretical and simulation work, the non-adsorbing polymers are always treated as ideal polymers, with the assumptions that the polymer osmotic pressure is given by the law of Van't Hoff, $\Pi = n_p k_B T$, where n_p is the number density of the polymers, and that the attraction between the segments of the polymer interchains in a theta-solvent neglects the excluded volume interactions [31, 84, 145]. However, the polymers very rarely behave close to ideal in experiments. This has been calculated by Aarts et al. [135, 145] based on previous experiments. They have first compared their findings with the polymer characteristics outlined by Lekkerkerker et al. [84] that ideal polymers are modelled as penetrable hard sphere with a radius R_g, and that the depletion layer thickness around a colloid, Δ, is equal to R_g. This is the same assumption we have made in explaining the interaction of a colloid with a hard wall in an ideal polymer solution (refer Fig. 3.4). Using the free volume theory, Aarts et al. [145] have shown that to treat the polymers more realistically as in the way the polymers behave in experiments, they have considered the excluded volume interactions between the polymer segments that swell in good solvents, as well as the effects of curvature q ($=R_g/R_c$). In another work, Aarts et al. [135] have compared the interfacial tension and wetting of colloid-polymer mixtures between ideal polymers at $q = 0.1$ with excluded volume interacting (EVI) polymer chains at $q = 1.08$. Those colloid-polymer size ratio of the ideal and EVI polymers were chosen to be compared with the existing theories [136, 146] as well as simulations [142], and with experiments [36, 147], respectively. They have shown that for ideal polymers, the position of the wetting transition is further away from the critical point than predicted by the theory [136] and simulations [142]. They have also compared their calculated wetting transition with the experimental work done by Wijting et

al. [139, 140]. By taking the same colloid-polymer size ratio $q = 0.93$ as experimentally done, they have found that the wetting transition is reasonably close to the experimental work. In addition to that, Bolhuis et al. [143, 144] have done some computer simulation work for the non-ideal polymers at a range of colloid-polymer size ratio in the colloid and the so-called protein limits as a comparison to the standard Asakura-Oosawa model theories and simulations for ideal polymers. By taking the excluded volume interactions of the interacting polymer chains in a good solvent into account, they were able to show quantitative agreement with experimental data for bulk phase behaviour.

Six years after Aarts et al. [135] presented their work, Blokhuis et al. [148] have come out with a recalculation of the work to suggest an additional contribution of the surface enhancement parameter, g, that influences the colloid-wall interaction potential, along with the surface chemical potential, h_1. The subtle interplay between the two terms accounts for the wetting and drying transitions of the system. A positive value of h_1 results in the attractive interactions between the colloid and the wall, and the expression of g is the sum of the terms g_1 and g_2. The term g_1 is the absence of the colloid-colloid interactions in the half space $z < 0$ (z is the distance of the colloid to the wall), whereas g_2 is the result of the enhancement of the colloid-colloid interactions close to the wall. They have shown that g_1 is the main contributor for g, and that both contributions to g are positive, and hence resulting in the less affinity between the colloid and the wall. Recalculating the system for both ideal and excluded volume interacting (EVI) polymers to be relatively compared to the work by Aarts et al. [135], they have taken into account the contribution from g_1 that was neglected in the previous calculations by Aarts et al. [135]. They have found that the recalculated wetting transitions for a range of different q values are all much closer to the critical points and hence fall into the second order transition based on the Nakanishi-Fisher model, whereas in contrast, the locations of the wetting transition obtained by Aarts et al. [135] are very far from the critical point. The highlight of their work is the mark of a crossover for an ideal polymer from wetting to drying transitions as q increases at $q \approx 0.935$, and they refer this occurrence as wetting reversal. This is in contrast with the recalculated version of their work that the crossover from the wetting to drying transition occurs as q decreases. However, it is difficult to compare their recalculated positions of the wetting transitions with experimental or other theoretical approaches, whereas the findings from Aarts et al. [135] are in accord with experimental work by Wijting et al. [139, 140].

Another theoretical approach by Indekeu et al. [138] has presented subtle theoretical predictions for the thickness of the wetting layer of the colloidal-rich phase adsorbed on a hard wall based on their experimental work that has been previously introduced by Hennequin et al. [149]. They have applied two theoretical predictions, (i) a simple heuristic interface potential, and (ii) the interface potential based on the linear renormalisation group (RG) theory, to predict the thickness of the wetting layer, l, adsorbed on the hard wall as a function of the height, h, above the horizontal plane of the liquid-gas interface. Using three different state points, the Van der Waals interactions are negligible by the refractive index and dielectric constant match between the colloids and the solvent, and hence the system is considered as short-range interactions. Their colloidal system reflects an attraction interaction between the colloids and the wall as $h_1 > 0$ due to a greater overlap volume between the colloid and the wall as compared to excluded volume between two colloids. With surface enhancement $g < 0$, this complementary parameter to h_1 suggests a reduced colloid-colloid interaction, and hence contributes to the colloid-wall attraction. Even though the variation of g in a system may influence the wetting transition from first order to critical (complete) wetting, but in their system, they have only experimentally observed a complete wetting ($\theta = 0^\circ$) with the vertical wetting layer adsorbed at the wall. With that basis, they have shown that the two theoretical approaches result in an almost identical predictions for the wetting layer thickness, l, versus height, h, for all the state points. However, experimental data for the state point closest to the critical point displays two distinct regimes instead of one as predicted by the theory, which is likely to happen due to the layer thickness not reaching the equilibrium yet despite resting times of up to several days [138].

Interestingly, this theoretical and simulation work has been described hand-in-hand with experimental observations to manifest the actual behaviour of the polymers in real life. Some initial experimental work has been successfully presented by Aarts et al. [33, 36, 38] and Wijting et al. [139, 140]. They have shown the attraction of the colloidal liquid phase towards the hard wall substrate using similar colloid-polymer systems of either poly(methylmethacrylate) (PMMA) colloids and poly(styrene) (PS) polymers in the solvent decalin, or spherical silica colloids and poly(dimethyl siloxane) (PDMS) polymers dispersed in cyclohexane as a solvent. If the challenge of the theoretical manifestation is about treating the non-adsorbing polymers more realistically, the experimental hurdle is more about obtaining accurate measurements of the contact angle from clear reliable images [135], which we have conquered and will be presented qualitatively and quantitatively in this chapter and the subsequence.

Wijting et al. [140] have also taken a step further by modifying the hard glass fibers they were using with PDMS, in an attempt to manipulate the particle-substrate interactions. They have compared the colloidal liquid phase interaction with the PDMS-coated wall, termed as a soft wall, along with its hard wall counterpart. They have shown qualitatively that the static contact angle of the colloidal liquid phase at the hard wall is less than 90°, implying that the colloidal liquid phase has a stronger attraction towards the hard wall due to the larger overlap volume between the colloid and the wall than the colloid-colloid interaction. On the other hand, the colloidal liquid phase exhibits a contact angle of more than 90° with the soft wall, showing a reduced interaction between them due to repulsive steric contribution. This implies that the colloidal gas phase prefers the PDMS-coated wall. Besides that, they have also shown the wetting transitions that occur at state points farther away and closer to the binodal line, with a few tie lines separating the partial and complete wetting boundaries. As for the hard wall observations, the colloidal liquid phase displays a partial wetting regime further away from the binodal line and complete wetting is achieved at state points closer to the binodal line. However, they have also shown that by grafting polymer chains to the substrate, the wetting transition occurs from partial wetting by the colloidal liquid phase to complete drying of the PDMS-coated wall by the polymer gas phase. These observations were made at state points far from the critical point which was determined by extrapolating the middle points of the tie lines to the binodal, to the ones closer to criticality. However, they did not characterise the properties of the PDMS-coated glass in detail, and due to the fuzzy liquid-gas interface of the images, the deductions of the coating success was only based on the contact angle of water that was remarkably larger than on unmodified glass. Apart from the fuzzy interface of the images, they have also mentioned about the difficulties in measuring the contact angle of the colloid-polymer system towards the substrates due to the small capillary length, l_c, and the low optical contrast between the colloidal liquid phase and the colloidal gas phase. Therefore, they determined the static contact angles by interpolation from the advancing and receding dynamic contact angles that was done by drawing tangents to the liquid-gas interface in the three-phase points [140]. The contact angle measured by interpolation in the report has been criticised by Aarts et al. [135]. The challenge in measuring the contact angle from images of the phase-separating colloid-polymer system will be tackled in the next chapter.

Putting that extended idea into realisation in our system, we have observed the interactions of the PMMA-xanthan colloid-polymer (colloidal liquid phase and colloidal gas phase) samples

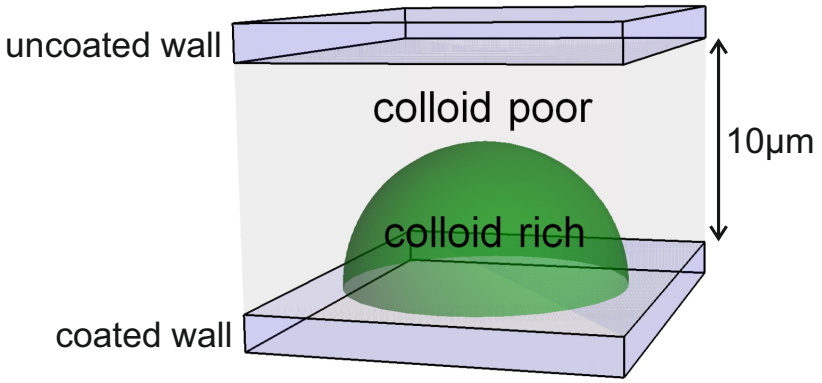


Figure 3.12: Formation of colloidal liquid droplets in the polymer phase dominant under asymmetric walls confinement, or single wall confinement. The bottom wall is the polymer-coated wall and the top wall is the uncoated clean glass. Both walls are separated at about 10 µm in distance, or the z axis obtained under the confocal microscope.

with the modified walls in both confinement and in bulk geometries. We have confined our colloid-polymer mixtures between two parallel glass walls of about 10 µm apart, with one wall coated with either polyacrylamide or chitosan as the bottom wall, and the top wall a clean glass. A colloid-polymer mixture sample that has a higher xanthan polymer concentration forms a morphological characteristic with droplets of the colloidal liquid phase (Fig. 3.12). As shown in Figure 3.13(a), we can observe that the droplets partially wet the polyacrylamide-coated wall with a wetting contact angle of less than 90°. Similarly, we can also see that the chitosan-coated glass wall exhibits partial wetting of the surface by the colloidal liquid phase droplets (Fig. 3.13(b)). Both images prove that by modifying the surface of the glass wall with polymers, we change the affinity of our colloid-polymer mixture towards the confining walls from wetting to partial wetting. These results can be compared to a clean glass wall that serves as a control as shown in Figure 3.13(c). This figure clearly shows the wetting of the hard wall by the PMMA colloids with $\theta = 0°$, similar to experimental results that have also been shown by Dr. E. Jamie in her thesis [43].

To further assess the efficacy of the surface modification, we confine a colloid-polymer mixture between two parallel polyacrylamide-coated walls. Contrary to the first sample mixture we use, this sample mixture which is PMMA-colloid dominant forms spherical droplets of the colloidal gas phase. It is conspicuous that the colloidal gas phase is attracted to both symmetrical coated walls and forms a contact angle of about 90° (Fig. 3.14(a)) with a sharp colloid-polymer interface. Alongside that, we have observed the colloidal gas phase behaviour towards chitosan-coated wall by designing a sample cuvette in such a way that the sample is not confined. With

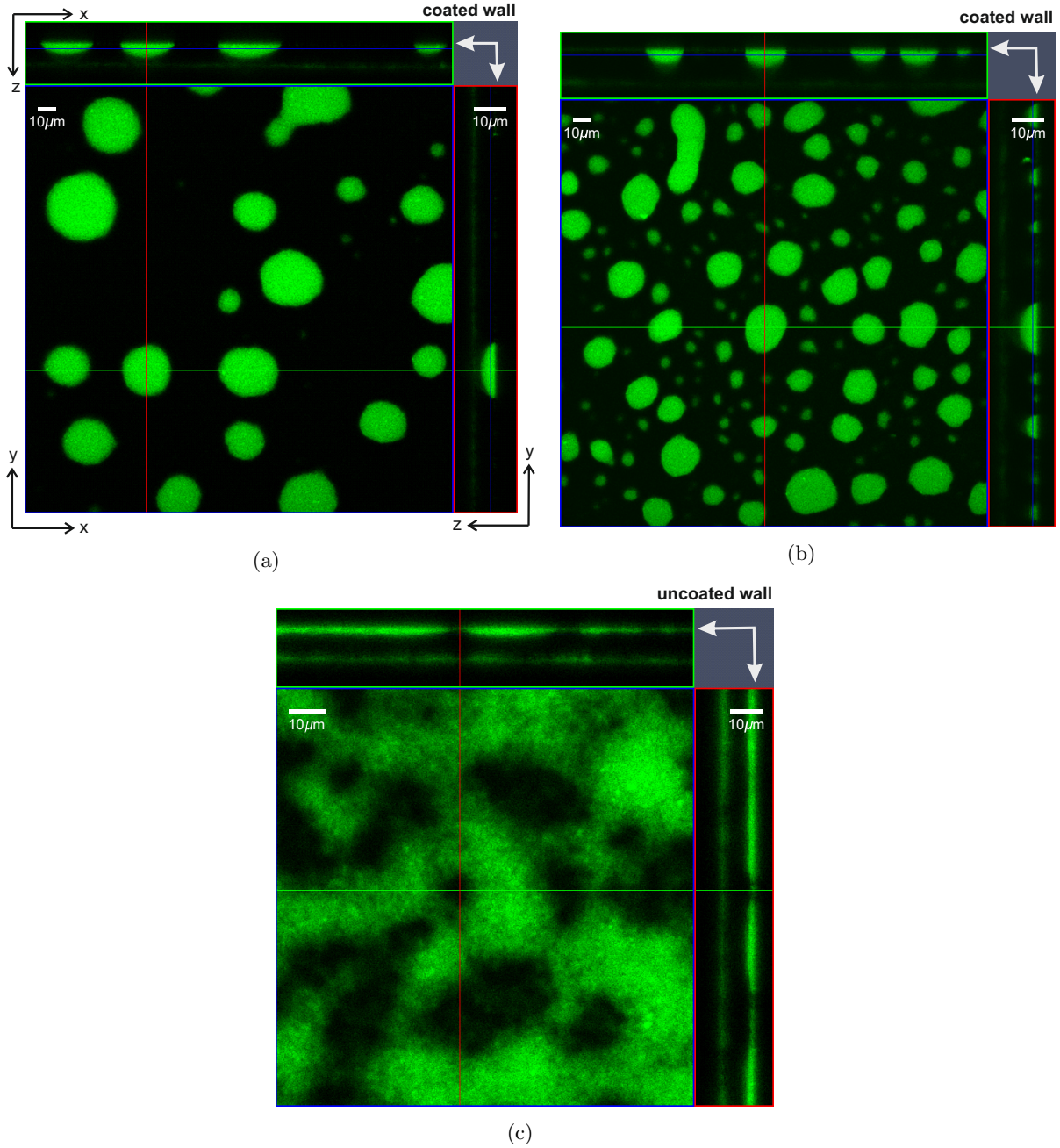
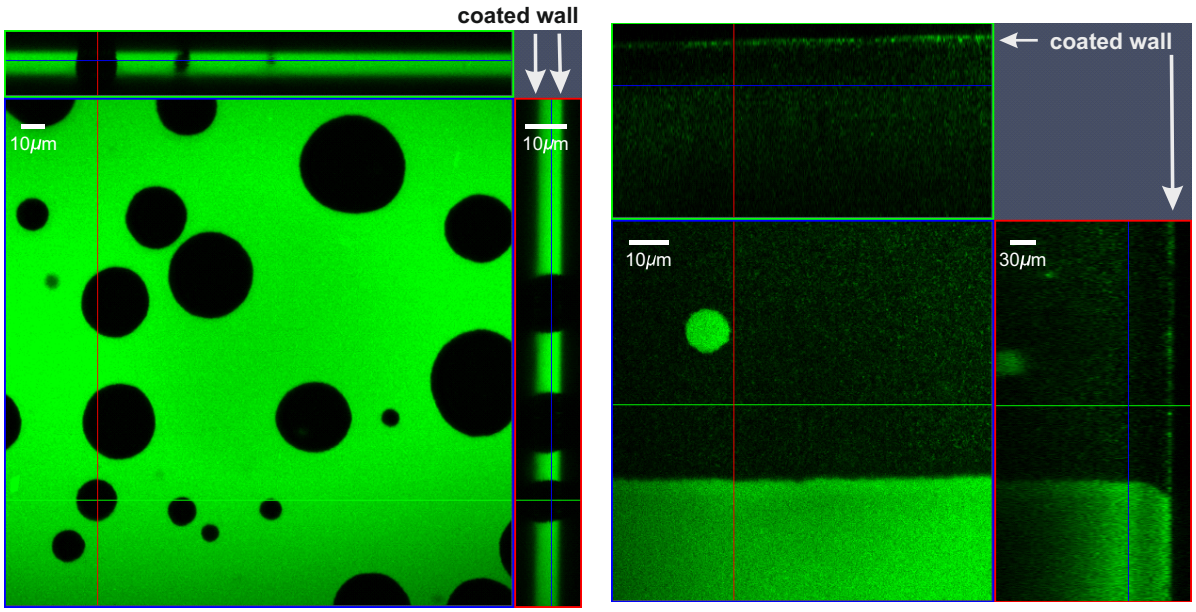


Figure 3.13: Confocal microscope images for single wall confinement of PMMA-xanthan colloid-polymer mixtures at glass walls coated with (a) polyacrylamide, and (b) chitosan, with (c) clean glass as a control. Fluorescently-dyed PMMA colloid is identified with the colour green. The images were taken with the z-stack mode of the confocal microscope. The xy axes show the layout of the xy plane of the sample slide, while the two adjacent fragments (labelled as the xz and yz axes) show the z-stack with respect to the xy plane, indicating the thickness of the sample slide. The coated wall that serves as the base wall is pointed out by the arrows for (a) and (b), along with the uncoated wall for (c). The axes of image (a) are also applicable to images (b) and (c).



(a) (b)

Figure 3.14: Confocal microscope images showing different ways of testing the polymer-modified glass walls by observing the behaviour of the PMMA-xanthan polymer mixtures towards (a) symmetric polyacrylamide-coated glass walls used to confine the sample, and (b) chitosan-coated glass wall with the influence of gravity in a non-confined sample cuvette in such a way that the sample is in bulk.

the influence of gravity, the sample phase-separates into colloidal liquid phase and colloidal gas phase, and the mixture is left to reach equilibrium before observation is made. Here, we observed a capillary depression formed by the colloidal gas phase in the vicinity of the chitosan-coated wall surface which reveals the reduction of the colloid-wall interaction as shown in Figure 3.14(b). This observation is in opposition to the capillary rise phenomenon that we can anticipate with a normal clean glass. The attraction of the PMMA colloidal liquid phase towards a hard wall that results in the capillary rise phenomena has also been experimentally shown by Aarts et al. [33] and Hennequin et al. [149], apart from other similar system of colloid-polymer silica-poly(dimethylsiloxane) (PDMS) mixtures in cyclohexane by Aarts et al. [36] and Wijting et al. [139, 140].

By materialising the aforementioned concept, we understand that when we modify the glass wall with polyacrylamide and chitosan polymers, we change the nature of the colloid-substrate interactions when the glass wall is coated with one end of the polymer brush chemically bound to the wall surface. This polymer brush acts in such a way that it effectively repels the colloidal particles from the wall by forming an excluded volume close to the wall, and this reaction results

in the reduction of the colloid-wall interaction. This occurrence has been described in Section 3.1.2, and the aiding figure (Fig. 3.6) shows that the distance of the colloidal sphere to the polymer-coated wall is determined by the thickness of the polymer brush.

It is also interesting to look at the whole system from a charge point of view. The attraction between the xanthan polymers and the polymer brush attached onto the wall can be attributed to the attraction of opposite charges. As chitosan is highly cationic and xanthan polymer is negatively charged, we can anticipate a strong affinity between them. However, the influence of the charge is not always the case as in the interaction between the neutral polyacrylamide and the xanthan polymer. In this case, however, the xanthan polymers in the system can to some extent penetrate into the polymer brush layer that coat the wall. Depending on the homogeneity of the coating and the state point of the colloid-polymer mixtures in the phase diagram, we have been able to observe partial wetting and drying states in our system. These observations form the basis of the subsequent chapters, but here we will qualitatively illustrate the wetting behaviour through confocal images.

3.5 Conclusion

We have given an overview of the different interactions of play in a colloidal model. We look at the interactions in our PMMA-xanthan colloid-polymer system from the depletion interaction point of view. By taking a step further from it, we have also shown the possibility of tuning the colloidal phase behaviour towards different substrates. The colloidal liquid phase that is ideally known to wet a hard wall can exhibit opposite behaviour towards a polymer-coated wall.

In this chapter, we have proven that polyacrylamide and chitosan polymers are efficacious in modifying the glass surfaces to alter its wettability. With the existence of the polymer layers on the hard wall surfaces, we were able to transform the surface to become soft walls, and thus tune the wettability from wetting to partial wetting, and even drying.

Those observations were made possible with our PMMA-xanthan colloid-polymer mixtures which exhibit a discernible morphology with the confocal microscope. Upon phase-separation, the PMMA colloid liquid phase has shown the tendency to wet the hard wall surface, whereas in contrast, the xanthan polymer gas phase has demonstrated an affinity towards the polymer-

modified wall surfaces.

Acknowledgements

We would like to thank Dr. Benoit Loppinet and Antonio Giuliani for the measurement of the polymer brush thickness. Dr. Martin Grossel is also thanked for the infrared measurement.

Chapter 4

Contact Angle Measurement of Colloid-Polymer Mixtures in Confinement

ABSTRACT

This chapter focuses on the quantitative contact angle measurement of our colloid-polymer mixture confined between a chemically modified wall using (i) polyacrylamide and (ii) chitosan polymers, and a clean glass wall. The confinement of the mixtures with asymmetric glass walls exhibits the formation of liquid droplets on the partially wetting modified wall which proves that the polymer grafting of the surfaces has a profound effect on the wetting behaviour. This geometry allows for the determination of the contact angle. The shape of the droplet is theoretically described by the interplay between gravity and interfacial curvature, with the contact angle entering as a boundary condition. Upon analysing the confocal microscopy images of the system using image analysis software built in-house, we are able to fit the interfacial drop profiles to the theoretical model. This allows quantitative measurement of the contact angle for mesoscopic droplets, where the droplet size is only an order of magnitude larger than the thermal roughness of the interface.

4.1 Introduction

Wetting phenomena in colloid-polymer mixtures have received considerable theoretical attention, see the introduction of Chapter 5. The precise measurement of the contact angle, however, has not yet been reported in literature, except for a very recent study published in Soft Matter [150]. Here, the authors invoke the line tension and describe part of the droplet shape with an interface displacement model [150, 151, 152]. We show that in our case, we do not need to add the line tension to our theory, but rather we are able to describe the drop shape using surface tension and gravity terms.

The measurement of the contact angle of a liquid drop placed on it is one convenient way to understand the wetting properties of a surface. This is widely known as the sessile drop technique. Many variations including static goniometric and dynamic tilted plate methods fall into this category. They essentially involve the macroscopic contact angle measurement from digital image analysis with the drop profiles fitted to a spherical cap or ellipse, or full numerical solutions to the Young-Laplace equation [153, 154, 155, 156, 157, 158, 159, 160]. Of particular note is the axisymmetric drop shape analysis (ADSA) which was first introduced by Rotenberg et al. [161], and measures the contact angle by taking the entire shape of the drop into account and performing a comparison with a theoretical curve representing a solution of the Laplace equation [162, 163]. This is similar to the approach we will follow.

We adopt a systematic method using colloid-polymer mixtures to generate images of microscopic droplets and subsequently measure the contact angle. These mixtures, which phase-separate into colloid-rich, polymer-poor phase (colloidal liquid) in coexistence with colloid-poor, polymer-rich phase (colloidal gas) upon mixing, are studied in the vicinity of different substrates modified with two types of polymer, polyacrylamide and chitosan (refer to Chapters 2 and 3). This colloid-polymer system has advantages as a good model system in studying the variations in contact angle as the interaction range of the polymers can be tuned by changing the molecular weight and concentration of the polymers. Due to the ultralow interfacial tension, the interface fluctuations can be followed in real-time and real-space [36, 164]. This makes it possible to study contact angle phenomena at length scales down to the interfacial width .

We use confocal microscopy and observe the morphology of the droplets on the polymer-

modified solid substrates (Section 4.3). Here, we obtain 3D images and image slices from the z-stack and reproduce these images using Mathematica for further analysis. We develop a method based on Young-Laplace equation and derived Euler-Lagrange equation (Section 4.2) to quantitatively measure the contact angles as presented in Section 4.4 from the drop profiles obtained from the raw 3D images. We end with a conclusion (Section 4.5).

4.2 Theoretical background

The theory was contributed by Professor Carlos Rascón from Department of Mathematics, University Carlos III de Madrid, Spain.

To analyse a drop on a substrate, we assume that the liquid drop is rotationally symmetric around its vertical axis, z. For this configuration, we solve for $z(r)$.

The energy of the drop's configuration is given by three contributions, (i) the liquid-gas surface tension, (ii) the gravitational contribution, and (iii) the interaction with the substrate. The contribution from the liquid-gas surface tension corresponds to the liquid-gas surface tension, γ, multiplied by the area of the liquid-gas interface:

$$\gamma \int (2\pi r)\sqrt{\mathrm{d}r^2 + \mathrm{d}z^2} = 2\pi\gamma \int_0^R r\sqrt{1 + z'^2}\,\mathrm{d}r. \tag{4.1}$$

The gravitational contribution can be obtained as the sum of cylindrical layers of radius, r, and is given as:

$$g\Delta\rho \int (2\pi r)\frac{1}{2}z^2\,\mathrm{d}r = 2\pi g\Delta\rho \int_0^R \frac{1}{2}rz^2\,\mathrm{d}r. \tag{4.2}$$

The interaction of the drop with the substrate is just the contact area multiplied by $-\gamma\cos\theta$ that gives $-\gamma\cos\theta\,\pi\,R^2$.

Hence, the total energy expression can be written as:

$$\frac{H[z]}{2\pi\gamma} = \int_0^R \left(r\sqrt{1 + z'^2} + \frac{1}{2{L_c}^2}rz^2\right)\mathrm{d}r - \frac{1}{2}\cos\theta\,R^2, \tag{4.3}$$

where $L_c = \sqrt{\gamma/\Delta\rho g}$ is the capillary length.

Apart from the energy contributions, we have to consider the constraint from the volume of the drop that is fixed, and can be given by:

$$\frac{V[z]}{2\pi} = \int_0^R rz \, \mathrm{d}r. \tag{4.4}$$

Having both the energy contributions and the volume of the drop, we can derive two equations that are necessary in fitting our experimental results to the theory. Minimisation of the free energy equation, Equation 4.3, with the constraint of fixed liquid volume produces (i) the boundary conditions, and (ii) the Euler-Lagrange equation. The boundary conditions are the standard conditions that force the contact angle to be the contact angle at each wall, and the equation is given as:

$$z'(R) = -\tan\theta. \tag{4.5}$$

The Euler-Lagrange equation can be expressed as:

$$\frac{1}{L_c^2} rz + \lambda r = \frac{\mathrm{d}}{\mathrm{d}r}\left(\frac{rz'}{\sqrt{1+z'^2}}\right), \tag{4.6}$$

where λ is a Lagrange multiplier that, in principle, can be tuned so that Equation 4.4 is satisfied. The Euler-Lagrange equation can be rewritten to be:

$$\frac{1}{L_c^2} rz + \lambda r = \frac{rz'' - z'\left(1+z'^2\right)}{\left(1+z'^2\right)^{\frac{3}{2}}}. \tag{4.7}$$

It is important to note that Equation 4.7 is the equation of a liquid drop on the bottom wall, or a gas bubble (immersed in liquid) on the top wall. If the liquid drop is on the top wall (hanging drop), or equivalently, we are describing a bubble on the bottom wall, then $\Delta\rho$ changes sign, and the equation will be:

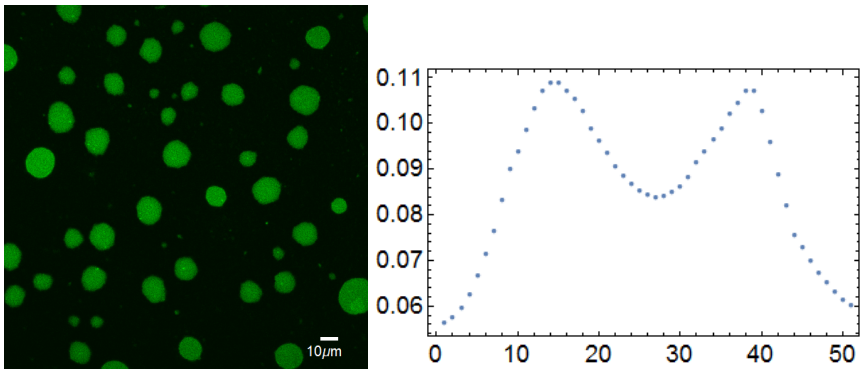
$$-\frac{1}{L_c^2} rz + \lambda r = \frac{rz'' - z'\left(1+z'^2\right)}{\left(1+z'^2\right)^{\frac{3}{2}}}. \tag{4.8}$$

The solution sets of Equations 4.7 and 4.8 are very different. However, in either case, the solution is a spherical drop in the limit of small volume or small gravity.

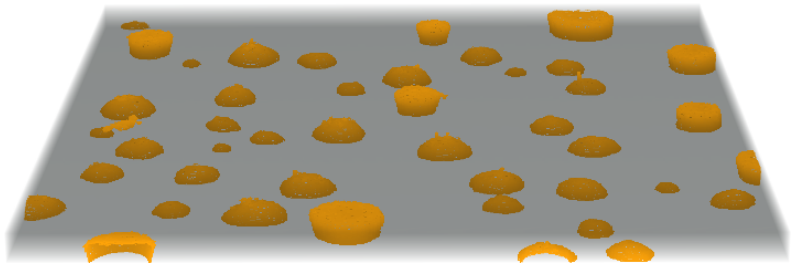
4.3 Experimental section

We fabricate a system consisting of fluorescently labelled poly(methylmethacrylate) colloidal particles of radius $R_c = 110$ nm and non-adsorbing xanthan polymers of radius of gyration $R_g = 264$ nm as a model system to understand wetting behaviour from mesoscopic scale contact angle measurements in a confined environment. This colloid-polymer mixture phase-separates into colloid-rich, polymer-poor phase (liquid phase) in coexistence with a colloid-poor, polymer-rich phase (gas phase) due to the depletion interaction between the colloids mediated by the polymers. We study the behaviour of this colloidal mixture in the vicinity of different substrates which serve as the confining walls. The glass walls used are chemically modified with (i) polyacrylamide and (ii) chitosan polymers, and in addition, a clean glass wall is used as a standard. This work utilises a laser scanning confocal microscope (LSCM) to study the system optically in three dimensions. Our initial focus on the interface between the colloidal liquid phase and the colloidal gas phase after a complete phase separation enables us to determine the capillary length of the system. The methods and preparations of the colloid-polymer mixture and the polymer-coated glass walls are described in detail in Chapter 2.

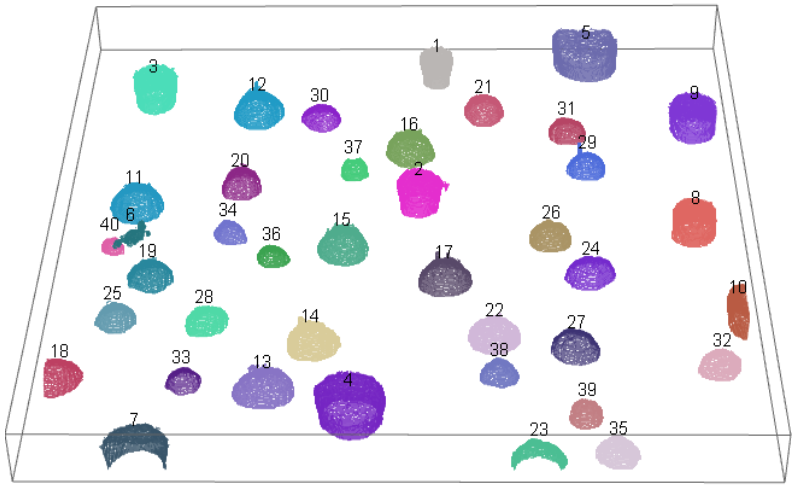
For image analysis, we utilise Mathematica to analyse and fit our experimental data to the theoretical prediction of the droplet shape in order to measure the contact angle of each droplet. Under this section, we show the preliminary image analysis before the fitting of the droplet to the outlined equations is done. For an example, we use an image from a colloid-polymer mixture at state point 5b in the vicinity of a PAA-coated wall taken at 180 min. We started by choosing a raw image acquired from the confocal microscope (Fig. 4.1(a)). This image is obtained by scanning the sample in 3D setting (taking the z-stack step). From that image, we plot the intensity profile with two peaks showing the intensity of both the bottom and top walls of our confinement system (Fig. 4.1(b)). Next, we reconstructed the image by binarising the raw data, and neglecting very small size droplets (Fig. 4.1(c)). For the convenience of tracking each droplet, we then labeled each droplet with number (Fig. 4.1(d)). Upon binarising and identifying the droplets, we started to work on detecting the surface of the droplet to be fitted later to the theoretical droplet shape as shown in Figure 4.1(e). Further analysis of the droplet surface until the accomplishment to obtain the contact angle will be discussed in the next section.



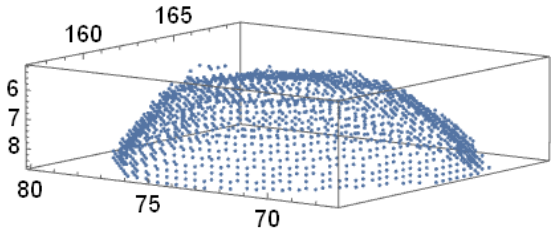
(a) (b)



(c)



(d)



(e)

Figure 4.1: Binarising and identifying the droplets of PAA-coated wall: (a) a raw confocal image, (b) intensity profile of the bottom and top walls of the confinement (arbitrary unit of axes), (c) binarising the 3D image, (d) identifying the droplets, and (e) detecting the droplet surface (arbitrary unit of axes).

Table 4.1: The concentration (denoted as 'c') and volume fraction (denoted as 'ϕ') of PMMA colloid and xanthan polymer at state points 5a, 5b and 5c.

State point	**PMMA**	**Xanthan**	**PMMA**	**Xanthan**
5a	$c_c = 0.059$ g/ml	$c_p = 1.64 \times 10^{-3}$ g/ml	$\phi_c = 0.05$	$\phi_p = 18.54$
5b	$c_c = 0.047$ g/ml	$c_p = 1.30 \times 10^{-3}$ g/ml	$\phi_c = 0.04$	$\phi_p = 14.62$
5c	$c_c = 0.039$ g/ml	$c_p = 1.08 \times 10^{-3}$ g/ml	$\phi_c = 0.03$	$\phi_p = 12.05$

4.4 Results and discussion

Referring to the experimental phase diagram in Figure 4.2, we have prepared three samples of polymethylmethacrylate (PMMA)-xanthan colloid-polymer mixture as shown in Table 4.1. In these samples at state point 5a, 5b and 5c (shown with arrows in the phase diagram), the non-adsorbing polymer component is dominating by 80%, making the fluorescently-labeled bright-coloured colloidal liquid phase a minority in the system and hence forming the dispersed phase. The higher percentage of the xanthan polymer concentration which acts as a depleting agent in this system increases the depletion interaction of the colloids, and thus leads to a sharp colloid-polymer interface as can be seen in Figure 4.3. From the figure, we can observe the behaviour of the colloid-polymer mixture at state point 5b after 180 min in the vicinity of polyacrylamide-coated (PAA-coated) (Fig. 4.3(a)) and chitosan-coated (Fig. 4.3(b)) glass walls as well as a clean glass slide (Fig. 4.3(c)), when put under confinement of parallel walls of approximately 10 µm apart. The walls of interest are positioned as the lower plane and another clean glass is put parallel to it as the top wall of the confinement. The demixing of the mixture takes place immediately after the confinement slide is prepared, but due to the higher polymer content which slows down the process, we take measurements after 60 min and up to 180 min, at different positions on the slide, to give ample time for the sample to reach equilibrium. Note that we also observe the droplets formation after 180 min, and left a sample overnight to see if there is a change in the wetting behaviour with respect to time.

Figures 4.3(a) and 4.3(b) illustrate the xz plane images of the colloid-polymer mixture behaviour in the vicinity of the PAA-coated and chitosan-coated glass walls, respectively. The mixture, which was sandwiched between asymmetric walls and placed perpendicular to gravity,

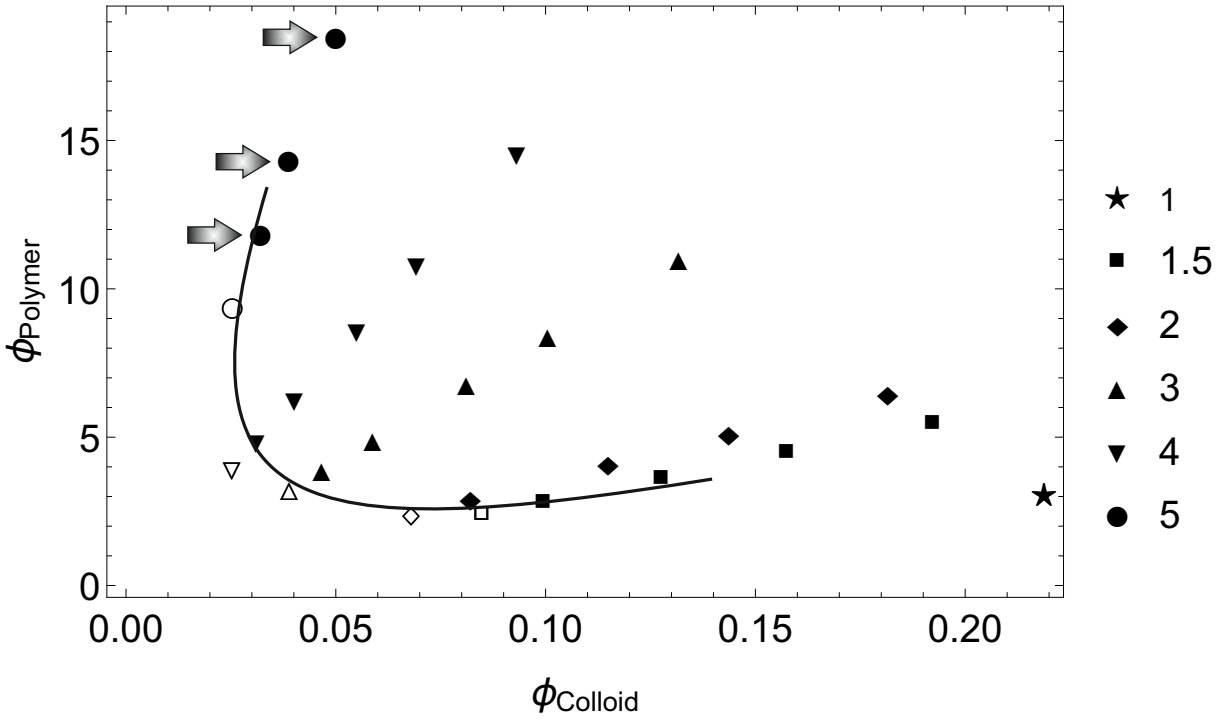


Figure 4.2: Phase diagram of PMMA-xanthan-water system. The filled symbols are the points of the two-phase region, and the open symbols are the points where the samples are not phase separating. The thick black line represents the approximate position of the binodal. The points of interest are shown by the arrows.

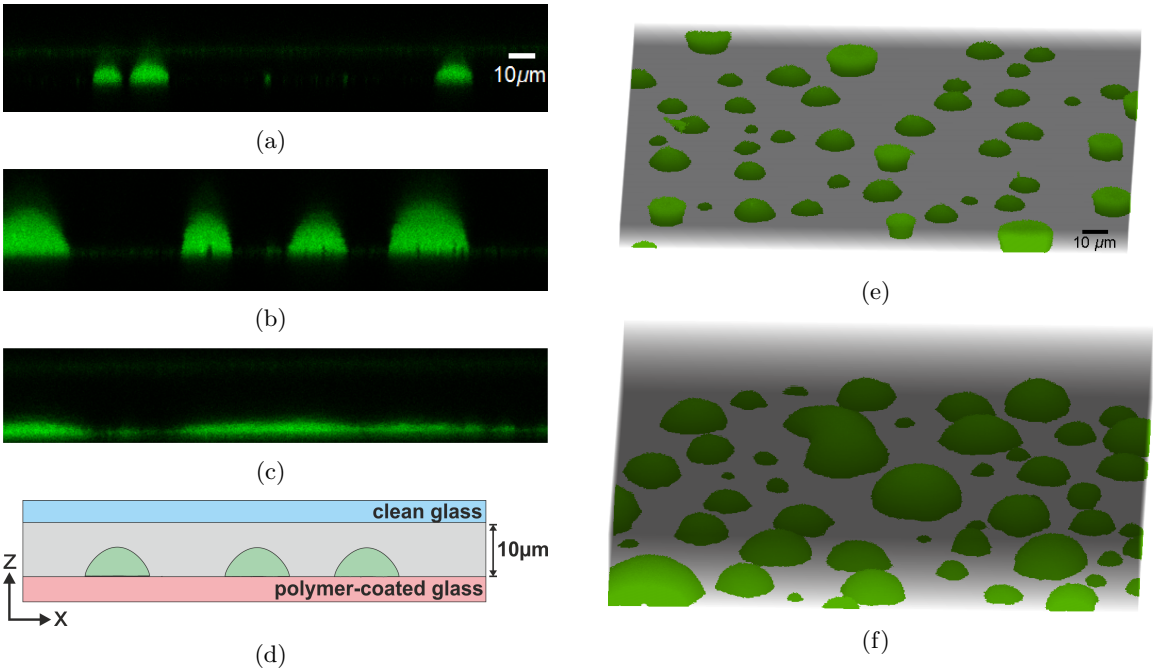


Figure 4.3: The xz plane images of colloid-polymer mixture at state point 5b taken after 180 min between (a) PAA-coated and clean glass walls, (b) chitosan-coated and clean glass walls, and (c) symmetric clean glass walls. The schematic diagram of the system is shown as (d). The reconstructed 3D images of the mixture from the raw data between (e) PAA-coated and clean glass walls, and (f) chitosan-coated and clean glass walls.

shows similar behaviour towards the two different kinds of polymer coating used. We observe that droplets of the colloidal liquid phase partially wet the coated wall. The schematic diagram of the system is shown in Figure 4.3(d).

As a reference, we have also looked at the behaviour of the colloid-polymer mixture towards symmetric clean glass walls used as a standard (Fig. 4.3(c)). In a similar experiment, Jamie et al. [165] have observed the behaviour of the colloid-polymer mixture that phase-separates via the nucleation and growth mechanism in a solvent mixture of 23% water and 77% glycerol on a glass slide. Jamie has described that the bright colloidal liquid phase starts to wet the glass walls due to the preferential wetting of the surface by the liquid phase. However, the liquid droplets that coarsen by coalescence in the bulk show no connection with the wetting layer on the wall. Thus, the wetting layer is attributable to the liquid droplets diffusing and coalescing on the wall surface, and consequently spread out across the wetting layer [165].

Apart from the quantitative measurement, it is also interesting to look at the raw images to gauge some ideas of the wetting behaviour of the colloid-polymer mixtures. Figure 4.4 shows the time lapse of the confocal images for PAA coating at state points 5a, 5b and 5c. We lay out the observations of the samples from the early times until 180 min where we believe that the samples have reached equilibrium. The network-like structure at the early times may be due to the shear developed from the two parallel walls, but these images show that even at 30 min, the colloid-polymer mixtures still exhibit the phase separating process to form droplets. Around this time, there is a break up of the network or coalescence of the droplets, implying an unstable morphology. However, at 60 min, the morphology seems more constant. Hence, it is a good judgment to consider the contact angle to be reliable after 60 min. At 180 min, the droplets seem to have a uniform size and are stable, which is another sign of equilibrium.

We reconstruct 3D images of the micrometer size fluorescent droplets from the raw data to obtain the drop shape profiles from which we can measure the contact angles (Fig. 4.3(e) and 4.3(f)). The confocal microscope z-stack images are binarised and we detect the surface of the droplet using an in-built function in Mathematica (Fig. 4.5(a) and 4.5(b)). The drop profile is constructed by calculating the average radius of the droplet for each z-stack slice. The error bar is the standard deviation in the radial average of the experimental droplet shape. We discard the innermost 20% of the average droplet profile as the top of the droplet is very noisy. In addition, any data points with a standard deviation bigger than one fifth of the radius is also

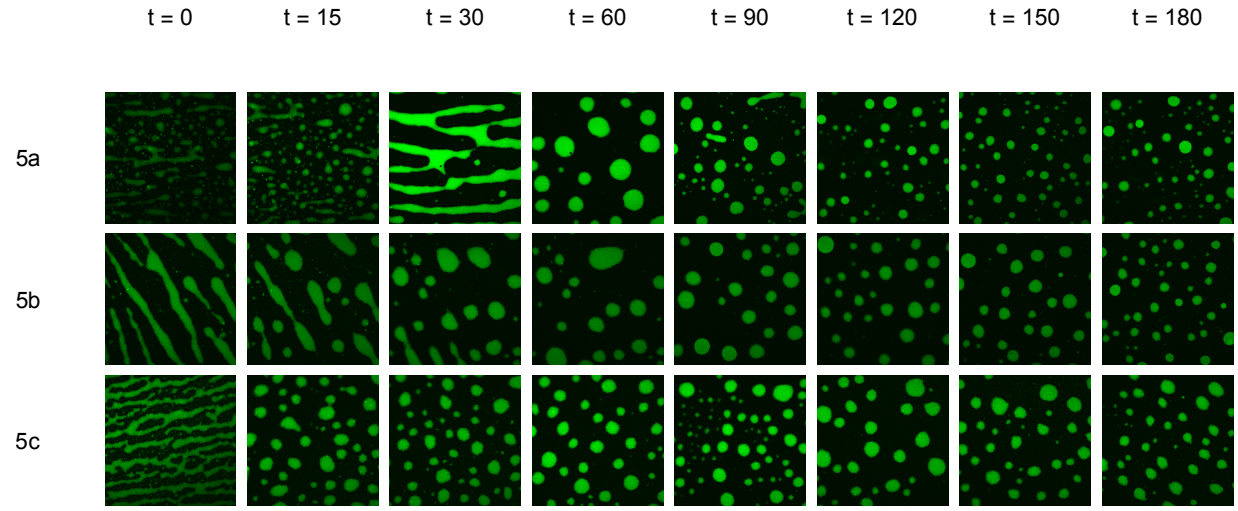


Figure 4.4: The time lapse images for PAA-coated walls at state points 5a, 5b and 5c, from the early times to 180 min.

rejected.

The drop profiles can now be fitted to the theoretical droplet shape that is given by Equation 4.6 obtained by minimising the free energy given in Equation 4.3 and the constant volume constraint (Eq. 4.4) which contribute to the Lagrange multiplier, λ, as shown in Figures 4.5(c) and 4.5(d). In order to fit the Euler-Lagrange equation to the experimental data, we use $L_c = 12$ µm obtained from the capillary waves analysis, the droplet radius, R, found from the droplet shape profile, and different values for λ. Different values of λ result in different theoretical curves from which we can find the best fit using the least squares method. 200 different values for λ are used for each droplet from which the best fitting curve is found. Another 200 curves are then generated close to the best fitting curve and again the best fit is determined (Fig. 4.5(e) and 4.5(f)). By taking the derivative of the best fitting curve at the base of the droplet and calculating the inverse tangent, we obtain the contact angle. This process is repeated for all the droplets in the frame with a radius of more than 1 µm to obtain an average value.

From the measurements done for state point 5b at after 180 min, it can be quantitatively concluded that the liquid droplets display partial wetting in the vicinity of the coated glass walls with a finite contact angle. The PAA-coated wall shows an average of $56^\circ \pm 3^\circ$ calculated based on 28 droplets, whereas the chitosan-coated wall displays a larger contact angle of $71^\circ \pm 5^\circ$ also based on 28 droplets. For the clean glass, we observe complete wetting, which is $\theta = 0^\circ$. This observed difference in contact angle proves that by altering the energy of the system by surface

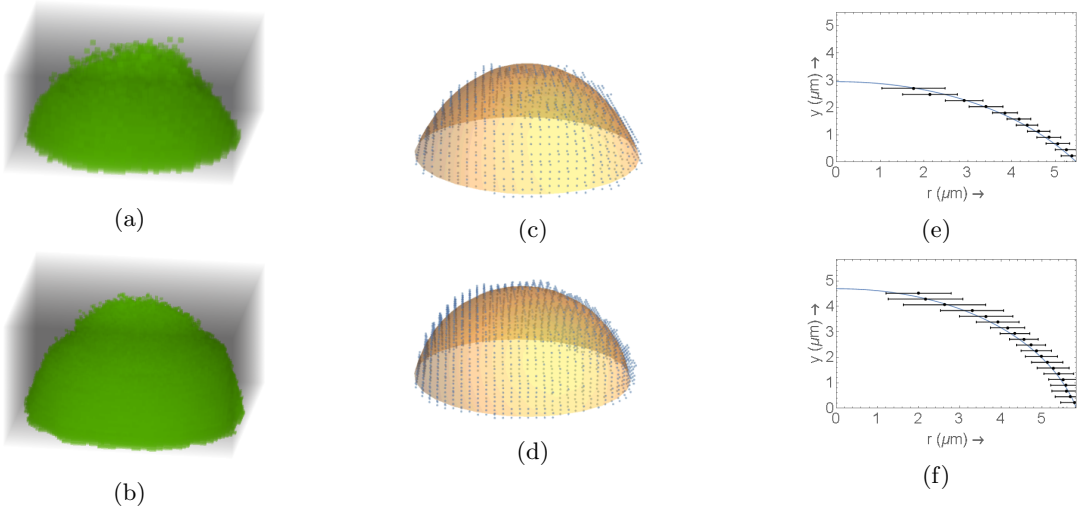


Figure 4.5: Fitting the drop profile of a sample at state point 5b, taken after 180 min: (a) a raw 3D droplet of PAA-coated wall, (b) a raw 3D droplet of chitosan-coated wall, (c) a 3D drop profile fitted to theoretical cap of a droplet on PAA-coated wall, (d) a 3D drop profile fitted to theoretical cap of a droplet on chitosan-coated wall, (e) the fitting curve with error bars of a droplet on PAA-coated wall, and (f) the fitting curve with error bars of a droplet on chitosan-coated wall.

modification, the contact angle can also be altered, described by Young's equation.

With a similar approach of measuring the contact angle mentioned above, we have done the measurement for the other two state points, 5a and 5c, as well. We have gathered data at five different time intervals between 60−180 min, with the number of droplets ranging from 20−50, taken at two different spots, for each time interval. Note that for the chitosan coating, we have only done the measurement at state point 5b. The average values of the contact angle are presented in Table 4.2. For clarity, we have plotted the values in graphs (Fig. 4.6). Figures 4.6(a), 4.6(b) and 4.6(c) show state points 5a, 5b and 5c for PAA coating from 60−180 min, respectively. We observe relatively small variations of the contact angle for state points 5a and 5b with time, possibly suggesting a small increase. Figure 4.6(c) shows no trend of the contact angle with respect to time. For the chitosan coating (Fig. 4.6(d)), the variations are much larger.

In addition to the early times, we have also measured the contact angle after 180 min for the PAA coating. We consider extended times at 210 min, 240 min, 5 hr and overnight. Figure 4.7 displays the plot of all the state points, at all the times we have measured the contact angle. This further illustrates that the system no longer changes considerably from 180 min onwards. Note that the overnight contact angle value we measured for state point 5a is not

Table 4.2: The contact angle θ in the time range of 60−180 min for PAA and chitosan coatings at state points 5a, 5b and 5c.

State point / Coating	**60 min**	**90 min**	**120 min**	**150 min**	**180 min**
5a PAA	46.44°	55.39°	60.20°	62.88°	55.10°
5b PAA	42.21°	46.20°	53.11°	56.01°	56.18°
5c PAA	46.30°	48.67°	45.97°	47.53°	52.50°
5b Chitosan	65.69°	86.06°	89.35°	65.45°	70.95°

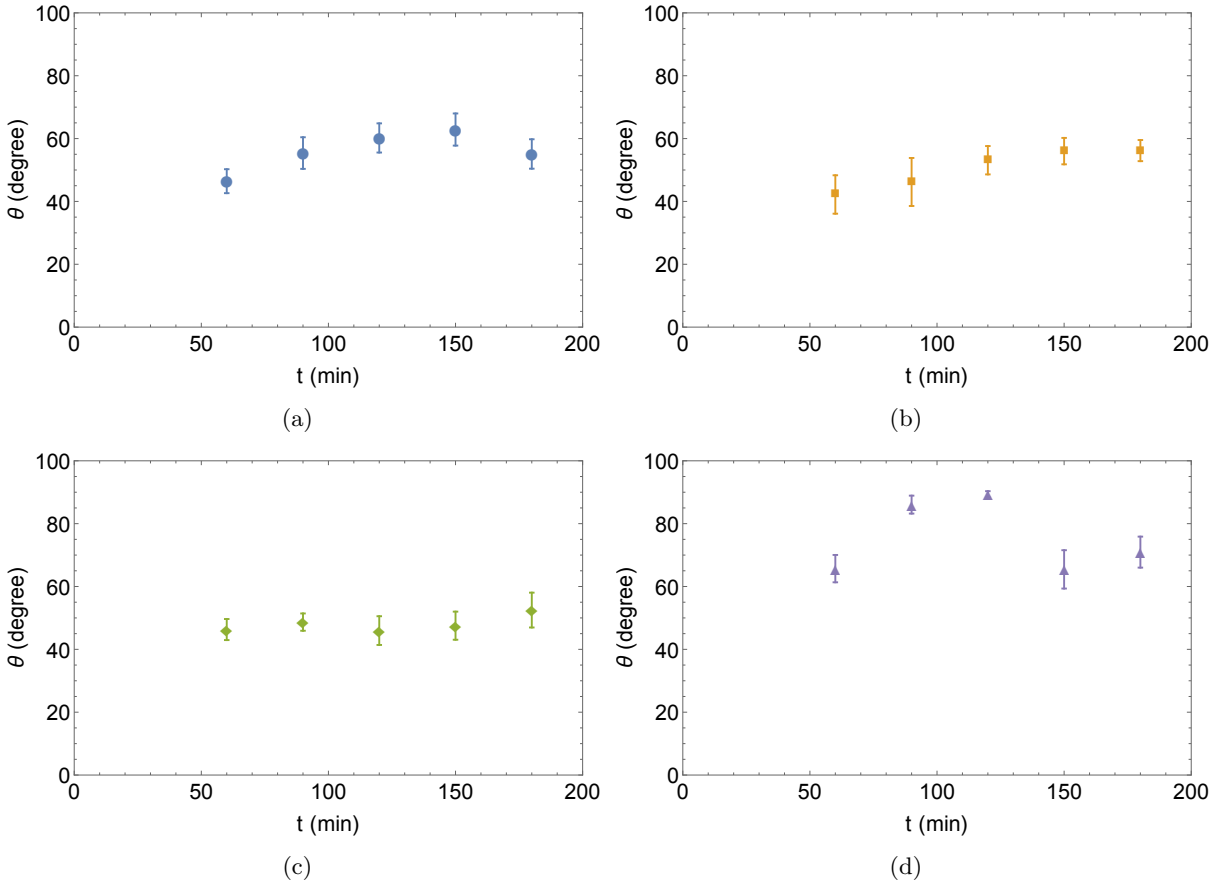


Figure 4.6: The contact angle θ versus time for (a) PAA coating at state point 5a, (b) PAA coating at state point 5b, (c) PAA coating at state point 5c, and (d) chitosan coating at state point 5b.

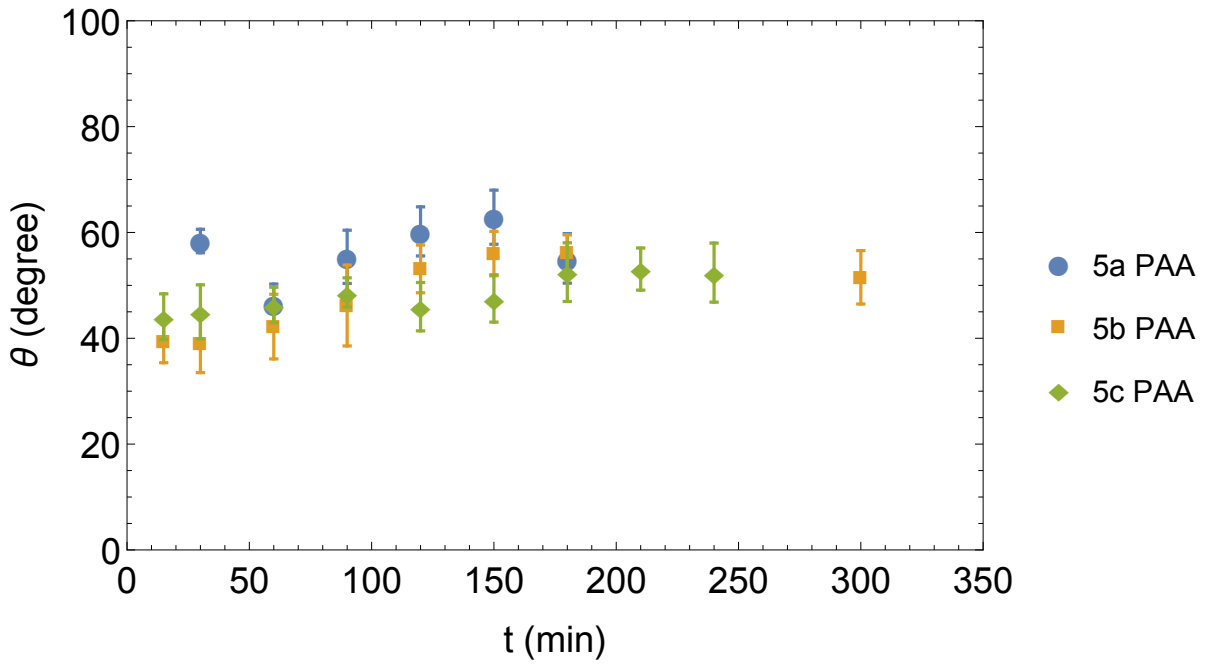


Figure 4.7: The contact angle θ versus time for PAA coating at state points 5a, 5b and 5c measured from the early to extended times.

plotted in the diagram, but the figure obtained as 52° is close to the one measured at 180 min. Surprisingly, and somewhat disappointingly, there is no trend between the contact angle and the state point for series 5. We had expected to see a decrease in contact angle on going from 5a to 5c. Interestingly, in the next chapter, such a change in the wettability is observed for different dilution lines.

Figure 4.8 shows a plot to compare the PAA and chitosan coatings in terms of the contact angle for state point 5b. It is clear that with different coatings, we obtain different contact angles. We can also see that the contact angle values are definitely higher for the chitosan than for the PAA coating. This demonstrates the capability of both polymers to change the wettability of a glass wall by exhibiting partial wetting. Given the time dependence, we believe that the PAA-coated walls show a more robust coating with a smaller variation as a function of time.

The robustness of the PAA coating may be suggested by the different regions of the sample slide that is probed to get two different images for each time interval. Figure 4.9 shows an example of a plot of two different images that we obtain by scanning different spots for each time interval. From the total number of the droplets between 20−50 for both images, we can see that there is only a small discrepancy between the different images. Hence, we expect that the

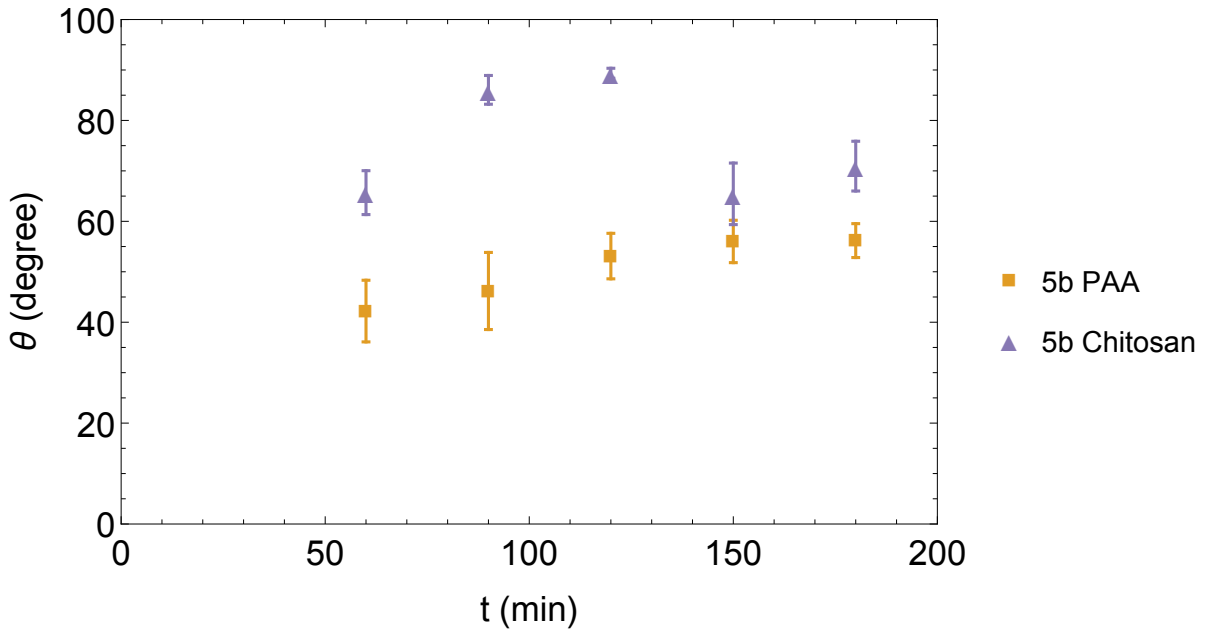


Figure 4.8: The contact angle θ versus time for PAA and chitosan coatings at state point 5b.

coating is uniform throughout the sample slide. On the other hand, the chitosan coating does not show the same consistency, as shown by the plot generated from two different images taken at two different spots for the same time interval (Fig. 4.10). This suggests that the chitosan coating is less uniform and may not be as robust.

Finally, we examine the possible role of the radius of the droplet. By looking at the raw confocal images (Fig. 4.4), we see that the size of the droplets gets somewhat smaller as the time increases and we are interested in possible effects on the contact angle. Therefore, we plot the distribution of the contact angle with respect to the droplet radius for PAA coating at state point 5a as shown in Figure 4.11. The distribution does not show a clear trend. At early times, the droplets are somewhat larger (the size range of 10−20 µm). The majority of the droplets, however, falls into the 4−10 µm size range. Similar observations can be made for 5b (Fig. 4.12), but 5c seems less time-dependent (Fig. 4.13). For the chitosan coating at state point 5b as shown in Figure 4.14, there is again no trend. More importantly, at any given time, there is no clear dependence of the contact angle with the radius (Fig. 4.15). This suggests that a possible line tension does not play a role in this system.

Finally, we note that contrary to a recent publication [150], we have not used the line tension to analyse our results. Their system consists of PMMA colloids and non-adsorbing polystyrene (PS) polymer, with colloid-to-polymer ratio $q = 1.18$, interfacial tension $\gamma_{\text{exp}} = 0.13$

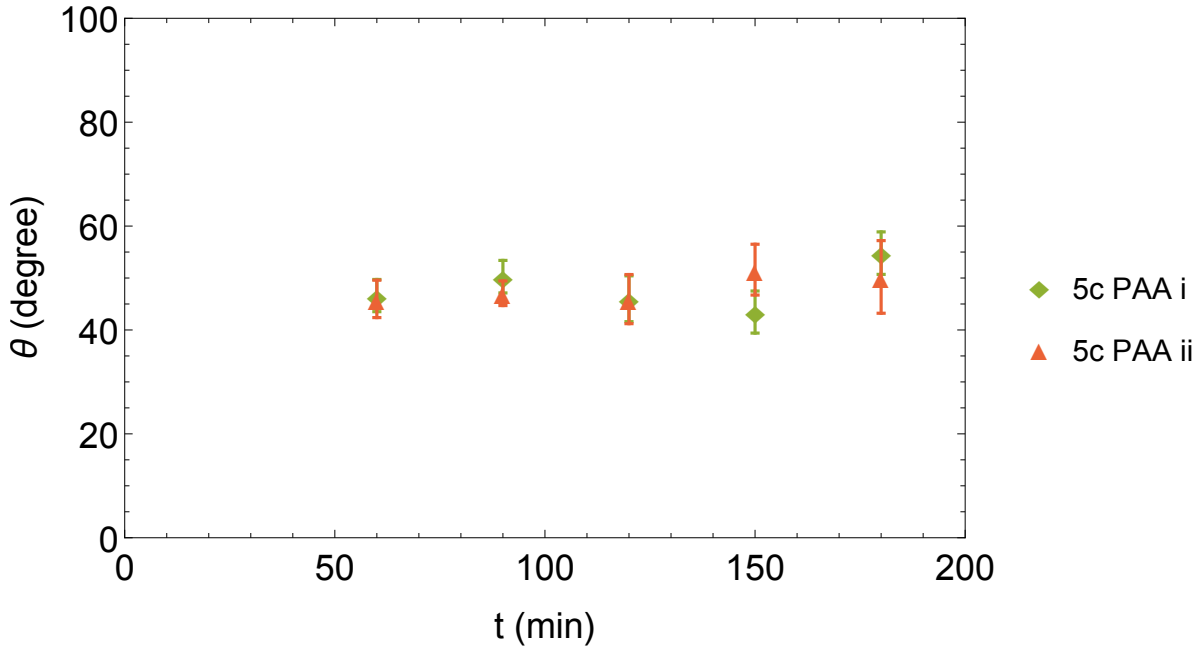


Figure 4.9: The contact angle θ versus time for PAA coating at state point 5c for droplets measured at two different regions of the sample slide.

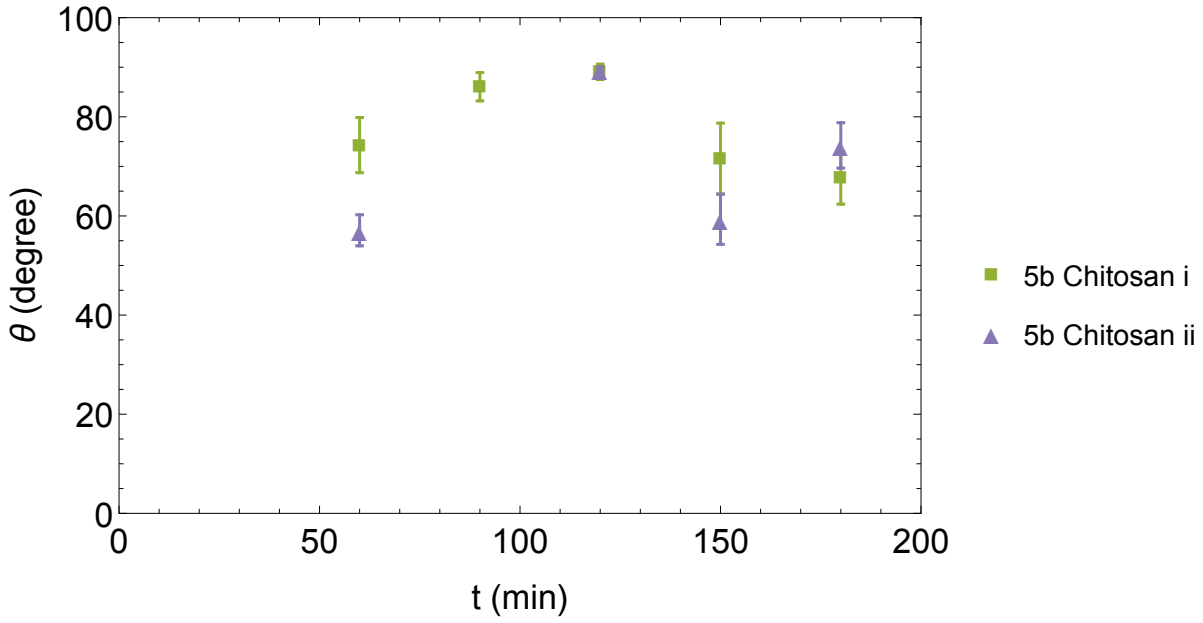


Figure 4.10: The contact angle θ versus time for chitosan coating at state point 5b for droplets measured at two different regions of the sample slide.

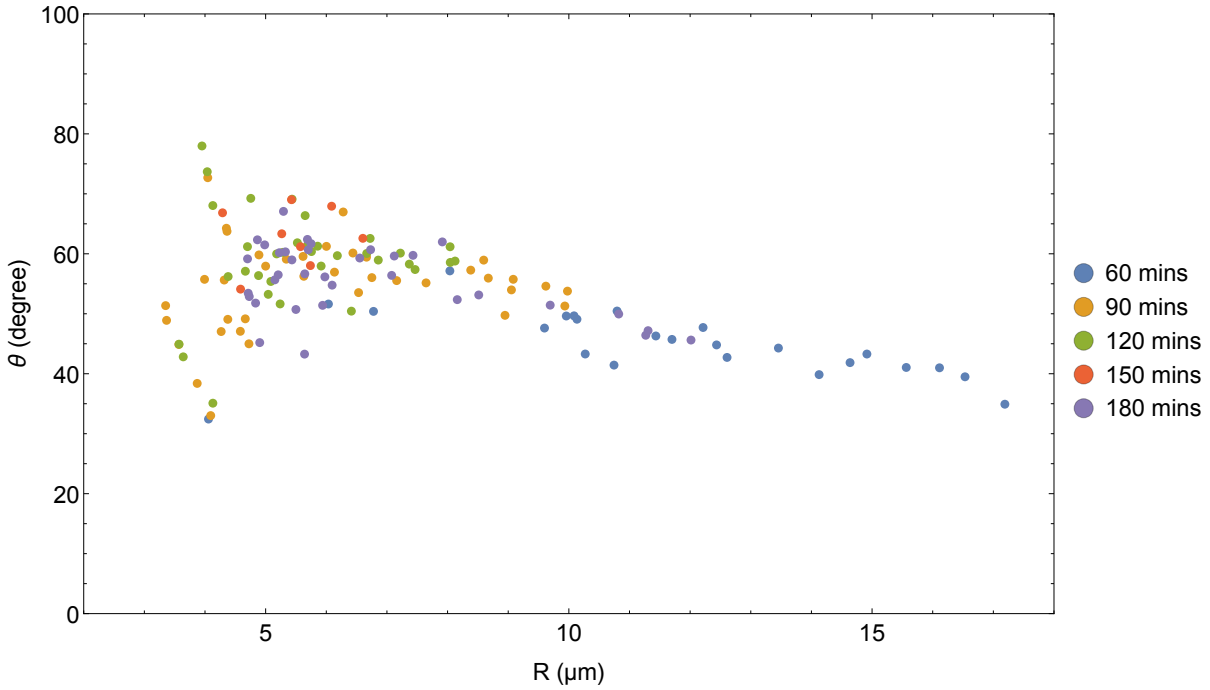


Figure 4.11: The droplet distribution of the contact angle θ versus radius of the droplets for PAA coating at state point 5a.

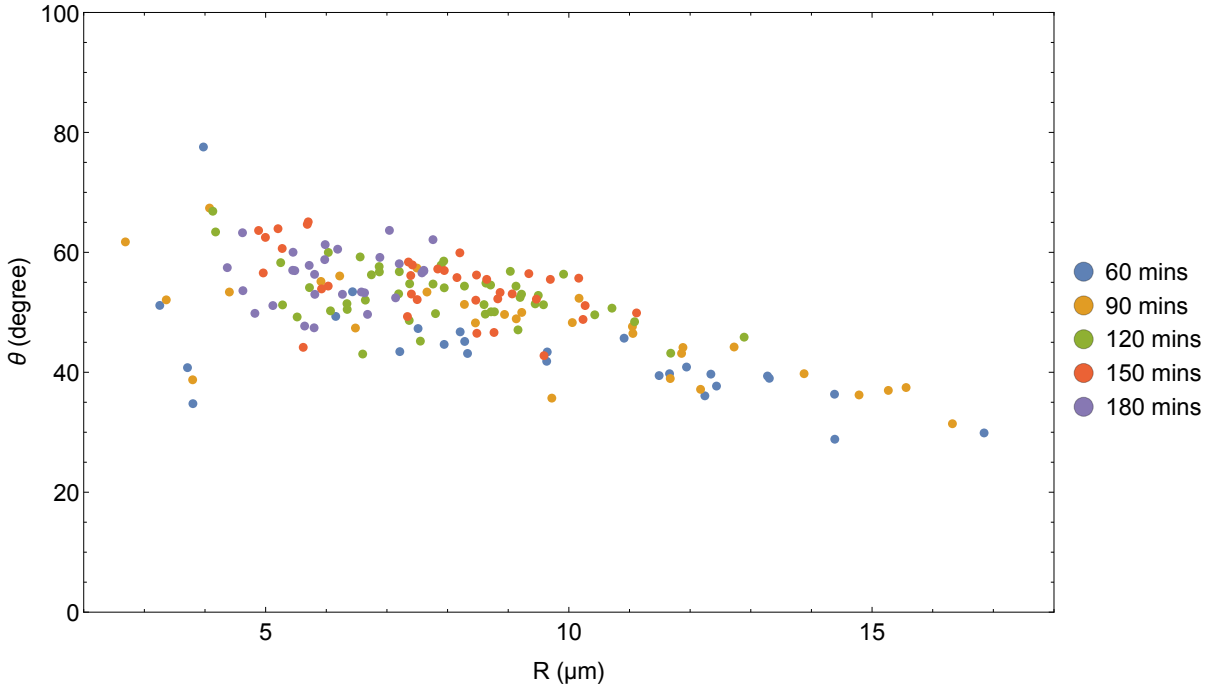


Figure 4.12: The droplet distribution of the contact angle θ versus radius of the droplets for PAA coating at state point 5b.

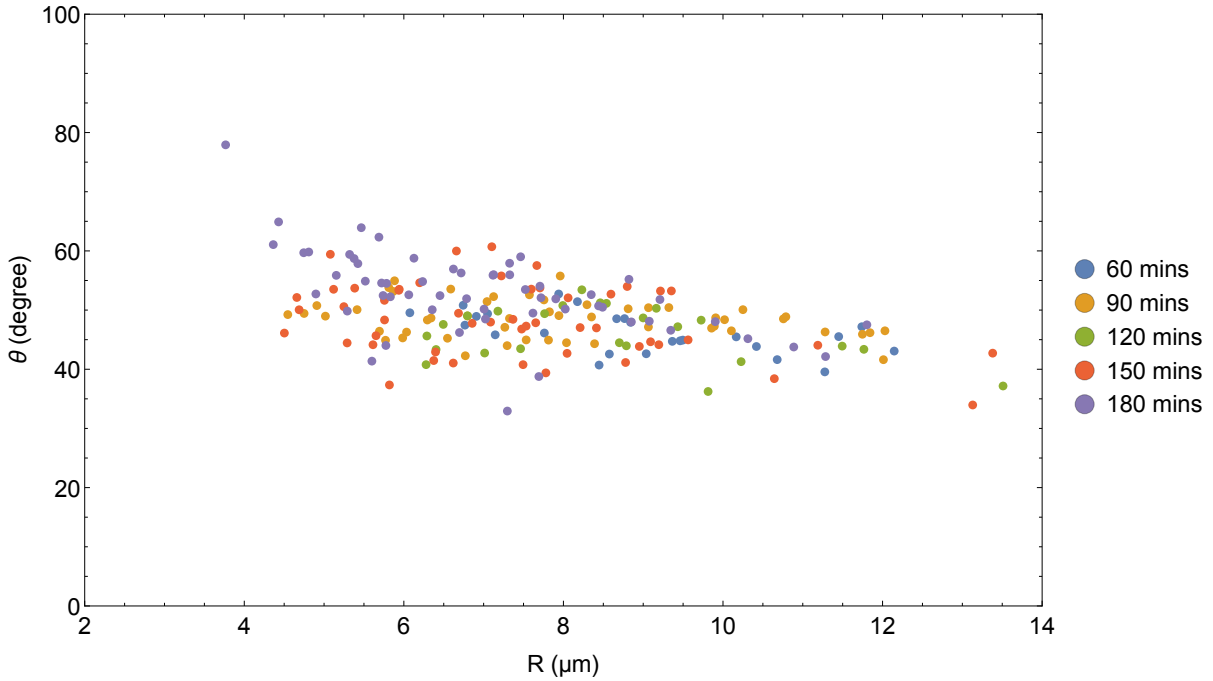


Figure 4.13: The droplet distribution of the contact angle θ versus radius of the droplets for PAA coating at state point 5c.

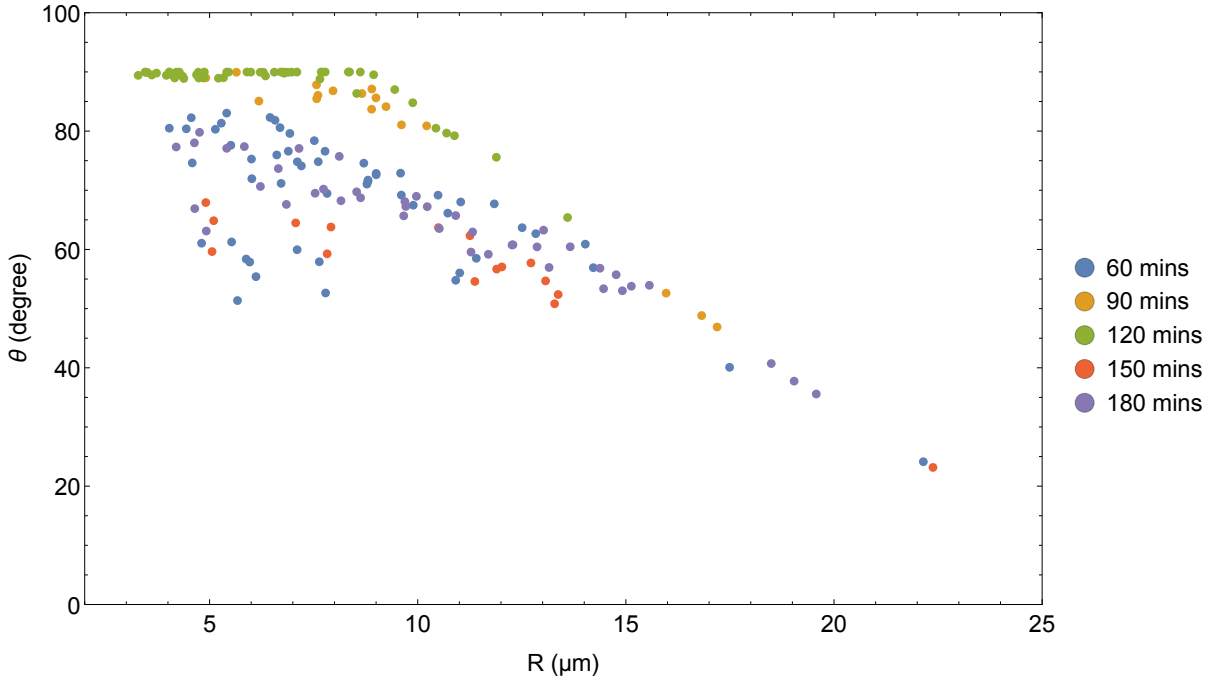
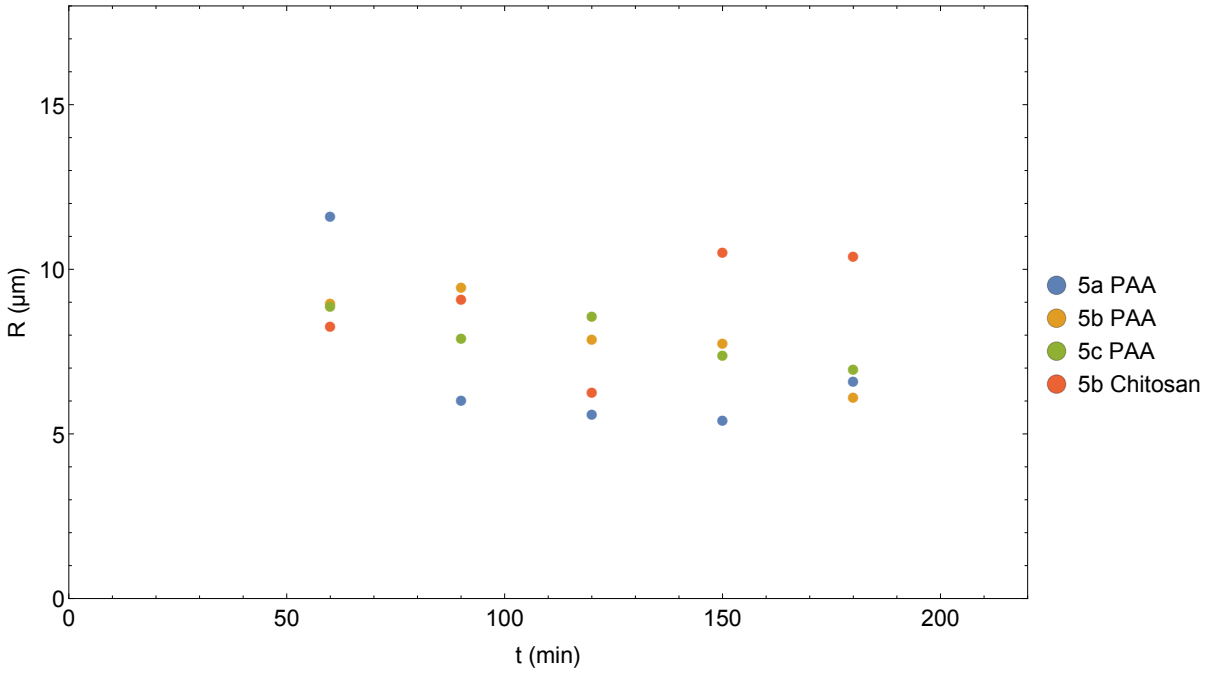
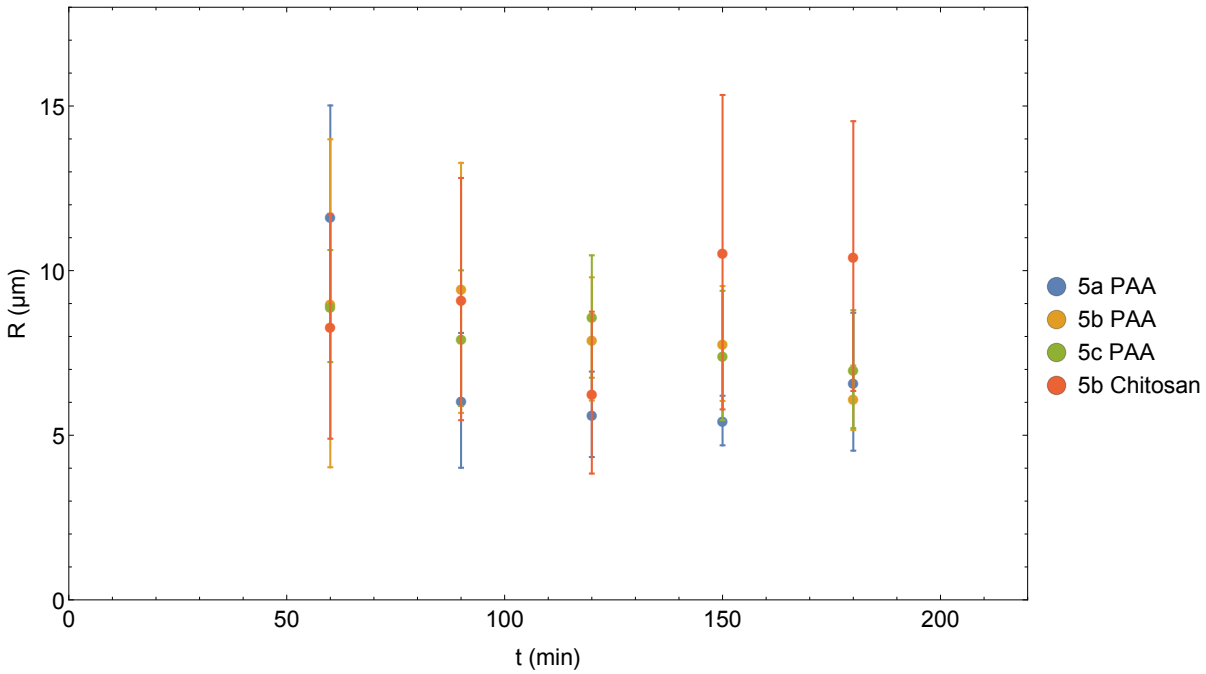


Figure 4.14: The droplet distribution of the contact angle θ versus radius of the droplets for chitosan coating at state point 5b.



(a)



(b)

Figure 4.15: The mean values of droplet radius versus time for all state points on PAA and chitosan coatings, shown (a) without error bars for clarity, and (b) with error bars.

$\pm$ 0.01 µN m^{-1}, capillary length $L_c = 25 \pm 5$ µm, and hence $\Delta\rho \sim 20$ kg m^{-3}. From the experimental parameters, they compared the contact line of a colloid-rich liquid droplet with the theoretical equivalent to predict the contact angle formed. From the theoretical $\gamma = 3.2$ µN m^{-1}, the predicted contact angle at $q = 1.18$ is 59°. This is far from the experimental contact angle that is obtained from a simple fitting of the foot of the droplet's cross-section to a spherical cap. The contact angle was estimated to be 30°, even though the spherical cap does not entirely describe the droplet [150]. It would be interesting to use our theoretical model on their droplet.

4.5 Conclusion

In summary, we have shown that colloid-polymer mixtures are a good model system in studying wetting through microscopic contact angle measurements. The fitting of the drop profile to the theoretical curves based on the Euler-Lagrange equation also proves that this method is reliable in measuring contact angles accurately. By altering the solid glass substrate using polymers, we could observe the changes in wettability of the system from wetting to partial wetting. Two different kinds of polymer used to modify the surface, polyacrylamide and chitosan, exhibit different contact angle values. No clear trend as a function of state point has been observed. The possible line tension did not need to be taken into account to describe the drop shape.

Acknowledgements

We thank Professor Carlos Rascón for the contribution of the theoretical part, and Professor Andrew Parry for stimulating discussions. Dr. Kira Klop is thanked for the help with the fitting of the drop profiles.

Chapter 5

Wetting Transition in Colloid-Polymer Mixtures at Polymer-Coated Walls

ABSTRACT

We study the wetting behaviour of colloid-polymer mixtures. To this end, we use the system introduced in Chapter 2 and follow the wetting behaviour along four different dilution lines. We observe a wetting transition from partial to complete wetting upon dilution for three dilution lines. The dilution line consisting the lowest percentage of the colloidal liquid phase displays partial wetting in all the two-phase regions.

5.1 Partial to complete wetting

When a liquid drop is placed on a solid substrate, we may either find partial or complete wetting. The same substrate can also demonstrate a transition in wetting behaviour by a modification in the thermodynamic variable, for instance in either the temperature or the chemical potential. The transition of this wetting behaviour from partial to complete wetting is known as the wetting transition.

According to Young's law, wetting of a system takes place when three phases coexist, with at least one phase of liquid, and not more than one solid phase. The wetting behaviour is determined by the formation of the static contact angle, θ, that is associated with the interfacial tension of the three phases, γ, based on the Young's law [16]:

$$\gamma_{SG} = \gamma_{SL} + \gamma_{LG} \cos\theta \tag{5.1}$$

with the subscripts of S, L, and G indicating the solid, liquid and gas, respectively. When the liquid completely wets the substrate, the contact angle formed is 0°, and this is known as complete wetting. If the contact angle is $0° < \theta < 90°$, the substrate is partially wet by the liquid. The state identified as partial drying occurs when $90° < \theta < 180°$, and at the other extreme, complete drying happens when θ is equivalent to 180°. The degree of the contact angle is determined by the force balance at the three-phase contact line, by considering each of the three interfacial tensions as a force per unit length that the interfaces exert on the contact line along which they are joined up. Imagine that we have a liquid droplet partially wet a substrate. At this point, the interfacial tension of the solid-gas is less than the total of the other two interfacial tensions ($\gamma_{SG} < \gamma_{SL} + \gamma_{LG}$). By changing a thermodynamic variable, for example the temperature, the three interfacial tensions will change and consequently the contact angle will also change. At some point, this may lead to the state where the sum of the solid-liquid and the liquid-gas interfacial tension becomes equal to the solid-gas interfacial tension ($\gamma_{SG} \equiv \gamma_{SL} + \gamma_{LG}$). At this particular point, the contact angle is zero and the system is considered to have reached complete wetting when a uniform liquid layer spreads out on the substrate (please refer to Figure 5.1) [138, 166, 167].

The wetting transition can be determined experimentally by measuring two different quan-

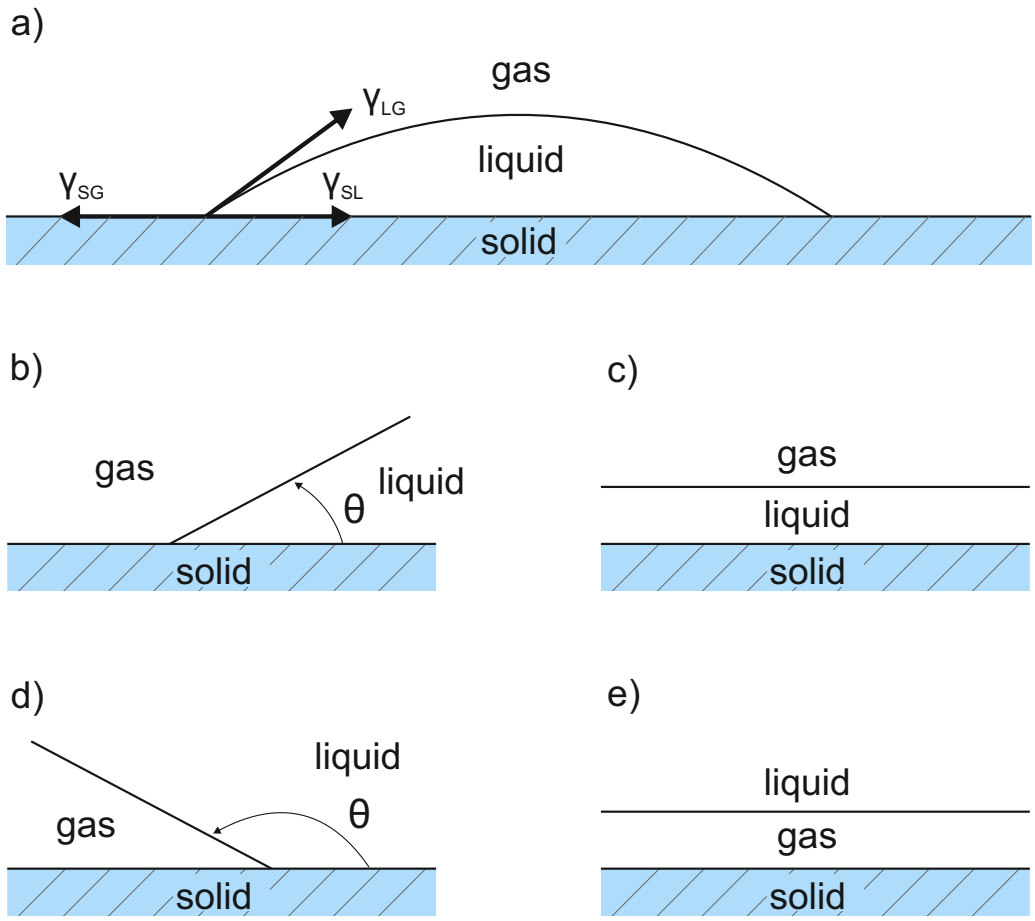


Figure 5.1: Coexistence of liquid, gas and solid substrate, with (a) a liquid droplet partially wets a solid substrate with the solid-liquid, liquid-gas and solid-gas interfacial tensions, (b) partial wetting of the substrate, (c) complete wetting of the substrate, (d) partial drying of the substrate, and (e) complete drying of the substrate.

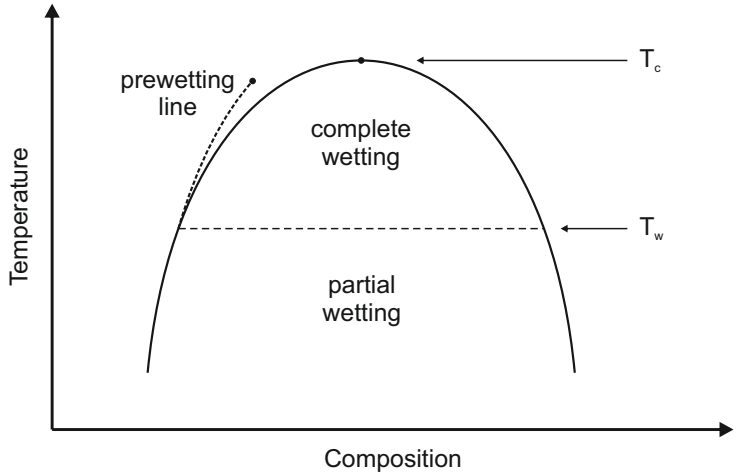


Figure 5.2: The wetting transition phase diagram predicted by Cahn in 1977. Complete wetting occurs close to the critical point, T_c, and the transition of partial to complete wetting is marked by the wetting temperature, T_w. The prewetting line indicates the first order wetting transition that extends into the one-phase region and terminates in a surface critical point [168].

tities namely the contact angle or the thickness of the adsorbed film on the substrate. The transition can be examined as a function of temperature along the bulk coexistence line, a region in the phase diagram where in a binary liquid system, the two liquids are at coexistence. The temperature at which the wetting transition occurs is known as the wetting temperature, T_w [166]. At this temperature, the contact angle that is formed in the partial wetting state disappears, and the contact angle becomes zero from this temperature up to the critical temperature, T_c [138]. In 1977, Cahn [168] has predicted that on approach of the critical point in a binary fluid mixture system with one inert substrate, a wetting transition always occurs (Fig. 5.2). As mentioned above, the wetting transition occurs when γ_{SG} is equal to the sum of $\gamma_{SL} + \gamma_{LG}$, or when $\gamma_{SG} - \gamma_{SL}$ is equal to γ_{LG}, which is when the liquid phase spreads out on the solid substrate. Cahn's argument involves scrutinising the dependence of the surface free energy to the temperature close to the critical point for both the γ_{LG} and $\gamma_{SG} - \gamma_{SL}$ [168, 169]. Cahn stated that the density (or composition) difference of the liquid and gas phases determines the interfacial tensions of the solid-liquid and solid-gas. It is known that this density difference vanishes at the critical point with an exponent defined as β_1. As $T \to T_c$, the relation is $\gamma_{SG} - \gamma_{SL} \propto (\rho_L - \rho_G) \propto |T - T_c|^{\beta_1}$ where the value of the exponent $\beta_1 \approx 0.8$. On the other hand, as $T \to T_c$, the liquid-gas interfacial tension, γ_{LG}, reaches zero at the critical point with the exponent μ, which gives $\gamma_{LG} \propto |T - T_c|^{\mu}$, with $\mu \approx 1.26$ [169]. The fact that $1.26 > 0.8$ shows that at some temperature close to the critical point, there is inequality of $\gamma_{SG} - \gamma_{SL} > \gamma_{LG}$ that will turn to an equality, and a wetting transition occurs [166, 168, 169].

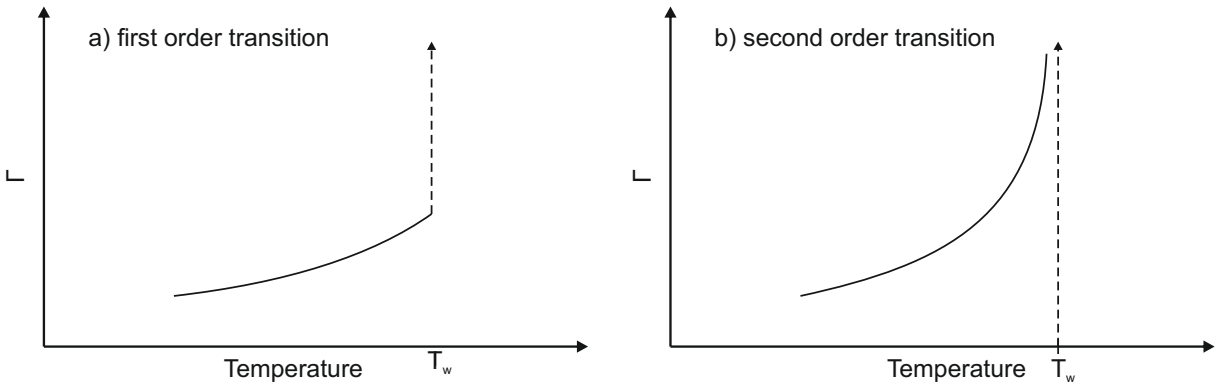


Figure 5.3: Liquid adsorption as a function of temperature along the three-phase coexistence line when (a) the wetting transition is a first order transition, and (b) when the wetting transition is a second order or continuous transition [169].

Theoretically, we can classify the wetting transition into two categories based on the surface free energy of the system related to its interfacial tension. If the first derivative of the surface free energy-temperature curve occurs abruptly and shows discontinuity at the wetting temperature, the wetting transition is known as first order. However, if the first derivative of the free energy is continuous at the transition point, the wetting transition is termed second order or critical wetting transition. The first order wetting transition usually occurs farther from the critical point, whereas the second order wetting transition happens when it is driven close to the critical point [166]. This critical wetting transition may experience long-range critical wetting due to the long-range Van der Waals forces that is preceded by a first order wetting transition, or short-range critical wetting when the layer thickness diverges in a continuous fashion from a microscopic to a macroscopically thick film [166]. These two types of wetting transition can also be determined experimentally from the contact angle or the thickness of the adsorbed liquid film on the substrate, Γ, which is between the thin and thick adsorbed films. For the first order wetting transition, the microscopically thin liquid adsorption on the substrate remains the same, but it jumps to the infinite (in principle) macroscopic thick film at the wetting temperature. The discontinuity in the film thickness is depicted in Figure 5.3(a). On the other hand, the second order or the critical wetting transition exhibits a continuous liquid film adsorption divergence on approach to the wetting temperature (Fig. 5.3(b)) [169].

For the first order wetting transition, Cahn has shown that the thin-thick liquid film thickness can happen outside the three-phase coexistence, known as the prewetting (Fig. 5.2) [168]. Along the three-phase coexistence line, there is a finite liquid adsorption below the T_w and an infinite adsorption above it. We know that the first order wetting transition experiences

a jump from a thin microscopically finite layer to an infinite liquid adsorption at T_w in the bulk phase. However, in the gas-substrate region close to the three-phase coexistence, the discontinuity of the liquid adsorption still happens, but it is meant to remain finite along the prewetting line. Hence, the microscopically thin liquid layer increases in thickness, but still with the finite microscopic thickness. The formation of the layer is analogous to the fact that the difference in the interfacial tension of the three phases implies the free energy cost to form a surface area of the substrate that has a direct contact with the gas phase (recall that the interfacial tension is the free energy per unit area). Hence, it is always more favourable for the system to create a surface area where the liquid phase intervenes between the substrate and the gas phase as this costs less free energy to the system. Consequently, there is always an increase in the liquid layer adsorption even though only at finite thickness. From Figure 5.2, it can be seen that this prewetting line extends from the wetting transition point at bulk coexistence, to a prewetting or surface critical point, where the adsorption difference between the thin and the thick layer vanishes, similar to the density difference between the liquid phase and the gas phase that vanishes at the ordinary or bulk critical point [166, 169].

Wetting transition phenomena have been predicted to be of the first order or second order. Having the theoretical predictions in hand, it is interesting to have it observed experimentally. Some experimental work has shown that wetting transition can display the first order or the second order regime. This is made possible with the measurement of either the contact angle or the thickness of the adsorbed film on the substrate [166]. In 1980, Moldover and Cahn [170] have shown experimentally the first order wetting transition by measuring the contact angle of partially miscible liquids which are mixtures of methanol, CH_3OH, and cyclohexane, C_6H_{12}. They measured the contact angle of the methanol-rich phase at the liquid-vapour interface of the cyclohexane-rich phase, and showed that the as they moved far from the critical temperature, T_c, the contact angle increased from zero to non-zero. The changes in the wetting behaviour was induced by addition of water that raised the T_c, and equivalently lowered the temperature of the whole system. They plotted the cosine of the contact angle as a function of the mole fraction, X, of water added to the methanol-cyclohexane mixture. At the ambient temperature of 22 °C, they found that for $X \leqslant 0.020$ the methanol-rich droplets spread into a film that completely wet the cyclohexane-rich liquid-vapour interface, but above this value, the droplets were stable at the interface. Hence, it showed that at the crossover of $X = 0.020$, there is a wetting transition from complete to partial wetting. The discontinuity at this point implies that

the wetting transition is of the first order [166, 170].

In ordinary molecular systems, it is the temperature that affects the phase behaviour of the compositions. However, in a colloid-polymer system, the phase diagram is constructed by changing the concentrations of the mixture as this influences the system. Thus, as for a relation, one may assume that $T \sim 1/c_p$ where c_p is the polymer concentration [171]. Experimental attempt to observe the wetting transition using colloid-polymer mixtures has been previously done by Wijting et. al [139, 140]. Using a colloid-polymer mixture of silica-poly(dimethylsiloxane) (PDMS) dispersed in cyclohexane, they have measured the contact angle of the colloid-polymer interaction with a hard wall, as well as with a PDMS-modified glass fiber denoted as soft wall. As for the hard wall, they managed to observe a partial wetting of the hard substrate by the colloidal liquid phase further away from the critical point. This meniscus, however, vanished as they scanned the phase diagram closer to the critical point, and this displayed the complete wetting of the substrate. On the other hand, the soft wall with a fluffy polymer layer at the surface showed that the contact angle of the colloidal liquid phase on the substrate is more than 90°, and this implied a partial wetting of the gas phase (or partial drying) further from the critical point. Interestingly, as they moved closer to the critical point, they could observe the complete drying of the soft wall. Both wetting transitions that they observed have occurred in the range of the polymer packing fraction of $4.3 < \phi^r_{pol} < 4.5$. However, due to the insufficient accuracy of their experimental data, they could not conclude their observations of the wetting transition to fall under first order or critical transition. They, nevertheless, made a remark that the transition might either be second order or weakly first order [139, 140]. Furthermore, note that their experimental method has been put into question by Aarts et. al [33].

5.2 Experimental systems

For the wetting transition observations, we have prepared four colloid-polymer mixtures of different state points from our fluorescently labelled poly(methylmethacrylate) (PMMA) colloidal particles of radius $R_c = 110$ nm and non-adsorbing xanthan polymers of radius of gyration $R_g = 264$ nm. Figure 5.4 shows the position of the state points, labelled as 1.5, 2, 3 and 5 in the phase diagram, with an arrow corresponding to the dilution line towards the binodal for each state point. The state points along the dilution line are marked as ‘a’, ‘b’, ‘c’, ‘d’, ‘e’ and ‘f’.

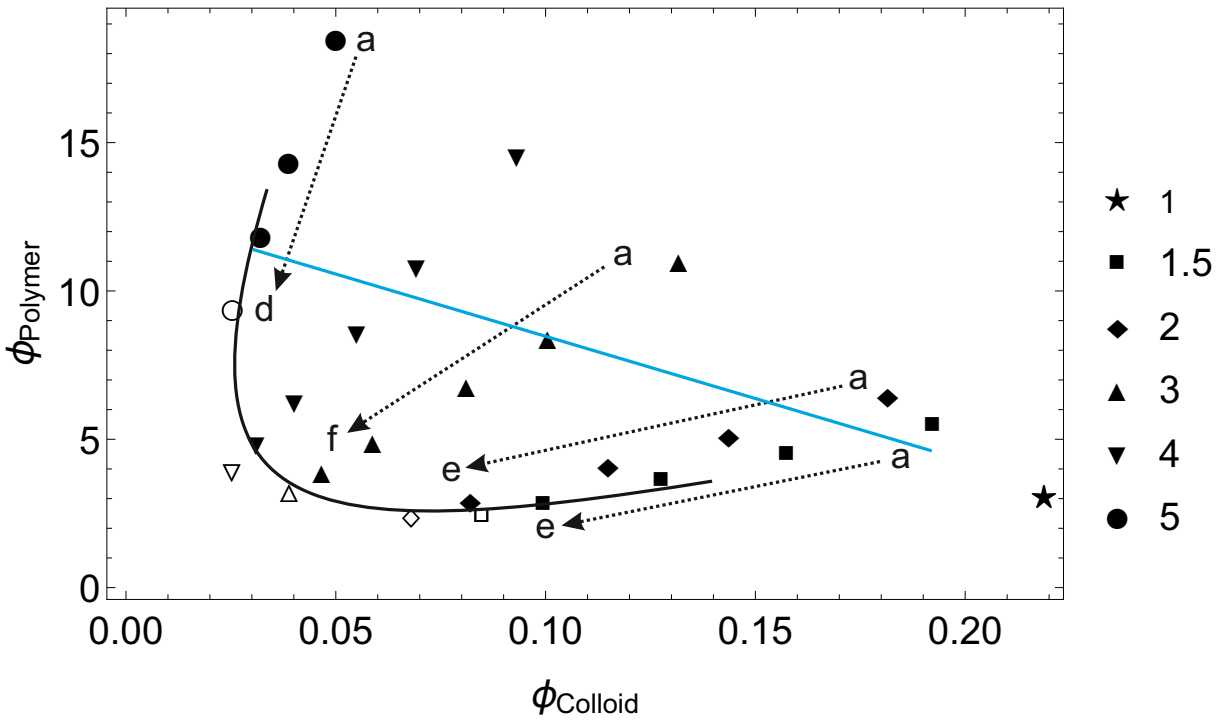


Figure 5.4: Phase diagram of PMMA-xanthan-water system. The filled symbols are the points of the two-phase region, and the open symbols are the points where the samples are not phase separating. The thick curved black line represents the approximate position of the binodal. The solid blue line represents the wetting transition line. The dilution lines of state points 1.5, 2, 3 and 5 are shown with an arrow pointing in an alphabetical order for each diluted state point.

The initial concentration and volume fraction of each state point is mapped out in Table 5.1.

The colloid-polymer mixtures are confined between two glass walls with approximate spacing of 10 µm, with one wall coated with polyacrylamide (PAA) polymer that serves as a base wall. Alongside PAA, we have also done the same experiment using chitosan-coated walls with samples of state points 2 and 3 (Please refer to the Appendix for the observations). The phase separation of the colloid-polymer mixtures into a colloid-rich, polymer-poor phase (liquid phase) and a colloid-poor, polymer-rich phase (gas phase) enables us to observe the wetting behaviour using laser scanning confocal microscopy (LSCM) in three dimensions, and the data is recorded between 60−180 mins. The state points are prepared along the dilution line until they reach the binodal line with only the existence of one phase of the mixtures. The methods and preparations of the colloid-polymer mixtures and the surface modification technique used to coat the glass wall are presented in detail in Chapter 2.

Table 5.1: The initial concentration (denoted as 'c') and volume fraction (denoted as 'ϕ') of PMMA colloid and xanthan polymer at state points 1.5, 2, 3 and 5.

State point	**PMMA**	**Xanthan**	**PMMA**	**Xanthan**
1.5	$c_c = 0.225$ g/ml	$c_p = 4.88 \times 10^{-4}$ g/ml	$\phi_c = 0.19$	$\phi_p = 5.51$
2	$c_c = 0.212$ g/ml	$c_p = 5.76 \times 10^{-4}$ g/ml	$\phi_c = 0.18$	$\phi_p = 6.50$
3	$c_c = 0.154$ g/ml	$c_p = 9.79 \times 10^{-4}$ g/ml	$\phi_c = 0.13$	$\phi_p = 11.05$
5	$c_c = 0.059$ g/ml	$c_p = 1.64 \times 10^{-3}$ g/ml	$\phi_c = 0.05$	$\phi_p = 18.54$

5.3 Qualitative results and discussion

The wetting behaviour of these samples were observed under confinement in the vicinity of polyacrylamide-coated glass wall. Colloid-polymer mixtures have proven to be a good model to study wetting phenomena, and in our system, the formation of liquid droplets and gas bubbles with a sharp interface enable us to observe the wetting behaviour efficiently (see Chapter 4). We have observed a complete wetting regime conveniently with our colloid-polymer mixtures on a hard glass wall, either in confinement or in bulk, at all state points, as partly shown in the previous chapters. Similar colloid-polymer mixtures exhibiting the complete wetting behaviour have also been experimentally shown by Aarts et. al [33] and Jamie et. al [165, 172]. We have also witnessed the capability of our colloid-polymer mixtures to exhibit a partial wetting regime in the vicinity of a polymer-coated wall (presented in previous chapters). Hence, it is intriguing to see if these colloid-polymer mixtures will be in corroboration with Cahn's prediction. Given the difficulties of measuring the contact angle for even a single state point (Chapter 4), we have opted here to make solely qualitative observations.

Figure 5.5 shows the LSCM z-stack side views (xz and yz views) of a colloid-polymer mixture at state point 1.5 and subsequent state points along the dilution line towards the binodal (please note that the polyacrylamide-coated wall is positioned on the top in all the images, but as a base wall in the experiment). From this figure, we can see that at state point 1.5a, the sample shows partial wetting in the vicinity of the polymer-coated wall. At this state point, the colloidal liquid phase is more abundant, and the colloidal gas phase appears as gas bubbles (please refer to the Appendix for the complete LSCM images of the mixtures). This

image displays a wetting contact angle of less than 90° by the colloidal liquid phase. The partial wetting is due to the reduced strength of the depletion interaction between the colloidal particles with the coated wall, whereby the existence of a polymer brush layer on the substrate forms an excluded volume that repels the colloidal particles. It is also interesting to note that the interaction of the colloidal gas phase with the polymer-coated substrate implies that the colloidal gas phase, which is less dense than the colloidal liquid phase, acts against gravity by staying at the bottom of the confinement wall. Apart from the reduced strength of the depletion interaction, an even more microscopic picture suggests that the entanglement of the xanthan polymers (which is mainly the colloidal gas phase) with the polyacrylamide brush layer should also been taken into consideration. Finally, we note that the uncoated glass wall is completely wet by the colloidal liquid phase, despite the gravitational cost for the denser liquid phase at the upper wall.

Moving from state point 1.5a to state point 1.5b where we move closer to the binodal line, the sample starts to show complete wetting with the substrate. This point can be considered as just after the wetting temperature, T_w, for this particular state point where the contact angle has become zero, implying the formation of a liquid layer that spreads on the substrate. As aforementioned in Section 5.1, we can conveniently monitor the wetting transition by measuring the contact angle formed by our system. Relating to the contact angle, the partial wetting at state point 1.5a suggests that the inequality of the three-phase interfacial tensions to be $\gamma_{SG} < \gamma_{SL} + \gamma_{LG}$, but transforms to $\gamma_{SG} \equiv \gamma_{SL} + \gamma_{LG}$ when the complete wetting is reached at state point 1.5b [166, 169]. Wessels et. al [173] have performed a theoretical calculation on the contact angle that is formed based on the Asakura-Oosawa-Vrij (AOV) model of hard sphere colloids and ideal polymers at the size ratio $q = 0.6$ and $q = 1$. They have calculated the interfacial tensions of the three phases and the colloid layers adsorbed on the wall that is referred to as the nth layering transition, and inserted the data to the Young's equation to obtain a contact angle curve, θ_n, for each n-layer state. They have shown that the lowest solid-gas interfacial tension possesses the largest value of the contact angle. The liquid adsorption, Γ, at the wall shows a discontinuity at the bulk coexistence upon crossing a layering transition that can be shown by the polymer packing fraction, η_p^r. A range of metastable states has also been found, corresponding to the number of adsorbed colloid layers on the wall. They have managed to observe finite contact angle when moving further from the critical point, even though the contact angle values are usually small in this partial wetting regime. However, as expected, they have found that the

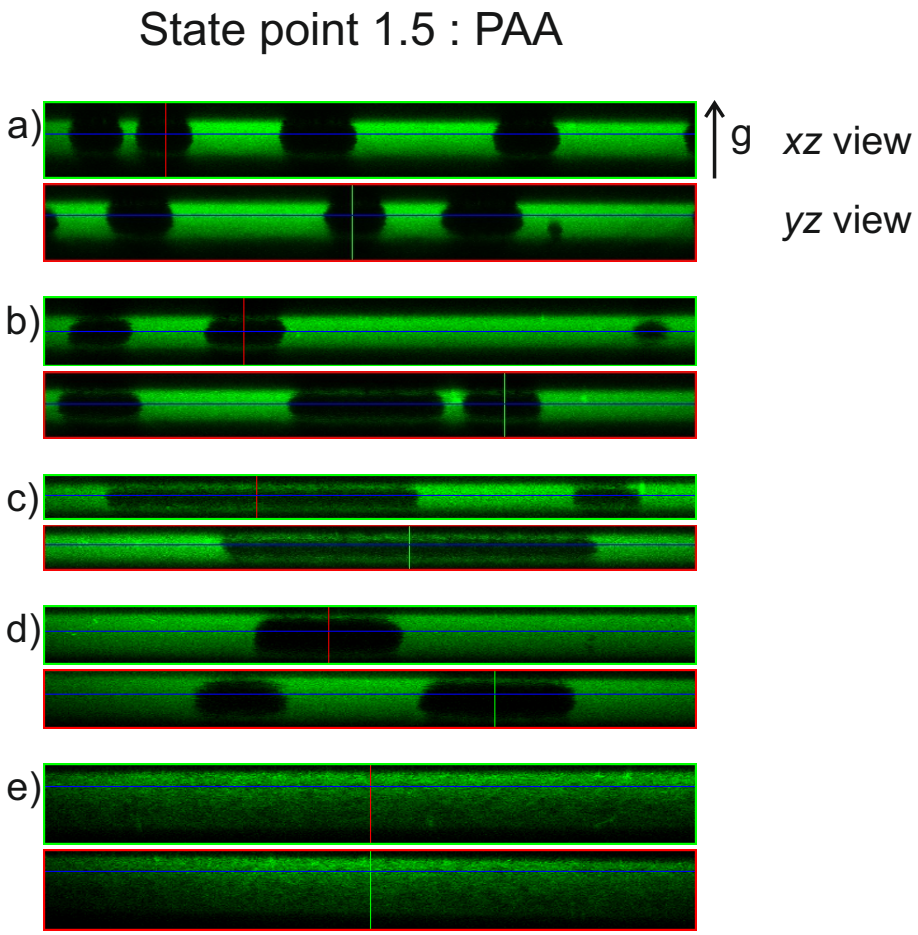


Figure 5.5: The z-stack view (xz and yz views on top of each other) of wetting transition for PAA-coated wall (note that the coated wall is positioned as the top wall in all images, but serves as a base wall in the experiment, as indicated by the arrow pointing towards gravity) along the dilution line of state point 1.5 towards the critical point: (a) at state point 1.5a, (b) at state point 1.5b, (c) at state point 1.5c, (d) at state point 1.5d, and (e) at state point 1.5e. The cell is about 10 µm in thickness and measured vertically through the visible green region formed by the fluorescently labelled PMMA colloidal particles. The width of each image is 200 µm. The red, blue and green lines are the positional marker from the confocal microscope software.

wall is completely wet by the colloidal liquid close to the bulk critical point when the density difference of the coexisting liquid and gas is small, which is approaching the one-phase region. They have also looked into the surface phase behaviour and identified the layering lines off bulk coexistence into the one-phase region [173].

Another theoretical study by Brader et. al [136] shows that at $q = 0.6$ and at a value of $\eta_p^r > 0.72$, the wall shows partial wetting by the colloidal liquid. They have found their wetting transition to be at η_p^r where the colloidal liquid starts to exhibit complete wetting with the formation of a liquid layer on the wall. At values of $0.62 < \eta_p^r < 0.72$, they have shown the first, second and third layering transitions with Γ that jumps discontinuously. This is a character of a first order wetting transition, even though the prewetting line is difficult to be determined. The absence of this tangential line from the coexistence curve at the wetting transition leads them to conclude the formation of extremely short prewetting line of the system [136].

This complete wetting regime can also be observed at state points 1.5c and 1.5d in our system. It is conspicuous that a liquid layer is formed on the coated wall, implying the complete wetting that happens below the T_w region. This sample reaches the one-phase region at state point 1.5e where we are not able to see any liquid-gas phase difference anymore, and hence no wall preference can be observed.

Similar observations can be seen at state point 2 (Fig. 5.6). At state point 2a, the sample displays partial wetting in the vicinity of the polymer-coated wall. With the first dilution point at state point 2b, the sample starts to exhibit complete wetting on the solid substrate, that can also be observed with state points 2c and 2d. State point 2e marks the one-phase region of the sample mixture. Figure 5.7 shows state point 3 where similar partial wetting to complete wetting can be observed. At state point 3a, the sample shows a partial wetting regime with the substrate. However, it starts to exhibit complete wetting for state points 3b and 3c, although the exact transition is hard to pinpoint. This sample shows one-phase behaviour at state points 3d, 3e and 3f. These qualitative experimental observations show that our colloid-polymer system displays a wetting transition from partial wetting to complete wetting on a polymer-coated substrate as we move closer to the binodal line, or the critical point.

In addition to these observations, we have scanned through our colloid-polymer mixture at state point 5 to identify whether a wetting transition may also occur at a state point further up

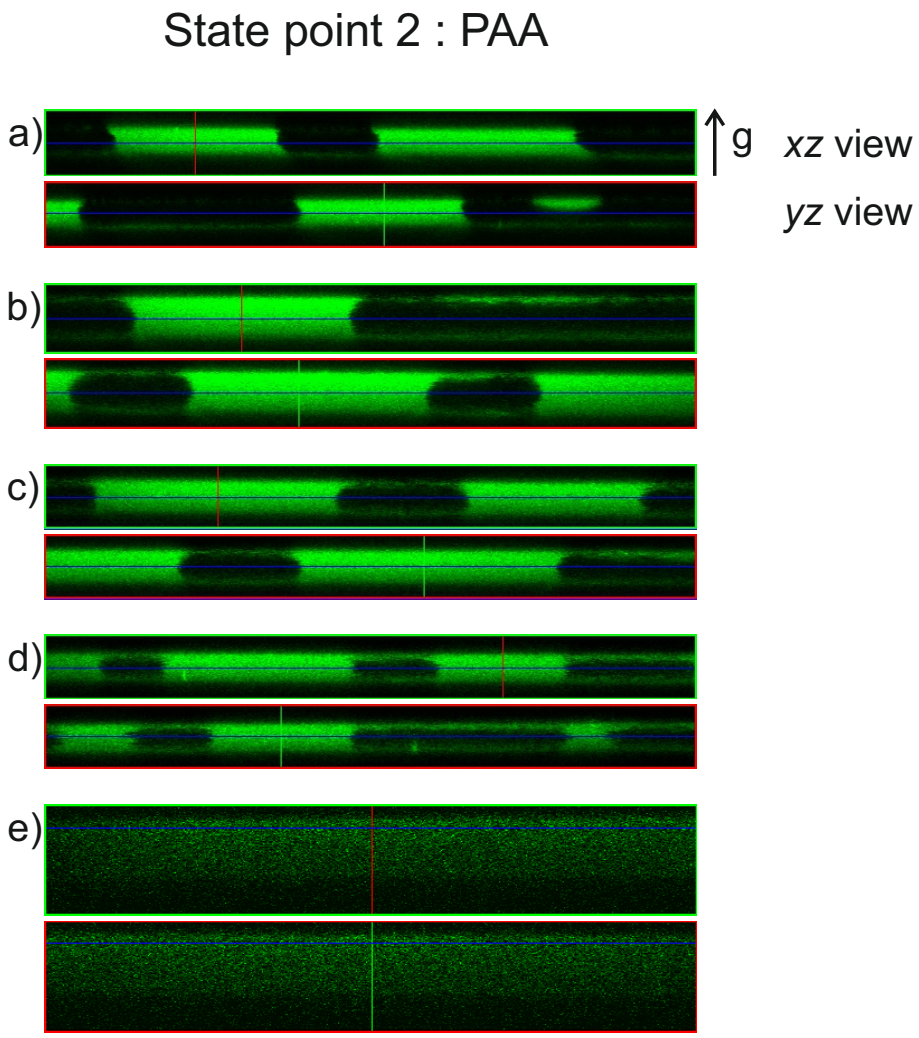


Figure 5.6: The z-stack view (xz and yz views on top of each other) of wetting transition for PAA-coated wall (note that the coated wall is positioned as the top wall in all images, but serves as a base wall in the experiment as indicated by the arrow pointing towards gravity) along the dilution line of state point 2 towards the critical point: (a) at state point 2a, (b) at state point 2b, (c) at state point 2c, (d) at state point 2d, and (e) at state point 2e. The cell is about 10 µm in thickness and measured vertically through the visible green region formed by the fluorescently labelled PMMA colloidal particles. The width of each image is 200 µm. The red, blue and green lines are the positional marker from the confocal microscope software.

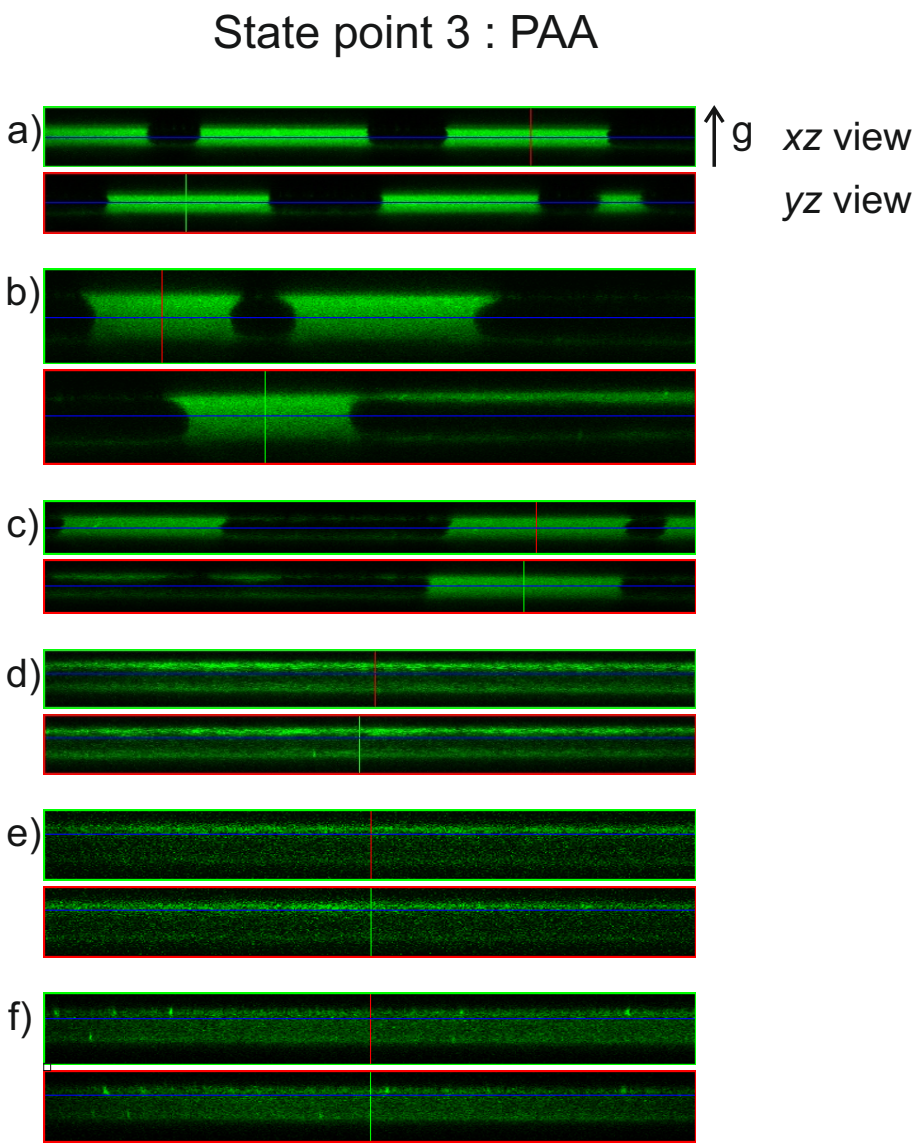


Figure 5.7: The z-stack view (xz and yz views on top of each other) of wetting transition for PAA-coated wall (note that the coated wall is positioned as the top wall in all images, but serves as a base wall in the experiment as indicated by the arrow pointing towards gravity) along the dilution line of state point 3 towards the critical point: (a) at state point 3a, (b) at state point 3b, (c) at state point 3c, (d) at state point 3d, and (e) at state point 3e. The cell is about 10 µm in thickness and measured vertically through the visible green region formed by the fluorescently labelled PMMA colloidal particles. The width of each image is 200 µm. The red, blue and green lines are the positional marker from the confocal microscope software.

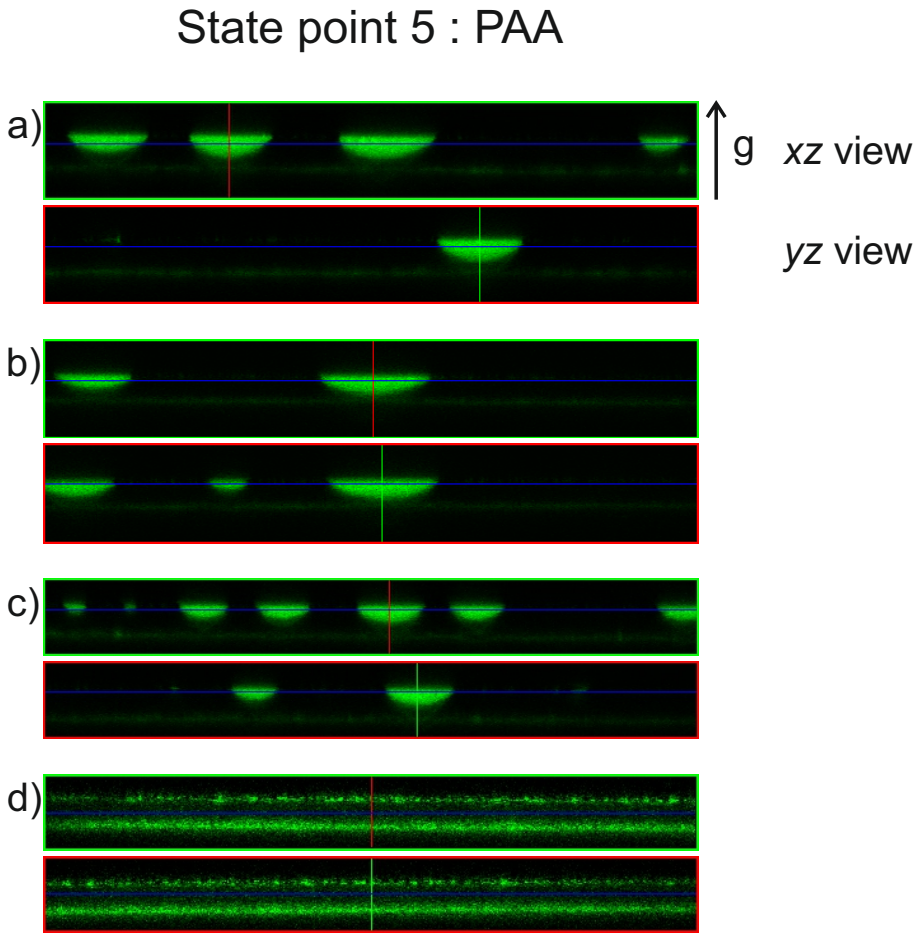


Figure 5.8: The z-stack view (xz and yz views on top of each other) of wetting transition for PAA-coated wall (note that the coated wall is positioned as the top wall in all images, but serves as a base wall in the experiment as indicated by the arrow pointing towards gravity) along the dilution line of state point 5 towards the critical point: (a) at state point 5a, (b) at state point 5b, (c) at state point 5c, and (d) at state point 5d. The cell is about 10 µm in thickness and measured vertically from the base of the visible green droplet to a very thin green layer on the top wall formed by the fluorescently labelled PMMA colloidal particles. The width of each image is 200 µm. The red, blue and green lines are the positional marker from the confocal microscope software.

on the phase diagram. However, this state point does not show any sign of wetting transition where we can expect to see a complete wetting as we get closer to the binodal line. In fact, Figure 5.8 shows that for all the two-phase regions of 5a, 5b and 5c, partial wetting is observed. This dilution line starts to reach the one-phase region at state point 5d. The additional observations with state point 5 allow us to draw the estimated wetting transition line in the phase diagram as indicated by the straight blue line (refer to the phase diagram). All the state points above the line behave as partial wetting, and the region between the line and the binodal line consists of state points that display complete wetting.

5.4 Conclusion

In sum, these qualitative experimental observations have shown that Cahn's wetting transition can be clearly observed using our colloid-polymer mixtures. Near the vicinity of the PAA-coated wall, we could see partial wetting of the substrate further from the binodal line, but as we move closer to the critical point, the colloidal liquid phase starts to spread on the substrate, forming complete wetting with zero contact angle.

On the other hand, we have seen a clear partial wetting of the colloid-polymer mixtures in the vicinity of the chitosan-coated walls. However, the coating appears less robust, and following the dilution lines, it is difficult to see the trend of wetting transitions.

Acknowledgements

We thank Dr. Lia Verhoeff and Rachel Knight, a Part II student in the Aarts group, for performing with related experiments.

Chapter 6

Wetting of Colloid-Polymer Mixtures at Curved Surfaces

ABSTRACT

In this chapter, we study the interface of our polymethyl(methacrylate) (PMMA) colloids and xanthan polymer mixtures in the vicinity of spherical silica micro beads. The silica beads are coated with polyacrylamide (PAA), alongside a batch of clean silica beads as a control. Upon modification, the silica beads are added into two different state points of our colloid-polymer mixtures. These mixtures are sandwiched between two glass walls, with the bottom wall a PAA-modified wall. We optically observe the wetting behaviour of the colloidal liquid phase with the silica spheres by utilising laser scanning confocal microscope (LSCM). The three-phase contact line and the deformation of the interface that can be determined are subsequently analysed with Mathematica. We compare the theoretical plots generated from mechanical equilibrium with the experiments.

6.1 Binary liquids behaviour towards spherical particles

The common saying that there is no use to cry over spilled milk might have been different if the milk in the container can remain still even if the receptacle is tilted horizontally. However, from common experience, we know that the milk spills out and empties the wide container if tilted horizontally. Contrary, the liquid behaves differently in a narrow container, like in a drinking straw, in which it remains even if it is lied flat [174]. This behaviour is attributable to the nature of the liquid that always favour the minimising of the free energy by adjusting itself to the shape of the container. The minimisation of the free energy is related to the three energy terms, namely the surface tension of the liquid-gas interface, the contact angle and the capillary length, which are all dependent on the shape l of the meniscus. The meniscus, or the extra area of the drop that is in contact with the container wall, can be measured by the Young-Laplace equation for l, and must be solved from the contact angle, θ, formed. This can be used to identify the wetting preference of the liquid towards the solid surface, and whether a liquid spills or remains [2, 174].

Interestingly, the choice of the liquid to remain inside a very small size of a capillary is not always the case. As calculated by Rascón et. al [174], liquids empty capillaries of noncircular cross-sections no matter how small they are, and this depends on the contact angle made by the liquid with the solid wall. This shows the crucial role of curvature on the wetting behaviour of a system. We can exploit this understanding in the recent advancement of microfluidic devices by constructing geometrical structures with various shapes and lengthscales of interest [174, 175]. Not only with a simple liquid, we can also design microfluidic devices that can be manipulated to study the phase behaviour of binary fluids that show rich wetting behaviour towards changes in the meniscus shape in response to small physical or chemical changes of the capillaries [2, 5, 174]. Inspired by these recent predictions, here we study the behaviour of a meniscus near a curved surface.

One straightforward way to observe the behaviour of a fluid at a curved surface is by preparing a mixture of a fluid with spherical or nonspherical hard particles. Due to the geometrical simplicity offered by a sphere, spherical particles in a simple or binary liquid can be a suitable model system in studying the phenomena [175]. Similar to a meniscus formed by a liquid at a vertical orientation of a planar wall, an interface of a phase separating binary mixture is also able to deform itself to show wetting preference at the vicinity of a spherical hard particle.

Take for example a system containing spherical silica particles dispersed in a colloid-polymer mixture. Colloid-polymer mixtures can phase separate into colloid-rich phase and polymer-rich phase, and form an interface that exhibits very low interfacial tensions. With spherical particles dispersed in the mixture, we can expect that large and dense particles will sink to the bottom. However, for a particle to be held at the fluid interface to satisfy the equilibrium, the system will do some adjustments by minimising the free energy of the system or equivalently setting the net force to zero [176]. The force balance between the gravity and the surface force acting on the particle determines whether the particle will be held at the interface or sink to the bottom. If the surface force is stronger than the gravitational force acting on the particle, the force is capable of holding the particle at the interface [176].

Spherical particles that are held at the liquid-liquid or liquid-gas interface act as freely moving particles, and their positions at the interface is influenced by the wetting at the curved surfaces. For particles with homogeneous surfaces, the wettability is determined by the contact angle formed by the particles at the liquid-liquid interface based on their preference. If we take oil-water interface for instance, the wettability can be decided by the hydrophilicity or hydrophobicity of the particles towards the liquids by the contact angle formed. If the particles are hydrophilic, they are preferentially wet by water with a contact angle, θ, of less than 90°. On the other hand, hydrophobic particles are wet by water with $90° < \theta < 180°$. However, particles that are equally wet by both liquids as they have equal interfacial tensions with the liquids display a contact angle of 90° [176, 177].

Strong particle adhesion at the interface enables solid spherical particles to act as a stabiliser in an emulsion. This is known as Pickering emulsions, named after Pickering [178], who outlined that particles which are wet more by water than by oil and dwell at the oil-water interface in stability are able to act as emulsifiers for oil-in-water emulsions. As a rule of thumb, one of the liquids will wet the particles more than the other liquid, and hence the configuration will lead the less wet liquid to become the dispersed phase in the emulsion [179, 180]. For example, silica particles that are hydrophilic will stabilise oil-in-water emulsions and hydrophobic carbon black particles will stabilise water-in-oil emulsions [180, 181].

Similar to oil and water mixtures stabilised by particles of different hydrophobicity, modified silica particles are expected to give different wetting behaviour in colloid-polymer mixtures compared to their pristine counterpart. It will be interesting to observe the coated silica par-

ticles being wet by one of the colloidal phases. The surface force than is stronger than the gravitational force will keep the particles reside at the interface, and there may be chances of emulsions of colloidal liquid-gas to form. However, it is also interesting to see if the gravitational force is stronger than the surface force, such that the particles will settle to the bottom and deformation of the colloidal liquid-gas interface occurs. Perturbation of the colloidal liquid-gas interface with the silica particles causes the wetting phase (the liquid phase) to bend or curve around the spherical particle. This can be either rising or depressing, depending on the wettability. Similar to wetting on a planar surfaces, this action comes with an energy cost that has to be taken into consideration.

A simple estimate to decide whether the silica particles rest at the interface or sink follows from the following: the gravitational force equals $m^*g = \Delta\rho(\frac{4}{3})\pi R^3 g$ and should be balanced by the interfacial force which is proportional to $2\pi\gamma R$, such that a critical radius $R^* \sim \sqrt{\gamma/\Delta\rho g}$ can be found above which particles will not be trapped at the interface. For our system, R* $\sim$ 1 µm, with $\Delta\rho$ the density difference between the silica particle and the aqueous colloidal phase.

We outline this chapter as follows: we begin by introducing the theoretical background of a solid sphere resting on a planar substrate, and is partially wet by a liquid. From the condition of the mechanical equilibrium, we come up with the mean curvature of a cylindrically symmetric surface. We then manage to generate the interfacial profile upon considering the gravitational and interfacial contributions through the Bond number. Next, we lay out the experimental systems we use to obtain the data, from the sample slide preparation to the utilisation of the confocal microscope. These data is later qualitatively discussed from the confocal image observations, and the reconstructed 3D images of the coated silica particles allow us to compare the experimental results with the theoretical predictions.

6.2 Theoretical background

The theory was contributed by Adam Stones, a DPhil student in the Aarts and Dullens groups, at the Physical & Theoretical Chemistry Laboratory, University of Oxford.

To analyse a solid sphere resting on a solid substrate and partially wet by a liquid, consider this scenario where we have a solid sphere of radius R tangentially-attached to a planar substrate

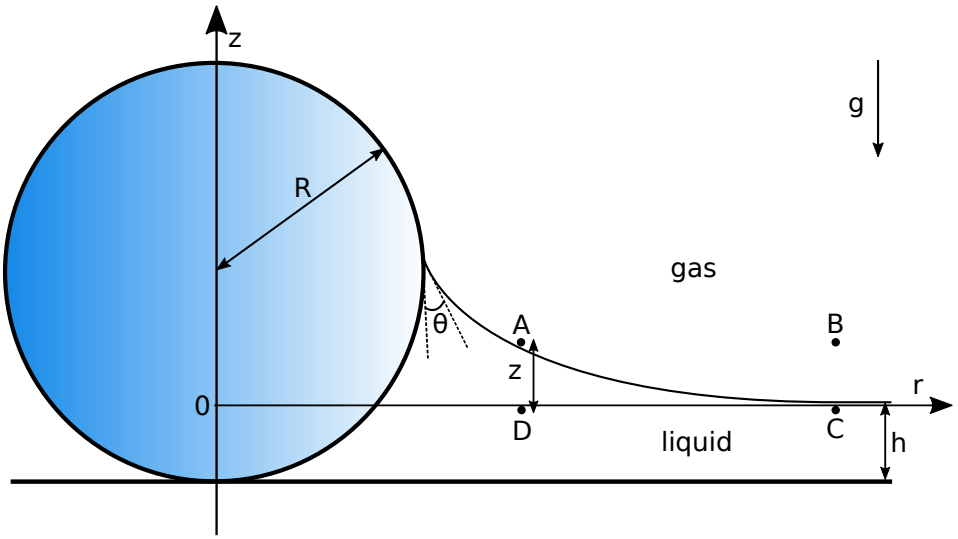


Figure 6.1: Schematic diagram of a spherical particle in contact with liquid-gas interface representing the interfacial profile.

as shown in Figure 6.1. The sphere is partially wet by a liquid layer which is at a height h from the planar substrate. The contact angle θ is measured from the tangent plane and the interface between the liquid and the gas above it.

The interfacial profile of this system can be worked out by first taking the vertical axis through the centre of the sphere, which is similar to a cylindrical symmetry scheme. We then come up with $z(r)$ where z is the vertical coordinate and r is the radial distance from this axis, which is measured relative to the interfacial height as $r \to \infty$.

From the perspective of mechanical equilibrium, points at the same height and in the same phase must have the same pressure. Therefore, by referring to Figure 6.1, this implies that:

$$P_A = P_B; \qquad P_D = P_C. \tag{6.1}$$

The pressure at point C then equals:

$$P_C = P_B + \rho_g g z, \tag{6.2}$$

with ρ_{g} the density of the gas, and g the gravity. As for point D, the related point A is just above the liquid-gas interface, and hence we have to consider adding the Laplace pressure term

due to the curved interface into the equation giving:

$$P_D = P_A + \rho_l g z - 2\gamma H, \tag{6.3}$$

with ρ_l the liquid density, γ the interfacial tension, and H the mean curvature. The mean curvature of a cylindrically symmetric surfaces is given by:

$$2H = \frac{z''}{(1+(z')^2)^{\frac{3}{2}}} + \frac{z'}{r(1+(z')^2)^{\frac{1}{2}}}, \tag{6.4}$$

where z' and z'' are the first and second derivatives of z with respect to r.

By subtracting Equation 6.2 from Equation 6.3, and substituting Equation 6.4 for H, we obtain:

$$\Delta\rho g z = \gamma \left(\frac{z''}{(1+(z')^2)^{\frac{3}{2}}} + \frac{z'}{r(1+(z')^2)^{\frac{1}{2}}} \right), \tag{6.5}$$

where $\Delta\rho = \rho_l - \rho_g$. By scaling all lengths by R, we can re-write this equation in terms of dimensionless variables that gives:

$$\left(\frac{R}{L_c}\right)^2 z = \frac{z''}{(1+(z')^2)^{\frac{3}{2}}} + \frac{z'}{r(1+(z')^2)^{\frac{1}{2}}}, \tag{6.6}$$

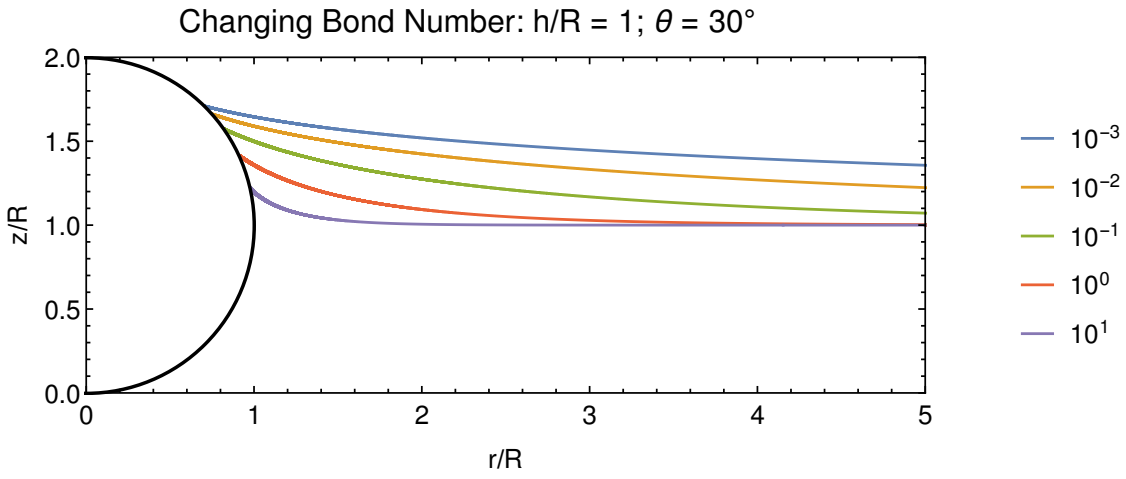
where $(R/L_c)^2$ is equal to the Bond number Bo which quantifies the relative importance of gravitational and interfacial forces, which can be written as:

$$Bo = \frac{\Delta\rho g R^2}{\gamma} = \left(\frac{R}{L_c}\right)^2. \tag{6.7}$$

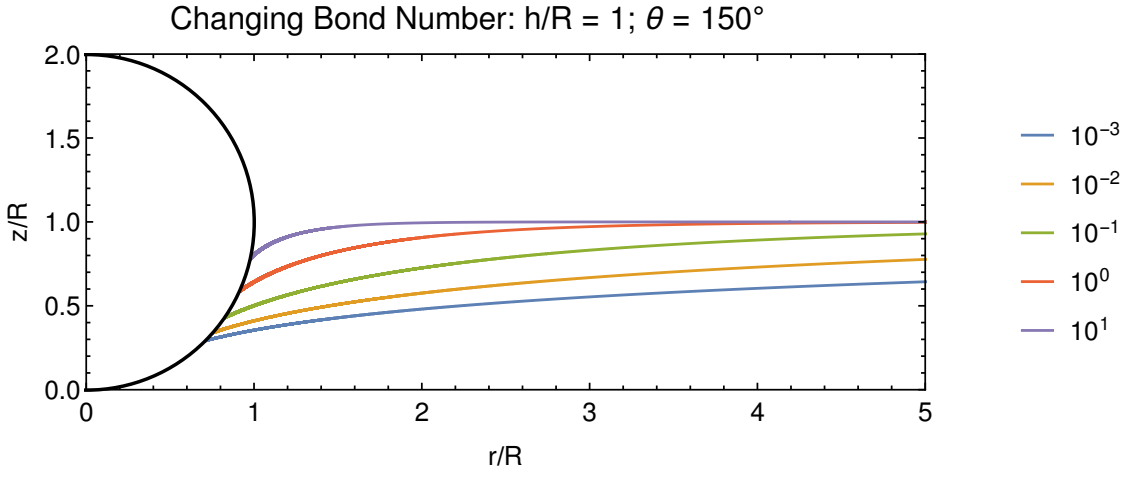
Here, the capillary length $L_c = \sqrt{\gamma/\Delta\rho g}$.

Solving Equation 6.6 for $z(r)$, we can find the interfacial profile for the boundary conditions of $z = 0$ for large r and z' at the contact radius given by the contact angle. Note that implementation of the contact boundary condition must be done with care, since the direction of the normal surface changes with the contact point.

The solution of Equation 6.6 allows us to understand the variation in the interfacial profile in terms of the changes in the Bond number Bo, the liquid height h, and the contact angle



(a)



(b)

Figure 6.2: Theoretical plots of the interfacial profile depending on the Bond number, with fixed contact angle and liquid height. Two possibilities of contact angle value are considered with (a) 30° and (b) 150°.

θ. Figure 6.2 illustrates an example of the interfacial profile of changing the Bond number. Increasing Bond number corresponds with a decrease in the capillary length.

6.3 Experimental systems

We have chosen two different state points of our colloid-polymer mixtures to study the liquid-gas interface in the vicinity of the spherical silica particles coated with polyacrylamide (PAA) as well as at uncoated silica particles. To observe this, we have prepared the colloid-polymer mixtures of fluorescently labelled poly(methylmethacrylate) (PMMA) colloidal particles of radius R_c =

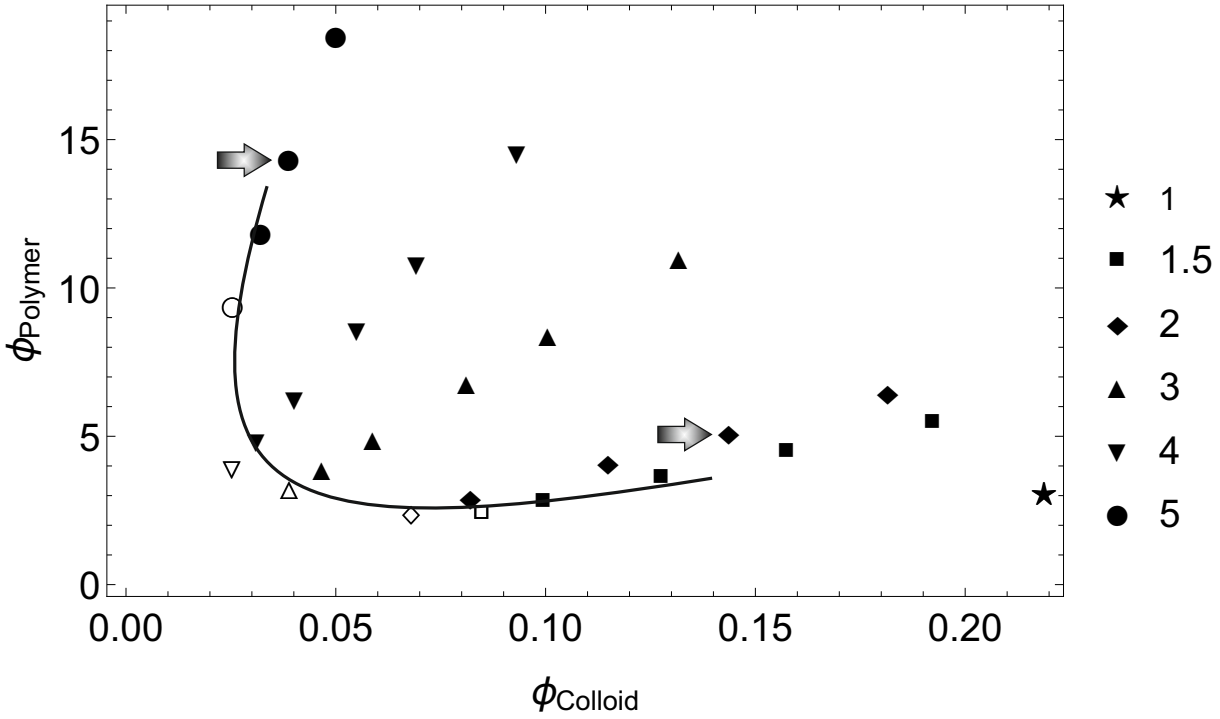


Figure 6.3: Phase diagram of PMMA-xanthan-water system. The filled symbols are the points of the two-phase region, and the open symbols are the points where the samples are not phase separating. The thick black line represents the approximate position of the binodal. State points 2b and 5b are pointed out by the arrows.

110 nm and non-adsorbing xanthan polymers of radius of gyration $R_g = 264$ nm at state points 2b and 5b, as pointed out in the phase diagram in Figure 6.3.

Spherical silica particles of 5 µm in diameter were purchased from JGC Catalysts & Chemicals Ltd. These commercial silica micro beads appear as a fine white powder and have a particle size distribution between 2−15 µm. These silica particles undergo surface modification with polyacrylamide, with the method outlined in Chapter 2. We have also prepared a batch of clean micro beads as a control, in which they undergo repeated washing and rinsing as for the coated particles prior to addition into the colloid-polymer mixtures.

The colloid-polymer mixtures containing coated and uncoated silica beads were then sandwiched between two glass walls, with the bottom wall a PAA-coated glass. Due to the large range of particle size distribution, the larger silica beads act as a spacer for the confinement. Hence, from the inverted and upright laser scanning confocal microscope (LSCM) used to observe the wetting behaviour optically, the height of the confinement was found to be between 20−40 µm.

The theoretical analysis of the particles in the colloid-polymer mixture at state point 5b was done based on the data we obtained from Chapters 2 and 4 of this thesis. The experimental plots were generated by taking the capillary length, L_c, as 12 µm and the contact angle, θ, as 60°. The size of the particles were measured from the reconstructed confocal images using Mathematica.

6.4 Results and discussion

In order to study the interfacial behaviour of our colloid-polymer mixtures towards spherical silica particles, we have prepared two mixtures of different state points, 2b and 5b. As shown in the phase diagram (Fig. 6.3), state point 2b has a higher colloidal liquid phase compared to its counterpart, state point 5b. Hence, we can expect the colloidal liquid-gas interface of state point 2b to be at a higher level than most of the silica or glass micro beads. In other word, small silica beads are immersed in the colloidal liquid phase and completely wet by the phase regardless of the coating as this costs less energy. One experimental remark that can be made here is that all the silica beads sediment to the bottom wall and due to the large size range of the 5 µm silica beads, some of the large beads act as a spacer in the sample confinement. In virtue of this, the gravity plays a role in the system, and thus, in some of the cases, the colloidal liquid phase settles to the bottom wall and completely wets the wall despite the bottom wall a PAA-coated wall. This is more pronounce in the mixtures of higher colloidal liquid phase content which is at state point 2b. However, in cases of sample 5b, PAA-coated bottom wall can be seen partially wet by the liquid phase. All of this behaviour of the samples between the parallel walls are optically observed by both types of confocal microscope, the inverted and upright mode. The inverted confocal microscope gives us a clear view from the bottom wall. However, we lack the information on the top view, where the top part of the particles appear black in the images. We thus utilise the upright confocal microscope as an alternative to get a better understanding of the colloidal liquid interaction with the silica spheres from the top view.

Figure 6.4 shows some examples of LSCM z-stack images of PAA-coated and uncoated silica beads dispersed in colloid-polymer mixtures at state points 2b and 5b, with the bottom wall of the confinement a PAA-coated wall. These images were observed with the upright confocal microscope, and due to the thickness of the sample slide, the intensity of the colloidal liquid

phase on the top and bottom walls has to be compromised. In Figure 6.4(a), we can see the PAA-coated silica beads dispersed in the sample of state point 2b, with quite a range of particle sizes. Due to the higher colloidal liquid phase in this sample, small size silica particles are fully immersed in the liquid phase despite being coated with a polymer layer as this costs less energy than bending the colloidal liquid-gas interface in favour of the silica beads coating. The expected contact angle depression of the colloidal liquid phase in the vicinity of the beads is also difficult to conclude with the naked eye. On the other hand, Figure 6.4(b) shows clean uncoated silica beads dispersed in sample 2b that act as a control. The formation of the rising meniscus by the colloidal liquid phase can be seen in the vicinity of the silica beads that surpass the height of the colloidal liquid-gas interface. This shows that the static beads distort the colloidal liquid and colloidal gas interface to form the right wetting contact angle. It is also good to note that the smaller size of the uncoated silica beads are readily submerged in the colloidal liquid phase as complete wetting is favourably achieved at no energy cost.

State point 5b has a lower content of the colloidal liquid phase, and hence we can see in Figures 6.4(c) and 6.4(d), islands of the phase in the images, with the colloidal gas phase dominating. It is also obvious that the silica beads, either coated or non-coated, prefer to be in the colloidal liquid phase region, with some of the beads dwell at the colloidal liquid-gas interface. The preference of the silica beads to rest in the colloidal liquid phase or be in the more wettable phase is the action to reduce the solid-liquid interfacial energy [182]. Tanaka et. al [182] have shown the pattern evolution of oligomers of styrene (OS) and ϵ-caprolactone (OCL) binary liquid mixtures containing glass particles that was caused by the dynamic interplay between phase separation and wetting. The glass beads are engulfed by the more wettable phase (OCL-rich phase) after phase separation of the binary mixtures and forming droplets that are eventually bridged by the wetting layer to form the interconnected structure. This is attributable to the strong attractive interaction between the interfacial energy between the two phases [182]. The work by Tanaka et. al [182] is similar to our sample of uncoated silica beads dispersed in a colloid-polymer mixture at state point 5b where the particles can be observed being distributed in the colloidal liquid phase (Fig. 6.4(d)). However, the PAA-coated silica beads in sample 5b display a more intriguing scenario in which the majority of the particles prefer to rest at the interface of the colloidal liquid and colloidal gas (Fig. 6.4(c)). We may assume that the affinity of the colloidal gas phase towards the coated beads to form a partial wetting situation triggers a competition between the colloidal liquid and colloidal gas phases to attract the beads, and thus

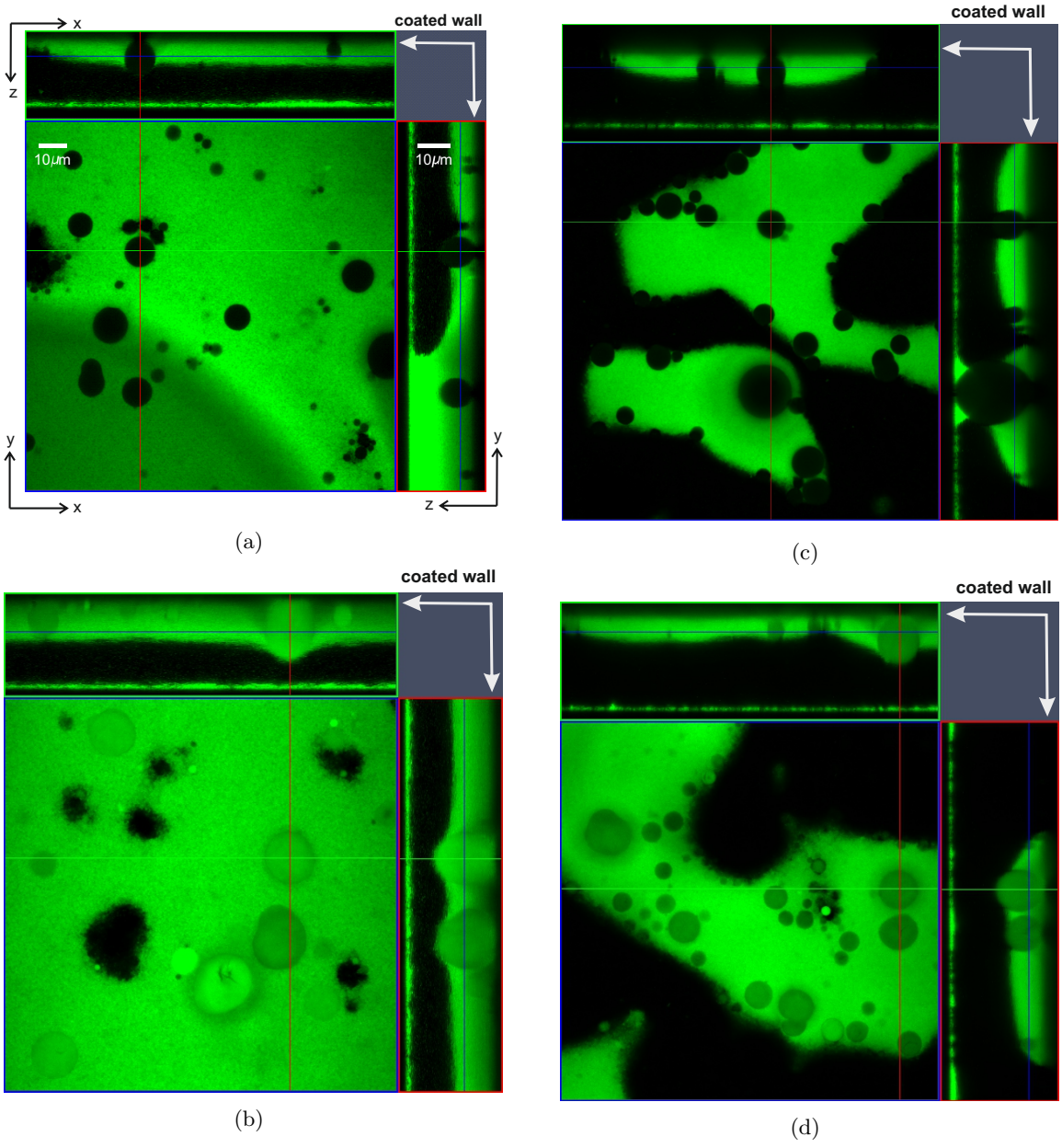


Figure 6.4: Upright LSCM z-stack images of silica beads in PMMA-xanthan colloid-polymer mixtures at state points 2b and 5b: (a) PAA-coated beads in sample 2b, (b) uncoated beads in sample 2b, (c) PAA-coated beads in sample 5b, and (d) uncoated beads in sample 5b. The xy axes show the layout of the xy plane of the sample slide, while the two adjacent fragments (labelled as the xz and yz axes) show the z-stack with respect to the xy plane, indicating the thickness of the sample slide. The coated wall that serves as the base wall is pointed out by the arrows. The axes and scale bar are also applicable to images (b), (c) and (d).

renders the beads to dwell at the interface. As a comparison to state point 5b, the case of the dwelling preference of our silica particles in the more wettable phase is not very significant in state point 2b as the higher content of the colloidal liquid phase enables the silica particles to be randomly distributed throughout the region of interest.

Having mentioned the preference of the silica particles in the samples, it is interesting to point out the small silica beads that also exist in the system. This is especially true for coated silica particles in the sample of state point 5b whereby the system tends to display partial wetting behaviour. Whether these spherical particles sit at the interface or sediment to the bottom wall depends on the force balance between gravity and the surface force [176]. In our case with the majority of the silica particles of roughly 5 µm in size, the gravitational force is larger than the surface force acting on the particles, and hence these particles sediment to the bottom wall as the surface force is not able to keep the particles floating at the interface. It is found that the gravitational force is 4.0×10^{-12} N whereas the surface force is 3.5×10^{-14} N in our system (see Section 6.1 for the estimation). In our case, even though there are some small particles of the size of ~ 1 µm that may be possible to be lifted up to be at the liquid-gas interface, it is difficult to find any single individual small particle from the confocal images. There are some small particles in clusters that may be considered to be at the interface, but this idea can be quite misleading as the small particle may be influenced by the capillary forces of its neighbouring particles.

In contrast to the aforementioned scenario, uncoated silica beads are not found to be at the colloidal liquid-gas interface (Fig. 6.4(b) and Fig. 6.4(d)). Even though we can argue from the perspective of the size of the silica beads in comparison to the gravitational and surface forces, we might need to consider the preference of the particles to be in the colloidal liquid phase. As the interfacial energy is lowered when the uncoated beads dwell in the colloidal liquid phase, hence it is more favourable for the colloidal liquid to enshroud the particles, and drag them down to settle to the bottom wall.

Another clear observation that we can make between the PAA-coated and uncoated silica particles under scrutiny is that the coated silica beads appear to be darker in colour as compared to their uncoated equivalent. It is thought that the PAA-coated beads that are partially wet by the colloidal liquid phase due to the depletion interaction have an increased interaction with the xanthan polymers. At the microscopic level, it is also possible for the xanthan polymer

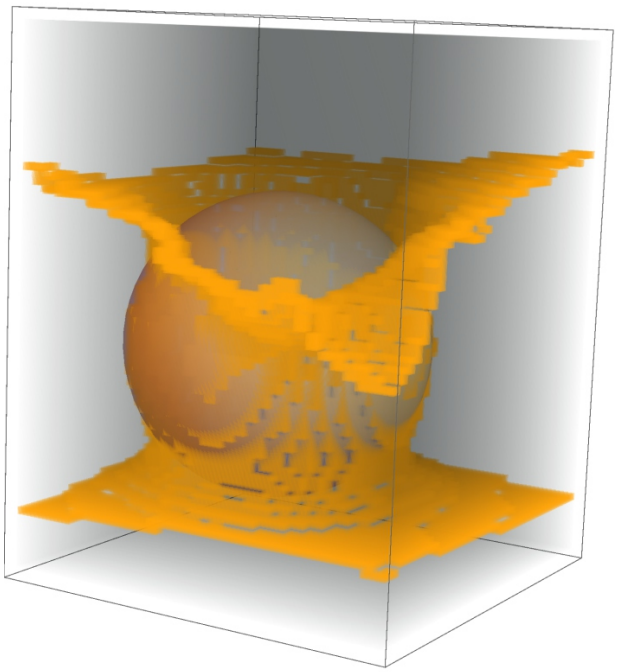
chains to be entangled with the PAA polymer chains that make up the thin layer coating on the silica beads. This remark is supported by the pristine silica beads that do not show this kind of interactions with the xanthan polymers by displaying the similar colour green.

To have a closer look at an individual particle, we have reconstructed the images we obtained from LSCM using Mathematica. Figure 6.5 shows 3D images of the position of two individual PAA-coated silica particles in the colloid-polymer mixture at state point 5b. In general, depending on the size and the position of the particles in the mixture, they can either be completely wet by the colloidal liquid phase or being partially wet by it. However, Figure 6.5 shows that coated particles at state point 5b display partial wetting behaviour. The behaviour of a meniscus near an even simpler curved interface, namely that of a cylinder, already shows intriguing behaviour, following Parry & Rascón [183]. Here, the situation is preferentially even more complex and rich, but any possible relation to wedge filling transitions fall outside the scope of the current work.

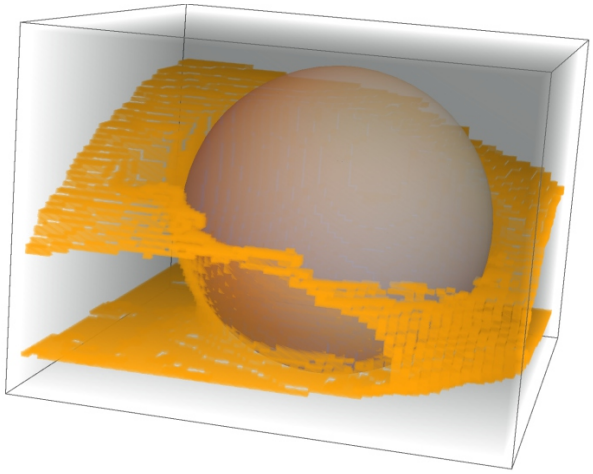
Next, we qualitatively compare the 3D experimental plots to the theoretically generated ones. We note that a direct quantitative comparison has not been attempted: the experimental configuration is not close enough to the idealised theoretical situation. However, from chapters 2 and 4, we use the experimental data: capillary length L_c equals 12 µm, and the contact angle $\theta \sim 60°$. For Sphere 1 (Fig. 6.5(a)) which has a radius $R = 2.3$ µm, this gives a $Bo = 0.04$. We note that $h/R > 2$. To verify that the theory predicts reasonable profiles, we generate theoretical lines for $Bo = 0.04$, $\theta = 60°$, and vary h/R around 2. Indeed, theory and experiment appear qualitatively similar. For Sphere 2 (Fig. 6.5(b)), $R = 4.0$ µm such that $Bo = 0.11$, and with $h/R \sim 1$, we again generate theoretical profiles. Here, we also find reasonable agreement, but we note that Sphere 2 sits at the edge of the interface, making it even less ideal in comparison with theory. Further work is needed to perform a quantitative analysis.

6.5 Conclusion

In summary, we have successfully coated silica beads with polyacrylamide and observed their behaviour in our colloid-polymer mixtures at state points 2b and 5b, alongside clean silica particles as a control. In general, both coated and clean particles show preference towards colloidal liquid phase in both colloid-polymer mixtures containing high and low colloidal liquid

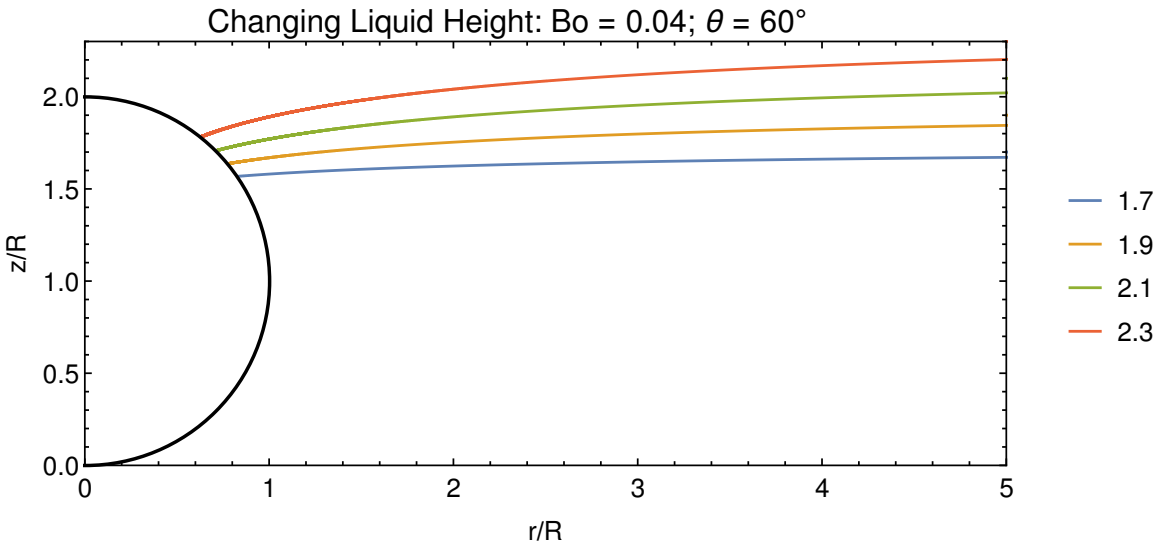


(a)

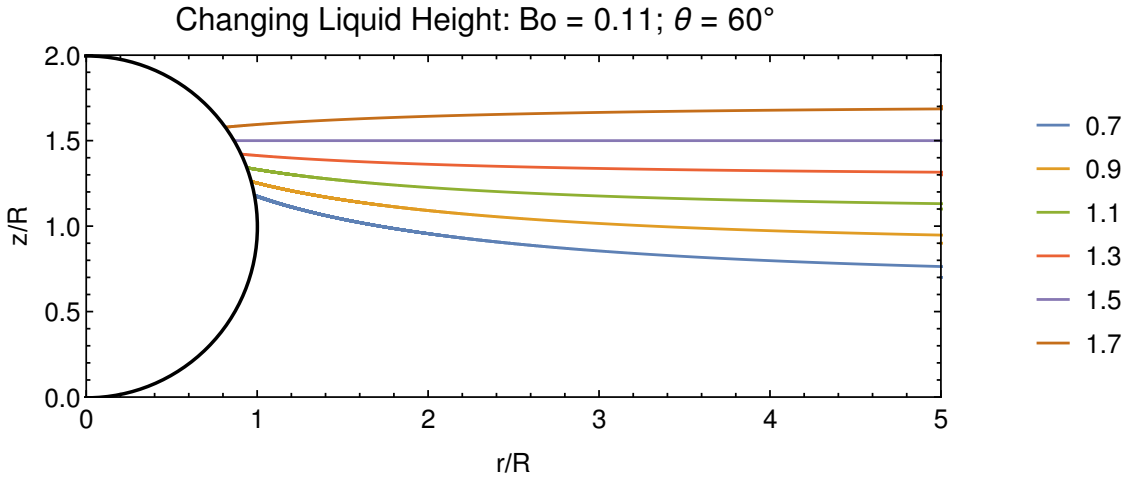


(b)

Figure 6.5: Reconstructed 3D images of PAA-coated silica bead's position in a PMMA-xanthan colloid-polymer mixture at state point 5b: (a) Sphere 1 and (b) Sphere 2.



(a)



(b)

Figure 6.6: Experimental plots of the interfacial profile depending on the liquid height, with fixed Bond number and contact angle. Two plots are made based on the particles observed in the experiment with different Bond numbers at (a) 0.04 and (b) 0.11.

content. Interesting observations can be made from the PAA-coated silica beads in the sample of state point 5b, where the particles can be visualised resting at the edge of the islands of colloidal liquid phase, implying the partial wetting. This partial wetting behaviour at a curved surface is in corroboration with the generated theoretical plots. These plots show that the colloid-polymer mixture still does not engulf the coated silica particle even if the colloidal liquid phase has reached a height above the particle.

Acknowledgements

We thank Adam Stones for the contribution of the theoretical part.

Summary

In this thesis, we studied the wetting behaviour of colloid-polymer mixtures in confinement. The fundamental objective is to observe partial wetting behaviour. This is made possible by using polymer-modified substrates and observe the mixtures by means of laser scanning confocal microscope. We began by giving a brief introduction about wetting phenomena in general and the colloidal lengthscales. We also mentioned the consequences of having a low interfacial tension (Chapter 1).

In Chapter 2, we introduced our colloid-polymer mixtures with the synthesis of the PMMA colloids that are fluorescently-labelled, as well as xanthan polymers that act as the depleting agent in the aqueous mixture. These mixtures phase-separate into colloid-rich, polymer-poor phase (colloidal liquid phase) in coexistence with the colloid-poor, polymer-rich phase (colloidal gas phase). They were then prepared in different series of concentrations to observe the phase separation to construct a phase diagram. To change the wetting behaviour of the mixtures, we have successfully performed chemical surface modification on glass substrates using two different polymers, polyacrylamide (PAA) and chitosan. The mixtures were sandwiched between two parallel glass slides of different wettability. Alongside that, we have also modified silica beads with PAA to study the wetting behaviour at curved surfaces. The length scales of the mesoscopic mixtures that is compatible with the real-space and real-time experiments in three dimensions allow us to scrutinise the mixtures by means of confocal microscopy. We also outlined the thermal capillary waves analysis that provides us with the physical properties of the system.

A review on polymer self-assembly and surface modification of the substrates, and possible interactions that might happen in our colloid-polymer system were presented in Chapter 3. We gave the background of PAA and chitosan polymers grafted on glass walls to form a thin monolayer. We also presented the physicochemical characterisations to measure the brush

thickness and the charge of the polymer coatings using ellipsometry, FTIR and zeta potential analysis. The colloid-polymer mixtures were used to physically probe the modified substrates in a single-wall or double-wall confinement where we could witness partial wetting of the mixtures, in contradiction to complete wetting exhibited by a clean glass wall. These qualitative results were obtained in the form of either colloidal liquid droplets or colloidal gas bubbles depending on the state point. We also demonstrated the phenomenon of capillary depression. The depletion interaction is the central theme of this whole entropy-driven system that causes the phase separation of the mixtures. The interaction between the colloidal particles and the modified substrate was changed due to the grafted polymer brush.

In Chapter 4, we performed contact angle measurements for the colloidal liquid droplets formed in the vicinity of PAA-coated and chitosan-coated walls. We have reconstructed the confocal images, prior to fitting to the theoretical model of the shape of a droplet. The theoretical framework is generated from the interplay between gravity and interfacial curvature based on Euler-Lagrange equation, with the contact angle fixed as a boundary condition. The fitting has quantitatively showed that both coatings are efficacious in demonstrating partial wetting, with PAA coating showing lower values of the contact angle. However, investigation on the relation between contact angle and time, or radius of the droplets does not show any clear trends for both parameters. We did not need to invoke the line tension in the system to analyse our droplets.

Chapter 5 showed that we were able to visualise the wetting transition using our colloid-polymer mixtures. We have scanned through four different series of mixtures in the vicinity of both PAA and chitosan coatings. As predicted, we could see partial wetting of the mixtures further from the binodal line, but displaying complete wetting closer to it. This enabled us to qualitatively estimate the wetting line in our phase diagram. The difficulty to measure the contact angle of the colloidal droplets as outlined in Chapter 4 has left the question about the order of the wetting transition open.

In Chapter 6, we took a step further in the geometry of our confinement by coating silica beads with PAA and dispersed the coated particles in our colloid-polymer mixtures at two different state points, alongside clean silica particles as a control. As expected, the clean silica beads are completely wet by the colloidal liquid particles. On the other hand, the PAA-coated particles show partial wetting. The particles also preferred to sit at the edge between the colloidal liquid and colloidal gas interface, which further implies partial wetting behaviour. This partial

wetting behaviour at a curved surface is in good agreement with the generated theoretical plots based on the condition of mechanical equilibrium.

This thesis shines light on wetting phenomena for systems where the interfacial roughness is comparable to the other relevant lengthscales of the systems. Furthermore, and in particular the last chapter, it may now become possible to study scaled up versions of, for example, Pickering emulsions, or the interaction between two particles trapped at an interface, where both the particles, their 3D positions and the thermal capillary waves can be observed in real time and space.

Appendix

A Wetting transition in the vicinity of PAA-coated walls

The wetting transition can be observed in our colloid-polymer mixtures for state points 1.5, 2 and 3, along their dilution lines, in the vicinity of a polyacrylamide (PAA)-coated wall (see Chapter 5). Figures A.1, A.2 and A.3 show the xy and z-stack views of LSCM images for samples at state point 1.5, 2 and 3, respectively. Note that the polyacrylamide-coated glass wall is positioned as a bottom wall for each observation, and pointed out by the arrows in the image. We can see that the PAA-coated wall is partially wet by the colloidal liquid phase at the first point of each mixture. However, as we move along the dilution line towards the binodal, the PAA-coated walls show complete wetting with the colloidal liquid phase. We have studied each sample until we reached the one-phase region, where there was no more phase separation between the colloidal liquid and the colloidal gas. In addition to this, we have also observed state point 5 where the state point and its dilution line only displays partial wetting behaviour (Fig. A.4). The one-phase region can be visualised at state point 5d. From these observations, we can draw an estimated wetting transition line that separates between partial wetting and complete wetting regions.

B Wetting transition in the vicinity of chitosan-coated walls

Apart from the PAA-coated walls, we have studied our chitosan-coated walls in a similar fashion in an attempt to observe the wetting transition (supplementary to Chapter 5). Figures B.1 and B.3 display the xz and yz views of LSCM images placed on top of each other for colloid-polymer samples at state points 2 and 3. The xy and z-stack views of the state points are also shown in

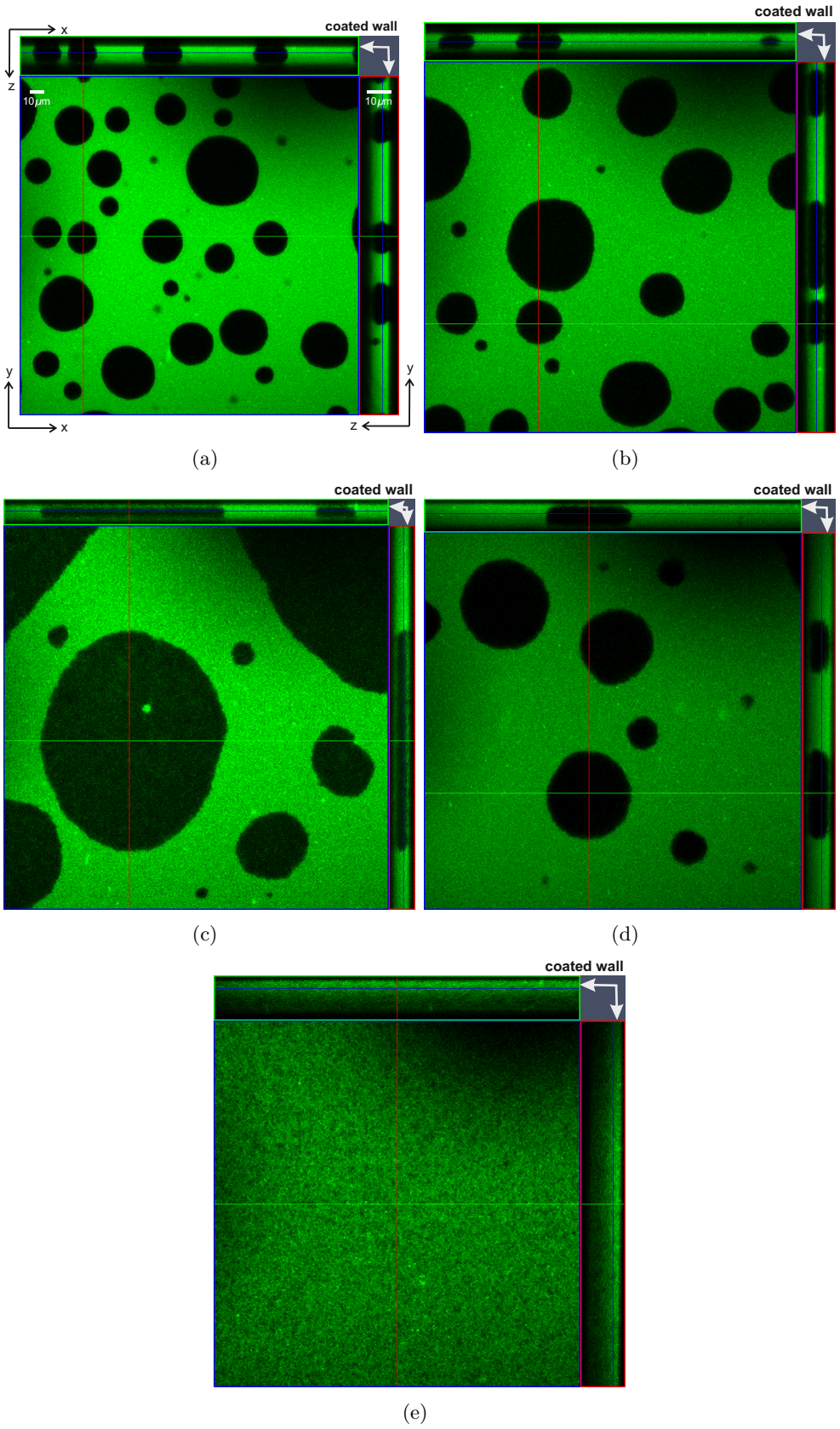


Figure A.1: Wetting transition for PAA-coated wall along the dilution line of state point 1.5 towards the critical point: (a) at state point 1.5a, (b) at state point 1.5b, (c) at state point 1.5c, (d) at state point 1.5d, and (e) at state point 1.5e. The arrows show the position of the PAA-coated wall which serves as the base wall. The axes and scale bars are also applicable to images (b), (c), (d) and (e).

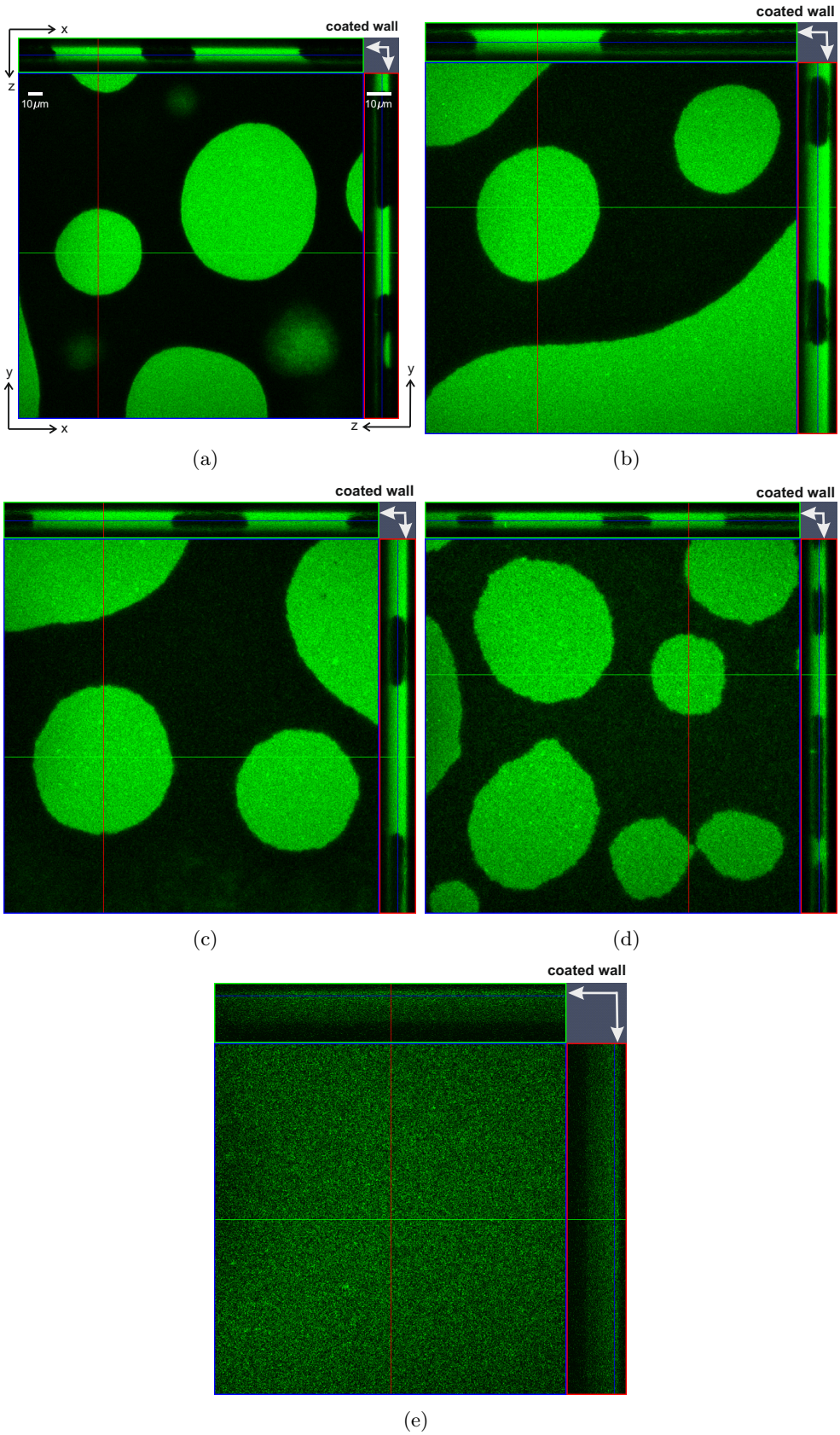


Figure A.2: Wetting transition for PAA-coated wall along the dilution line of state point 2 towards the critical point: (a) at state point 2a, (b) at state point 2b, (c) at state point 2c, (d) at state point 2d, and (e) at state point 2e. The arrows show the position of the PAA-coated wall which serves as the base wall. The axes and scale bars are also applicable to images (b), (c), (d) and (e).

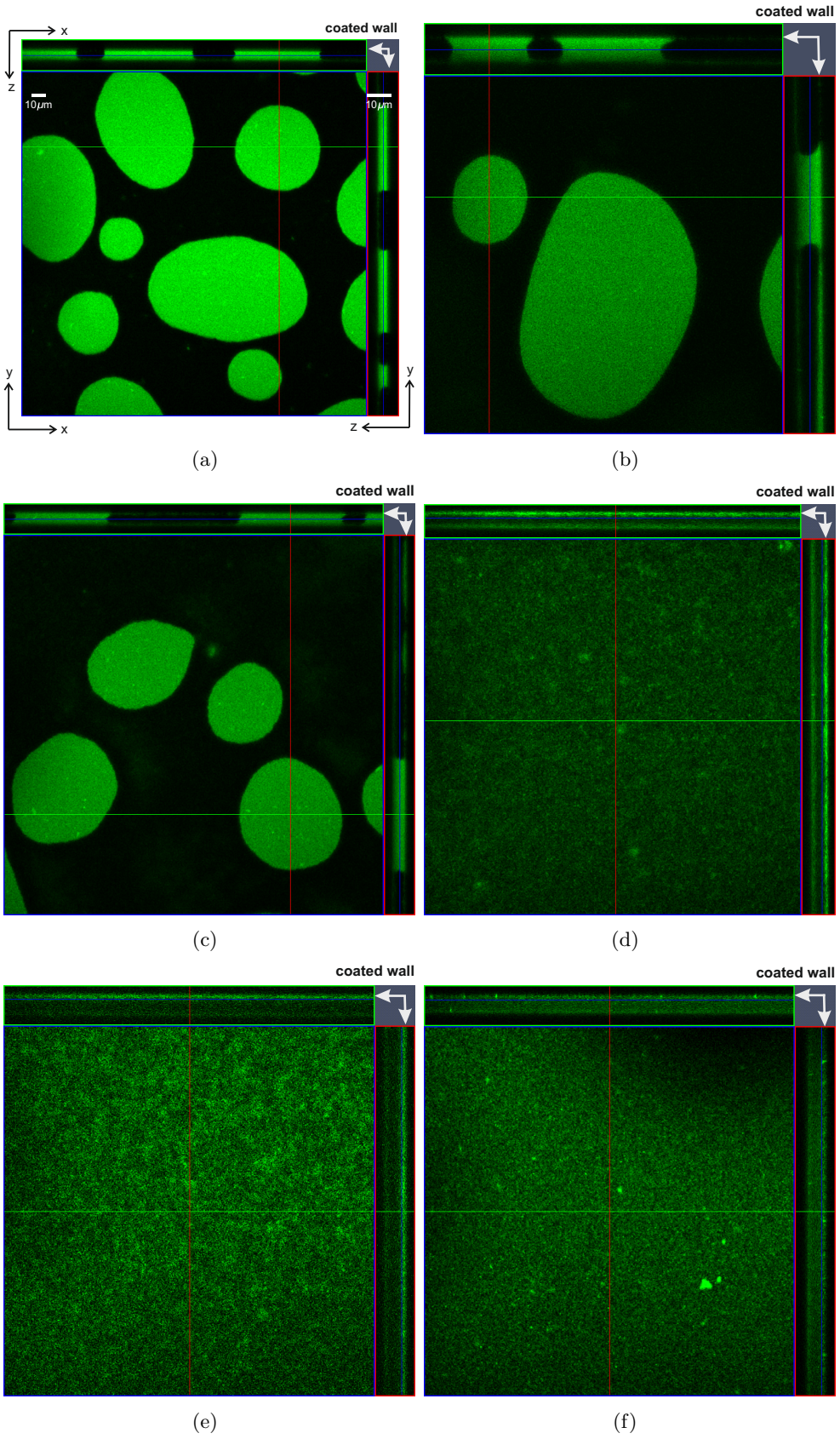
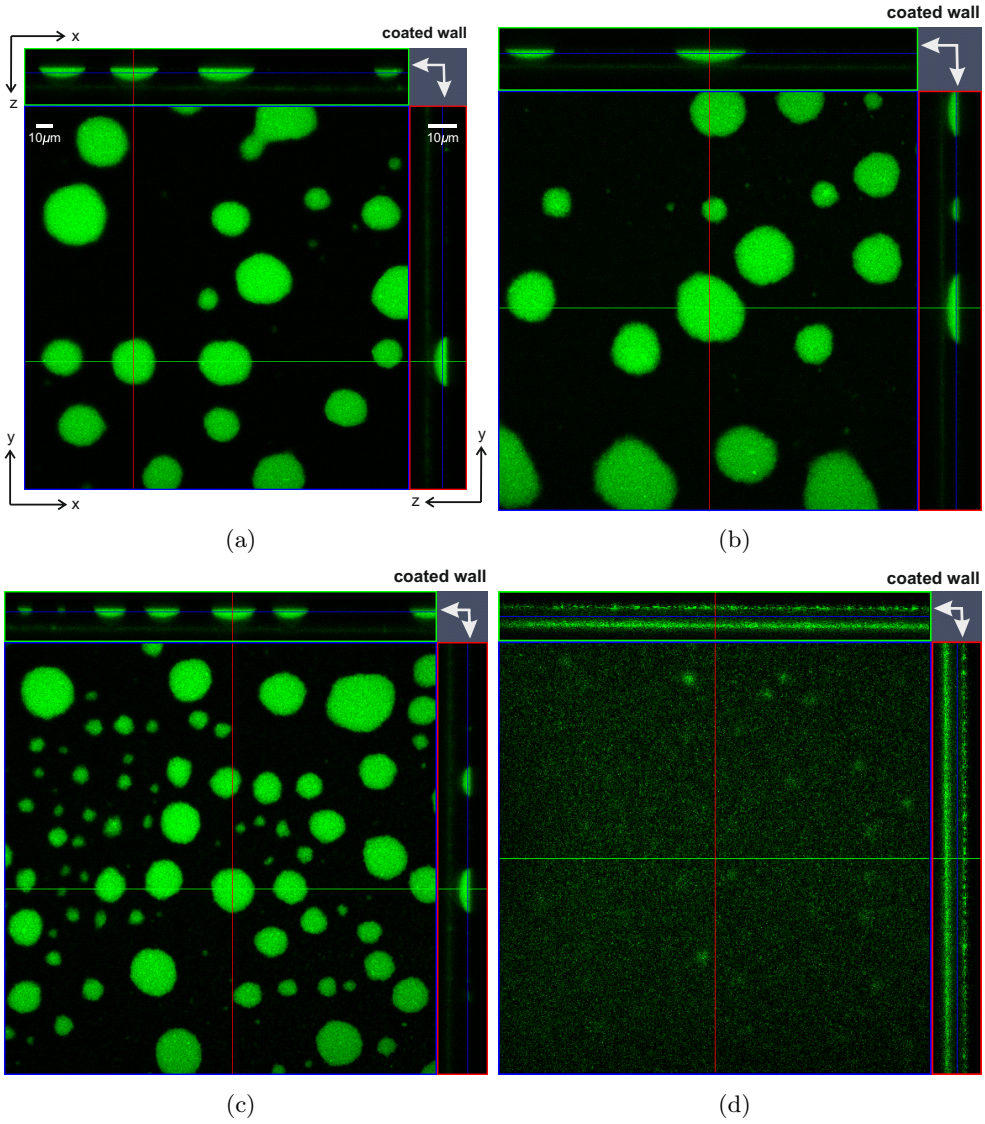


Figure A.3: Wetting transition for PAA-coated wall along the dilution line of state point 3 towards the critical point: (a) at state point 3a, (b) at state point 3b, (c) at state point 3c, (d) at state point 3d, (e) at state point 3e, and (f) at state point 3f. The arrows show the position of the PAA-coated wall which serves as the base wall. The axes and scale bars are also applicable to images (b), (c), (d), (e) and (f).



(a) (b)

(c) (d)

Figure A.4: Wetting transition for PAA-coated wall along the dilution line of state point 5 towards the critical point: (a) at state point 5a, (b) at state point 5b, (c) at state point 5c, and (d) at state point 5d. The arrows show the position of the PAA-coated wall which serves as the base wall. The axes and scale bars are also applicable to images (b), (c) and (d).

Figures B.2 and B.4.

Even though the chitosan-coated walls are capable of changing the wetting behaviour of the colloid-polymer mixtures from complete to partial wetting, it is quite difficult to see the trend of wetting transition from one state point and along its dilution line. At state point 2 for instance (Fig. B.1), the samples show partial wetting with the chitosan-coated walls for all the two-phase region (state point 2a, 2b and 2c), as opposed to PAA-coated walls that show partial wetting only at state point 2a with complete wetting observed at subsequent state points towards the binodal line.

On the other hand, observing state point 3 (Fig. B.3), the chitosan-coated walls show partial wetting at state point 3a, but it is not very discernible to conclude if state points 3b and 3c display partial or complete wetting. This shows that chitosan-coated walls can be a good model system in showing partial wetting for contact angle measurement, but are less robust in wetting transition observations.

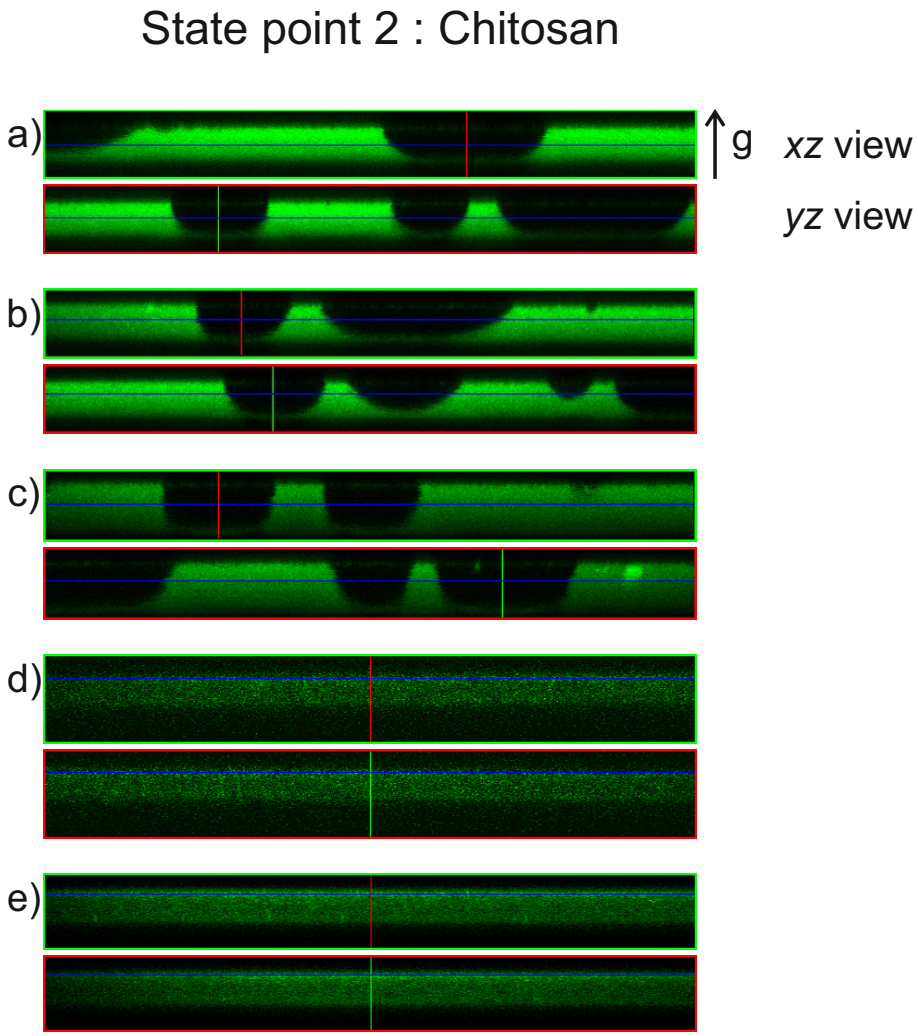


Figure B.1: The z-stack view (xz and yz views on top of each other) of wetting transition for chitosan-coated wall (note that the coated wall is positioned as the top wall in all images) along the dilution line of state point 2 towards the critical point: (a) at state point 2a, (b) at state point 2b, (c) at state point 2c, (d) at state point 2d, and (e) at state point 2e. The cell is about 10 µm in thickness and measured vertically through the visible green region formed by the fluorescently labelled PMMA colloidal particles. The width of each image is 200 µm. The red, blue and green lines are the positional marker from the confocal microscope software.

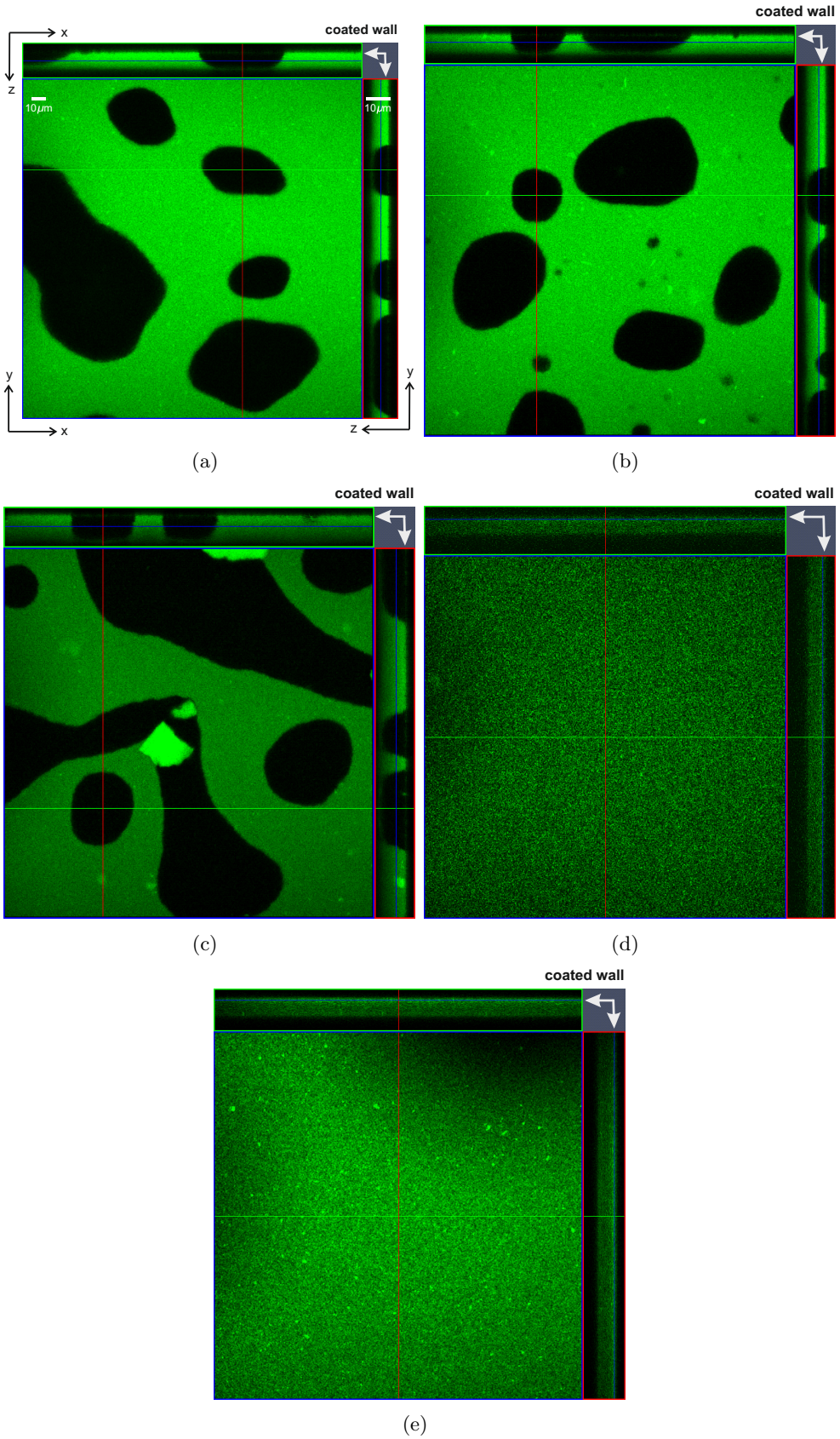


Figure B.2: Wetting transition for chitosan-coated wall along the dilution line of state point 2 towards the critical point: (a) at state point 2a, (b) at state point 2b, (c) at state point 2c, (d) at state point 2d, and (e) at state point 2e. The arrows show the position of the chitosan-coated wall which serves as the base wall. The axes and scale bars are also applicable to images (b), (c), (d) and (e).

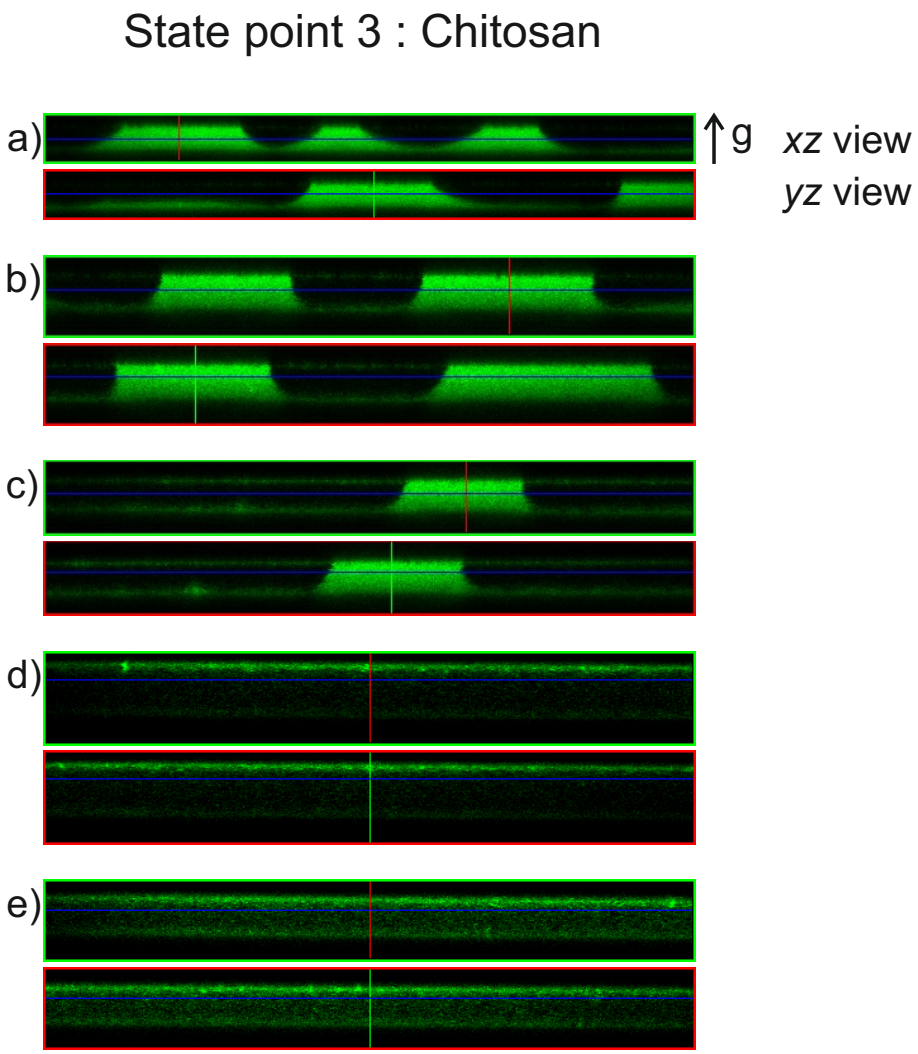


Figure B.3: The z-stack view (xz and yz views on top of each other) of wetting transition for chitosan-coated wall (note that the coated wall is positioned as the top wall in all images) along the dilution line of state point 3 towards the critical point: (a) at state point 3a, (b) at state point 3b, (c) at state point 3c, (d) at state point 3d, and (e) at state point 3e. The cell is about 10 µm in thickness and measured vertically through the visible green region formed by the fluorescently labelled PMMA colloidal particles. The width of each image is 200 µm. The red, blue and green lines are the positional marker from the confocal microscope software.

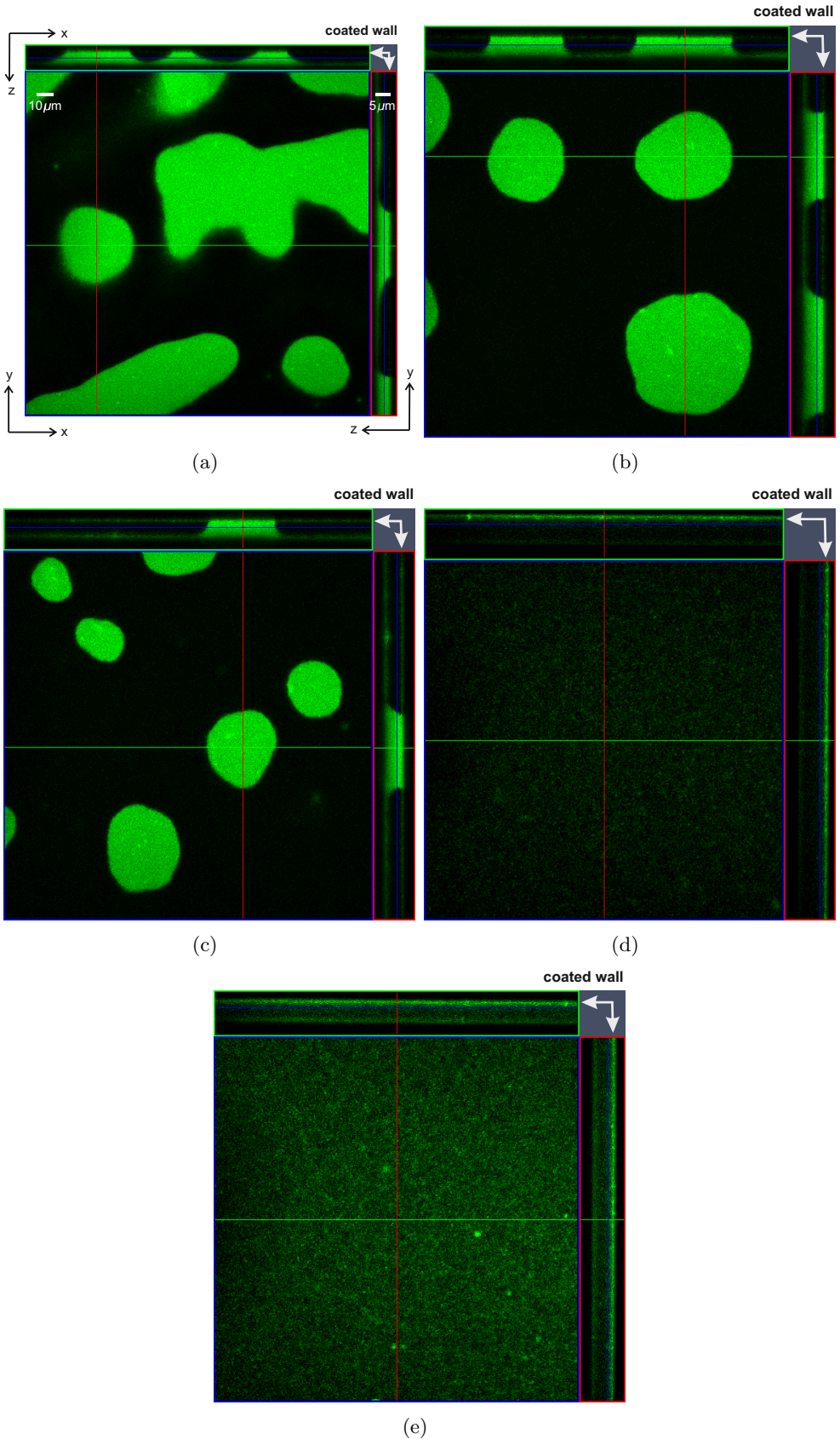


Figure B.4: Wetting transition for chitosan-coated wall along the dilution line of state point 3 towards the critical point: (a) at state point 3a, (b) at state point 3b, (c) at state point 3c, (d) at state point 3d, and (e) at state point 3e. The arrows show the position of the chitosan-coated wall which serves as the base wall. The axes and scale bars are also applicable to images (b), (c), (d) and (e).

Bibliography

[1] P. G. de Gennes, F. Brochard-Wyart, and D. Quéré. *Capillarity and Wetting Phenomena: Drops, Bubbles, Pearls, Waves*. Springer Science & Business Media, New York, 2004.

[2] D. Bonn, J. Eggers, J. Indekeu, J. Meunier, and E. Rolley. Wetting and spreading. *Reviews of Modern Physics*, 81(2):739–805, 2009.

[3] E. Bertrand, D. Bonn, D. Broseta, H. Dobbs, J. O. Indekeu, J. Meunier, K. Ragil, and N. Shahidzadeh. Wetting of alkanes on water. *Journal of Petroleum Science and Engineering*, 33(1-3):217–222, 2002.

[4] V. Bergeron, D. Bonn, J. Y. Martin, and L. Vovelle. Controlling droplet deposition with polymer additives. *Nature*, 405(6788):772–5, 2000.

[5] P. Tabeling. *Introduction to Microfluidics*. Oxford University Press, Oxford, 2005.

[6] G. M. Whitesides. The origins and the future of microfluidics. *Nature*, 442(7101):368–373, 2006.

[7] N. Pamme. Continuous flow separations in microfluidic devices. *Lab on a Chip*, 7(12):1644–59, 2007.

[8] Y. Yoon, S. Kim, J. Lee, J. Choi, R.-K. Kim, S.-J. Lee, O. Sul, and S.-B. Lee. Clogging-free microfluidics for continuous size-based separation of microparticles. *Scientific Reports*, 6(1):26531, 2016.

[9] E. A. G. Jamie, R. P. A. Dullens, and D. G. A. L. Aarts. Fluid-fluid demixing of off-critical colloid-polymer systems confined between parallel plates. *Journal of Physics. Condensed Matter: An Institute of Physics Journal*, 24(28):284120, 2012.

[10] S.-Y. Teh, R. Lin, L.-H. Hung, and A. P. Lee. Droplet microfluidics. *Lab on a Chip*, 8(2):198, 2008.

[11] O. K. Castell, C. J. Allender, and D. A. Barrow. Liquid-liquid phase separation: Characterisation of a novel device capable of separating particle carrying multiphase flows. *Lab Chip*, 9(3):388–396, 2009.

[12] K. F. Jensen. Microreaction engineering - is small better?. *Chemical Engineering Science*, 56(2):293–303, 2001.

[13] W. A. Zisman. Relation of the equilibrium contact angle to liquid and solid constitution. *Contact Angle, Wettability, and Adhesion*, 43(43):1–51, 1964.

[14] P. G. de Gennes. Wetting: Statics and dynamics. *Reviews of Modern Physics*, 57(3):827–863, 1985.

[15] G. M. Whitesides and P. E. Laibinis. Wet chemical approaches to the characterization of organic surfaces: Self-assembled monolayers, wetting, and the physical-organic chemistry of the solid-liquid interface. *Langmuir*, 6(1):87–96, 1990.

[16] T. Young. An essay on the cohesion of fluids. *Philosophical Transactions of the Royal Society of London*, 95:65–87, 1805.

[17] D. J. Durian and C. Franck. Wetting phenomena of binary liquid mixtures on chemically altered substrates. *Physical Review Letters*, 59(5):555–558, 1987.

[18] J. K. Ferri and K. J. Stebe. Which surfactants reduce surface tension faster? A scaling argument for diffusion-controlled adsorption. *Advances in Colloid and Interface Science*, 85(1):61–97, 2000.

[19] D. Myers. *Surfaces, Interfaces and Colloids.* Wiley-VCH, New York, 1990.

[20] G. T. Barnes and I. R. Gentle. *Interfacial Science: An Introduction.* Oxford University Press, 2011.

[21] P. Mansky. Controlling polymer-surface interactions with random copolymer brushes. *Science*, 275(5305):1458–1460, 1997.

[22] V. Kumar, K. N. Bhat, and N. Nipun Sharma. Surface modification of textured silicon and its wetting behaviour. *Journal of Adhesion Science and Technology*, 29(4):308–318, 2015.

[23] D. H. Everett. *Basic Principles of Colloid Science.* Royal Society of Chemistry, London, 1988.

[24] D. F. Evans and H. Wennerström. *The Colloidal Domain Where Physics, Chemistry, Biology, and Technology Meet.* Wiley-VCH, New York, 1999.

[25] M. D. Haw. Colloidal suspensions, Brownian motion, molecular reality: A short history. *Journal of Physics: Condensed Matter*, 14(33):7769, 2002.

[26] A. Einstein. Über die von der molekularkinetischen theorie der wärme geforderte bewegung von in ruhenden flüssigkeiten suspendierten teilchen. *Annalen der Physik*, 322(8):549–560, 1905.

[27] R. Kubo. Brownian motion nonequilibrium statistical mechanics. *Science*, 233(4761):330–334, 1986.

[28] J. Perrin. Mouvement brownien et réalité moléculaire. *Annales de Chimie et de Physique*, 18:5–104, 1909.

[29] J. Perrin. *Les Atomes*. Librairie Félix Alcan, Paris, 1913.

[30] W. Poon. Colloids as big atoms. *Science*, 304(5672):830–831, 2004.

[31] H. N. W. Lekkerkerker and R. Tuinier. *Colloids and the Depletion Interaction*, volume 833. Springer, Heidelberg, 2011.

[32] D. G. A. L. Aarts, M. Schmidt, and H. N. W. Lekkerkerker. Direct visual observation of thermal capillary waves. *Science*, 304(5672):847–850, 2004.

[33] D. G. A. L. Aarts and H. N. W. Lekkerkerker. Confocal scanning laser microscopy on fluid-fluid demixing colloid-polymer mixtures. *Journal of Physics: Condensed Matter*, 16(38):S4231–S4242, 2004.

[34] S. A. Setu. *Interfacial Instabilities and Wetting Behaviour in Confinement*. PhD thesis, 2014.

[35] H. N. W. Lekkerkerker, V. W. A. de Villeneuve, J. W. J. de Folter, M. Schmidt, Y. Hennequin, D. Bonn, J. O. Indekeu, and D. G. A. L. Aarts. Life at ultralow interfacial tension: wetting, waves and droplets in demixed colloid-polymer mixtures. *The European Physical Journal B*, 64(3-4):341–347, 2008.

[36] D. G. A. L. Aarts, J. H. van der Wiel, and H. N. W. Lekkerkerker. Interfacial dynamics and the static profile near a single wall in a model colloid polymer mixture. *Journal of Physics: Condensed Matter*, 15(1):S245–S250, 2003.

[37] E. A. G. Jamie, G. J. Davies, M. D. Howe, R. P. A. Dullens, and D. G. A. L. Aarts. Thermal capillary waves in colloid-polymer mixtures in water. *Journal of Physics: Condensed Matter*, 20:494231, 2008.

[38] D. G. A. L. Aarts. The interface in demixed colloid-polymer systems: Wetting, waves and droplets. *Soft Matter*, 3:19, 2007.

[39] E. Kumacheva, O. Kalinina, and L. Lilge. Three-dimensional arrays in polymer nanocomposites. *Advanced Materials*, 11(3):231–234, 1999.

[40] G. Bosma, C. Pathmamanoharan, E. H. A. de Hoog, W. K. Kegel, A. van Blaaderen, and H. N. W. Lekkerkerker. Preparation of monodisperse, fluorescent PMMA-latex colloids by dispersion polymerization. *Journal of Colloid and Interface Science*, 245(2):292 – 300, 2002.

[41] G. H. Koenderink, S. Sacanna, D. G. A. L. Aarts, and A. P. Philipse. Rotational and translational diffusion of fluorocarbon tracer spheres in semidilute xanthan solutions. *Physical Review E - Statistical, Nonlinear, and Soft Matter Physics*, 69:1–12, 2004.

[42] E. A. G. Jamie, H. H. Wensink, and D. G. A. L. Aarts. Probing the critical behavior of colloidal interfaces by gravity. *Soft Matter*, 6(2):250–255, 2010.

[43] E. A. G. Jamie. *Colloidal Interfaces in Confinement*. PhD thesis, 2011.

[44] A. W. C. Lau, A. Prasad, and Z. Dogic. Condensation of isolated semi-flexible filaments driven by depletion interactions. *Europhysics Letters (EPL)*, 87(4):48006, 2009.

[45] T. Sanchez, D. T. N. Chen, S. J. DeCamp, M. Heymann, and Z. Dogic. Spontaneous motion in hierarchically assembled active matter. *Nature*, 491(7424):431–4, 2012.

[46] S. S. Silva, R. A. S. Ferreira, L. Fu, L. D. Carlos, J. F. Mano, R. L. Reis, and J. Rocha. Functional nanostructured chitosansiloxane hybrids. *Journal of Materials Chemistry*, 15(35-36):3952, 2005.

[47] M. V. von Smoluchowski. Molekularkinetische theorie der opaleszenz von gasen im kritischen zustand, sowie einiger verwandter erscheinungen. *Ann. Phys.*, 330:205–226, 1908.

[48] L. Mandelstam. Über die rauhigkeit freier flüssigkeitsoberflächen. *Ann. Phys.*, 25:609–624, 1913.

[49] E. A. G. Jamie, G. J. Davies, M. D. Howe, R. P. A. Dullens, and D. G. A. L. Aarts. Thermal capillary waves in colloid-polymer mixtures in water. *Journal of Physics: Condensed Matter*, 20:494231, 2008.

[50] V. W. A. de Villeneuve, J. M. J. van Leeuwen, J. W. J. de Folter, D. G. A. L. Aarts, W. van Saarloos, and H. N. W. Lekkerkerker. Residence and waiting times of Brownian interface fluctuations. *Europhysics Letters*, 81(6):60004, 2008.

[51] V. Prasad, D. Semwogerere, and E. R. Weeks. Confocal microscopy of colloids. *Journal of Physics: Condensed Matter*, 19(11):113102, 2007.

[52] M. Minsky. Memoir on inventing the confocal scanning microscope. *Scanning*, 10:128–138, 1988.

[53] T. Wilson. Resolution and optical sectioning in the confocal microscope. *Journal of Microscopy*, 244(2):113–121, 2011.

[54] T. Wilson. *Confocal Microscopy*. Academic Press, London, 1990.

[55] S. W. Paddock. Principles and practices of laser scanning confocal microscopy. *Molecular Biotechnology*, 16(2):127–150, 2000.

[56] R. H. Webb. Confocal optical microscopy. *Reports on Progress in Physics*, 59(3):427–471, 1999.

[57] R. P. A. Dullens. *Structure and Dynamics of Colloidal Hard Spheres in Real-space*. PhD thesis, 2005.

[58] J. J. Cras, C. A. Rowe-Taitt, D. A. Nivens, and F. S. Ligler. Comparison of chemical cleaning methods of glass in preparation for silanization. *Biosensors and Bioelectronics*, 14:683–688, 1999.

[59] C. Haensch, S. Hoeppener, and U. S. Schubert. Chemical modification of self-assembled silane based monolayers by surface reactions. *Chemical Society Reviews*, 39(6):2323, 2010.

[60] A. Ulman. Formation and structure of self-assembled monolayers. *Chemical Reviews*, 96(4):1533–1554, 1996.

[61] W. C. Bigelow, D. L. Pickett, and W. A. Zisman. Oleophobic monolayers: Films adsorbed from solution in non-polar liquids. *Journal of Colloid Science*, 1(6):513–538, 1946.

[62] E. G. Shafrin and W. A. Zisman. Hydrophobic monolayers adsorbed from aqueous solutions. *Journal of Colloid Science*, 4(6):571–590, 1949.

[63] J. Sagiv. Organized monolayers by adsorption: Formation and structure of oleophobic mixed monolayers on solid surfaces. *Journal of the American Chemical Society*, 399(1976):92–98, 1980.

[64] N. K. Chaki and K. Vijayamohanan. Self-assembled monolayers as a tunable platform for biosensor applications. *Biosensors and Bioelectronics*, 17(1-2):1–12, 2002.

[65] P. Silberzan, L. Leger, D. Ausserre, and J. J. Benattar. Silanation of silica surfaces: A new method of constructing pure or mixed monolayers. *Langmuir*, 7(8):1647–1651, 1991.

[66] A. Ulman. Self-assembled monolayers of alkyltrichiorosilanes: Building blocks for future organic materials. *Advanced Materials*, 2(12):573–582, 1990.

[67] R. Banga, J. Yarwood, A. M. Morgan, B. Evans, and J. Kells. FTIR and AFM studies of the kinetics and self-assembly of alkyltrichlorosilanes and (perfluoroalkyl)trichlorosilanes onto glass and silicon. *Langmuir*, 11(11):4393–4399, 1995.

[68] C. D. Bain and G. M. Whitesides. Modeling organic surfaces with self-assembled monolayers. *Advanced Materials*, 1(4):110–116, 1989.

[69] J. P. S. Farinha, M. A. Winnik, and K. G. Hahn. Characterization of oil droplets under a polymer film by laser scanning confocal fluorescence microscopy. *Langmuir*, 16(7):3391–3400, 2000.

[70] L.-H. Lee. Wettability and conformation of reactive polysiloxanes. *Journal of Colloid and Interface Science*, 27(4):751–760, 1968.

[71] B. Zhao and W. J. Brittain. Polymer brushes: Surface-immobilized macromolecules. *Progress in Polymer Science*, 25(5):677–710, 2000.

[72] W. J. Brittain and S. Minko. A structural definition of polymer brushes. *Journal of Polymer Science, Part A: Polymer Chemistry*, 45(16):3505–3512, 2007.

[73] J. N. Israelachvili. *Intermolecular and Surface Forces*. Academic Press, London, 1992.

[74] B. Zdyrko and I. Luzinov. Polymer brushes by the "grafting to" method. *Macromolecular Rapid Communications*, 32(12):859–869, 2011.

[75] R. A. L. Jones and R. W. Richards. *Polymers at Surfaces and Interfaces*. Cambridge University Press, 1999.

[76] P. G. de Gennes. Conformations of polymers attached to an interface. *Macromolecules*, 13(19):1069–1075, 1980.

[77] B. V. Derjaguin and L. Landau. Theory of the stability of strongly charged lyophobic sols and of the adhesion of strongly charged particles in solutions of electrolytes. *Acta Physicochim URSS*, 14:633–662, 1941.

[78] E. J. W. Verwey and J. T. G. Overbeek. *Theory of the Stability of Lyophobic Colloids*. Elsevier, 1948.

[79] S. B. Johnson, G. V. Franks, P. J. Scales, D. V. Boger, and T. W. Healy. Surface chemistry-rheology relationships in concentrated mineral suspensions. *International Journal of Mineral Processing*, 58(1-4):267–304, 2000.

[80] A Vrij. Polymers at interfaces and the interactions in colloidal dispersions. *Pure and Applied Chemistry*, 48:471–483, 1976.

[81] P. Atkins and J. de Paula. *Physical Chemistry*. Oxford University Press, 9th edition, 2010.

[82] S. Asakura and F. Oosawa. Surface tension of high-polymer solutions on interaction between two bodies immersed in a solution of macromolecules. *The Journal of Chemical Physics*, 22:1255–1256, 1954.

[83] S. Asakura and F. Oosawa. Interaction between particles suspended in solutions of macromolecules. *Journal of Polymer Science*, 33(126):183–192, 1958.

[84] H. N. W. Lekkerkerker, W. C.-K. Poon, P. N. Pusey, A. Stroobants, and P. B. Warren. Phase behaviour of colloid + polymer mixtures. *Europhysics Letters (EPL)*, 20(6):559–564, 1992.

[85] S. M. Ilett, A. Orrock, W. C.-K. Poon, and P. N. Pusey. Phase behavior of a model colloid-polymer mixture. *Physical Review E*, 51(2):1344–1352, 1995.

[86] R. Tuinier, D. G. A. L. Aarts, H. H. Wensink, and H. N. W. Lekkerkerker. Pair interaction and phase separation in mixtures of colloids and excluded volume polymers. *Physical Chemistry Chemical Physics*, 5(17):3707, 2003.

[87] A. A. Louis, P. G. Bolhuis, J. P. Hansen, and E. J. Meijer. Can polymer coils be modeled as soft colloids?. *Physical Review Letters*, 85(12):2522–2525, 2000.

[88] B. J. Kirby, A. R. Wheeler, R. N. Zare, J. A. Fruetel, and T. J. Shepodd. Programmable modification of cell adhesion and zeta potential in silica microchips. *Lab on a Chip*, 3(1):5–10, 2003.

[89] J. Horvath and V. Dolník. Polymer wall coatings for capillary electrophoresis. *Electrophoresis*, 22(4):644–655, 2001.

[90] A. Cifuentes, P. Canalejas, and J. C. Diez-Masa. Preparation of linear polyacrylamide-coated capillaries: Study of the polymerization process and its effect on capillary electrophoresis performance. *Instrumentation*, 830:423–438, 1999.

[91] L. Gao and S. R. Liu. Cross-linked polyacrylamide coating for capillary isoelectric focusing. *Analytical Chemistry*, 76(24):7179–7186, 2004.

[92] S. Wu and R. A. Shanks. Solubility study of polyacrylamide in polar solvents. *Journal of Applied Polymer Science*, 93(3):1493–1499, 2004.

[93] A. F. Hollander, P. Somasundaran, and C. C. Gryte. Adsorption characteristics of polyacrylamide and sulfonate-containing polyacrylamide copolymers on sodium kaolinite. *Journal of Applied Polymer Science*, 26(7):2123–2138, 1981.

[94] S. Hjertén. High-performance electrophoresis. *Journal of Chromatography A*, 347:191–198, 1985.

[95] H. Engelhardt and M. A. Cuñat-Walter. Preparation and stability tests for polyacrylamide-coated capillaries for capillary electrophoresis. *Journal of Chromatography A*, 716(1-2):27–33, 1995.

[96] X. Huang, L. J. Doneski, and M. J. Wirth. Surface-confined living radical polymerization for coatings in capillary electrophoresis. *Analytical Chemistry*, 70(19):4023–4029, 1998.

[97] J. J. Lu and S. Liu. A robust cross-linked polyacrylamide coating for microchip electrophoresis of dsDNA fragments. *Electrophoresis*, 27(19):3764–3771, 2006.

[98] J. J. Lu, S. Wang, G. Li, W. Wang, Q. Pu, and S. Liu. Chip-capillary hybrid device for automated transfer of sample preseparated by capillary isoelectric focusing to parallel capillary gel electrophoresis for two-dimensional protein separation. *Analytical Chemistry*, 84(16):7001–7007, 2012.

[99] M. Huang, W. P. Vorkink, and M. L. Lee. High efficiency cross-linked polyacrylamide coating for capillary electrophoresis of proteins. *Journal of Microcolumn Separations*, 4(3):233–238, 1992.

[100] J. R. Lovett, L. A. Fielding, S. P. Armes, and R. Buxton. One-pot preparation of conducting polymer-coated silica particles: Model highly absorbing aerosols. *Advanced Functional Materials*, 24(9):1290–1299, 2014.

[101] E. Bourgeat-Lami and J. Lang. Encapsulation of inorganic particles by dispersion polymerization in polar media. *Journal of Colloid and Interface Science*, 210(2):281–289, 1999.

[102] B. J. Maranzano, N. J. Wagner, G. Fritz, and O. Glatter. Surface charge of 3-(trimethoxysilyl) propyl methacrylate (TPM) coated Stöber silica colloids by zeta-phase analysis light scattering and small angle neutron scattering. *Langmuir*, 16(26):10556–10558, 2000.

[103] A. P. Philipse and A. Vrij. Preparation and properties of nonaqueous model dispersions of chemically modified, charged silica spheres. *Journal of Colloid and Interface Science*, 128(1):121–136, 1989.

[104] J. Z. Du and Y. M. Chen. Atom-transfer radical polymerization of a reactive monomer: 3-(Trimethoxysilyl)propyl methacrylate. *Macromolecules*, 37(17):6322–6328, 2004.

[105] J. B. Brzoska, I. Ben Azouz, and F. Rondelez. Silanization of solid substrates: A step toward reproducibility. *Langmuir*, 10(11):4367–4373, 1994.

[106] F. Bauer, H. Ernst, U. Decker, M. Findeisen, H. Gläsel, H. Langguth, E. Hartmann, R. Mehnert, and C. Peuker. Preparation of scratch and abrasion resistant polymeric nanocomposites by monomer grafting onto nanoparticles: FTIR and multi-nuclear NMR spectroscopy to the characterization of methacryl grafting. *Macromolecular Chemistry and Physics*, 201(18):2654–2659, 2000.

[107] I. Fundeanu, H. C. van der Mei, A. J. Schouten, and H. J. Busscher. Polyacrylamide brush coatings preventing microbial adhesion to silicone rubber. *Colloids and Surfaces B: Biointerfaces*, 64(2):297–301, 2008.

[108] I. Cringus-Fundeanu, J. Luijten, H. C. van der Mei, H. J. Busscher, and A. J. Schouten. Synthesis and characterization of surface-grafted polyacrylamide brushes and their inhibition of microbial adhesion. *Langmuir*, 23(9):5120–5126, 2007.

[109] T. Wu, K. Efimenko, and J. Genzer. Combinatorial study of the mushroom-to-brush crossover in surface anchored polyacrylamide. *Journal of the American Chemical Society*, 124(32):9394–9395, 2002.

[110] T. Wu, K. Efimenko, P. Vlěek, V. Šubr, and J. Genzer. Formation and properties of anchored polymers with a gradual variation of grafting densities on flat substrates. *Macromolecules*, 36(7):2448–2453, 2003.

[111] J. Bai, Y. Li, J. Du, S. Wang, J. Zheng, Q. Yang, and X. Chen. One-pot synthesis of polyacrylamide-gold nanocomposite. *Materials Chemistry and Physics*, 106(2-3):412–415, 2007.

[112] X. Lu and Y. Mi. Characterization of the interfacial interaction between polyacrylamide and silicon substrate by Fourier Transform Infrared Spectroscopy. *Macromolecules*, 38(3):839–843, 2005.

[113] M. Wiśniewska, S. Chibowski, and T. Urban. Impact of anionic and cationic polyacrylamide on the stability of aqueous alumina suspensioncomparison of adsorption mechanism. *Colloid and Polymer Science*, 293(4):1171–1179, 2015.

[114] Y.-C. Wang, S.-H. Kao, and H.-J. Hsieh. A chemical surface modification of chitosan by glycoconjugates to enhance the cell-biomaterial interaction. *Biomacromolecules*, 4(2):224–31, 2003.

[115] Y. Zhang, X. Zhang, R. Ding, J. Zhang, and J. Liu. Determination of the degree of deacetylation of chitosan by potentiometric titration preceded by enzymatic pretreatment. *Carbohydrate Polymers*, 83(2):813–817, 2011.

[116] N. Balázs and P. Sipos. Limitations of pH-potentiometric titration for the determination of the degree of deacetylation of chitosan. *Carbohydrate Research*, 342(1):124–130, 2007.

[117] T. Wu and S. Zivanovic. Determination of the degree of acetylation (DA) of chitin and chitosan by an improved first derivative UV method. *Carbohydrate Polymers*, 73(2):248–253, 2008.

[118] R. A. A. Muzzarelli. Biochemical significance of exogenous chitins and chitosans in animals and patients. *Carbohydrate Polymers*, 20(1):7–16, 1993.

[119] E. I. Rabea, M. E.-T. Badawy, C. V. Stevens, G. Smagghe, and W. Steurbaut. Chitosan as antimicrobial agent: Applications and mode of action. *Biomacromolecules*, 4(6):1457–1465, 2003.

[120] J. D. Bumgardner, R. Wiser, P. D. Gerard, P. Bergin, B. Chestnutt, M. Marin, V. Ramsey, S. H. Elder, and J. A. Gilbert. Chitosan: Potential use as a bioactive coating for orthopaedic and craniofacial/dental implants. *Journal of Biomaterials Science. Polymer Edition*, 14(5):423–438, 2003.

[121] H.-S. Lee, M. Q. Yee, Y. Y. Eckmann, N. J. Hickok, D. M. Eckmann, and R. J. Composto. Reversible swelling of chitosan and quaternary ammonium modified chitosan brush layers: Effect of pH and counter anion size and functionality. *Journal of Materials Chemistry*, 22(37):19605–19616, 2012.

[122] C. K. S. Pillai, W. Paul, and C. P. Sharma. Chitin and chitosan polymers: Chemistry, solubility and fiber formation. *Progress in Polymer Science*, 34(7):641–678, 2009.

[123] M. Rinaudo, G. Pavlov, and J. Desbrières. Influence of acetic acid concentration on the solubilization of chitosan. *Polymer*, 40(25):7029–7032, 1999.

[124] G. F. Payne and S. R. Raghavan. Chitosan: A soft interconnect for hierarchical assembly of nano-scale components. *Soft Matter*, 3(5):521, 2007.

[125] V. Tangpasuthadol, N. Pongchaisirikul, and V. P. Hoven. Surface modification of chitosan films. *Carbohydrate Research*, 338:937–942, 2003.

[126] G. A. Morris, J. Castile, A. Smith, G. G. Adams, and S. E. Harding. Macromolecular conformation of chitosan in dilute solution: A new global hydrodynamic approach. *Carbohydrate Polymers*, 76(4):616–621, 2009.

[127] H. Yi, L. Q. Wu, W. E. Bentley, R. Ghodssi, G. W. Rubloff, J. N. Culver, and G. F. Payne. Biofabrication with chitosan. *Biomacromolecules*, 6(6):2881–2894, 2005.

[128] K. Kurita. Controlled functionalization of the polysaccharide chitin. *Progress in Polymer Science*, 26(9):1921–1971, 2001.

[129] A. Subramanian, A. V. Rau, and H. Kaligotla. Surface modification of chitosan for selective surface-protein interaction. *Carbohydrate Polymers*, 66(3):321–332, 2006.

[130] C. Sanchez, F. Ribot, and B. Lebeau. Molecular design of hybrid organic-inorganic nanocomposites synthesized via sol-gel chemistry. *Journal of Materials Chemistry*, 9(1):35–44, 1999.

[131] V. P. Hoven, V. Tangpasuthadol, Y. Angkitpaiboon, N. Vallapa, and S. Kiatkamjornwong. Surface-charged chitosan: Preparation and protein adsorption. *Carbohydrate Polymers*, 68(1):44–53, 2007.

[132] X. Lü, W. Cui, Y. Huang, Y. Zhao, and Z. Wang. Surface modification on silicon with chitosan and biological research. *Biomedical Materials*, 4(4):044103, 2009.

[133] H. S. Lee, D. M. Eckmann, D. Lee, N. J. Hickok, and R. J. Composto. Symmetric pH-dependent swelling and antibacterial properties of chitosan brushes. *Langmuir*, 27(20):12458–12465, 2011.

[134] S. Boddohi, C. E. Killingsworth, and M. J. Kipper. Polyelectrolyte multilayer assembly as a function of pH and ionic strength using the polysaccharides chitosan and heparin. *Biomacromolecules*, 9(7):2021–2028, 2008.

[135] D. G. A. L. Aarts, R. P. A. Dullens, H. N. W. Lekkerkerker, D. Bonn, and R. van Roij. Interfacial tension and wetting in colloid-polymer mixtures. *The Journal of Chemical Physics*, 120(4):1973, 2004.

[136] J. M. Brader, R. Evans, M. Schmidt, and H. Löwen. Entropic wetting and the fluid-fluid interface of a model colloid-polymer mixture. *Journal of Physics: Condensed Matter*, 14(1):L1–L8, 2002.

[137] J. M. Brader, M. Dijkstra, and R. Evans. Inhomogeneous model colloid-polymer mixtures: Adsorption at a hard wall. *Physical Review E*, 63(4):041405, 2001.

[138] J. O. Indekeu, D. G. A. L. Aarts, H. N. W. Lekkerkerker, Y. Hennequin, and D. Bonn. Thermal fluctuation forces and wetting layers in colloid-polymer mixtures: Derivation of an interface potential. *Physical Review E - Statistical, Nonlinear, and Soft Matter Physics*, 81(4):1–12, 2010.

[139] W. K. Wijting, N. A. M. Besseling, and M. A. Cohen Stuart. Wetting in a colloidal liquid-gas system. *Physical Review Letters*, 90(19):196101, 2003.

[140] W. K. Wijting, N. A. M. Besseling, and M. A. Cohen Stuart. Wetting behavior in colloid-polymer mixtures at different substrates. *The Journal of Physical Chemistry B*, 107(38):10565–10570, 2003.

[141] M. Dijkstra, J. M. Brader, and R. Evans. Phase behaviour and structure of model colloid-polymer mixtures. *Journal of Physics: Condensed Matter*, 11(50):10079–10106, 1999.

[142] M. Dijkstra and R. van Roij. Entropic wetting and many-body induced layering in a model colloid-polymer mixture. *Physical Review Letters*, 89(1):208303, 2002.

[143] P. G. Bolhuis, A. A. Louis, and J. P. Hansen. Influence of polymer-excluded volume on the phase-behavior of colloid-polymer mixtures. *Physical Review Letters*, 89(12):1283021–1283024, 2002.

[144] P. G. Bolhuis, E. J. Meijer, and A. A. Louis. Colloid-polymer mixtures in the protein limit. *Physical Review Letters*, 90(6):068304, 2003.

[145] D. G. A. L. Aarts, R. Tuinier, and H. N. W. Lekkerkerker. Phase behavior of mixtures of colloidal spheres and excluded-volume polymer chains. *Journal of Physics: Condensed Matter*, 14:7551–7561, 2002.

[146] J. M. Brader and R. Evans. The fluid-fluid interface of a model colloid-polymer mixture. *Europhysics Letters (EPL)*, 49:678–684, 2000.

[147] E. H. A. de Hoog and H. N. W. Lekkerkerker. Measurement of the interfacial tension of a phase-separated colloid-polymer suspension. *The Journal of Physical Chemistry B*, 103(25):5274–5279, 1999.

[148] E. M. Blokhuis and J. Kuipers. Wetting reversal in colloid-polymer systems. *Physical Review E - Statistical, Nonlinear, and Soft Matter Physics*, 81(5), 2010.

[149] Y. Hennequin, D. G. A. L. Aarts, J. O. Indekeu, H. N. W. Lekkerkerker, and D. Bonn. Fluctuation forces and wetting layers in colloid-polymer mixtures. *Physical Review Letters*, 100(17):2–5, 2008.

[150] J. Koning, Y. Hennequin, D. Bonn, and J. Indekeu. Contact line of adsorbed colloid-polymer droplets in theory and experiment. *Soft Matter*, 12:4052–4058, 2016.

[151] J. Koning, Y. Vandecan, and J. Indekeu. Theoretical study of line and boundary tension in adsorbed colloid-polymer mixtures. *Journal of Chemical Physics*, 141(4):1–11, 2014.

[152] Y. Vandecan and J. Indekeu. Theoretical study of the three-phase contact line and its tension in adsorbed colloid-polymer mixtures. *Journal of Chemical Physics*, 128(10), 2008.

[153] C. Huh and R. L. Reed. A method for estimating interfacial tensions and contact angles from sessile and pendant drop shapes. *Journal of Colloid and Interface Science*, 91(2):472–484, 1983.

[154] A. S. Dimitrov, P. A. Kralchevsky, A. D. Nikolov, H. Noshi, and M. Matsumoto. Contact angle measurements with sessile drops and bubbles. *Journal of Colloid and Interface Science*, 145(1):279–282, 1991.

[155] C. W. Extrand and Y. Kumagai. Contact angles and hysteresis on soft surfaces. *Journal of Colloid and Interface Science*, 184(1):191–200, 1996.

[156] D. Quere, M. Azzopardi, and L. Delattre. Drops at rest on a tilted plane. *Langmuir*, 14(97):2213–2216, 1998.

[157] A. F. Stalder, T. Melchior, M. Müller, D. Sage, T. Blu, and M. Unser. Low-bond axisymmetric drop shape analysis for surface tension and contact angle measurements of sessile drops. *Colloids and Surfaces A: Physicochemical and Engineering Aspects*, 364(1-3):72–81, 2010.

[158] M. Schmitt and F. Heib. High-precision drop shape analysis on inclining flat surfaces: Introduction and comparison of this special method with commercial contact angle analysis. *The Journal of Chemical Physics*, 139(13):134201, 2013.

[159] C. W. Extrand. Uncertainty in contact angle measurements from the tangent method. *Journal of Adhesion Science and Technology*, 30(15):1597–1601, 2016.

[160] E. Atefi, J. A. Mann, and H. Tavana. A robust polynomial fitting approach for contact angle measurements. *Langmuir*, 29(19):5677–5688, 2013.

[161] Y. Rotenberg, L. Boruvka, and A. W. Neumann. Determination of surface tension and contact angle from the shapes of axisymmetric fluid interfaces. *Journal of Colloid and Interface Science*, 93(1):169–183, 1983.

[162] J. K. Spelt, Y. Rotenberg, D. R. Absolom, and A. W. Neumann. Sessile-drop contact angle measurements using axisymmetric drop shape analysis. *Colloids and Surfaces*, 24(2-3):127–137, 1987.

[163] P. Cheng, D. Li, L. Boruvka, Y. Rotenberg, and A. W. Neumann. Automation of axisymmetric drop shape analysis for measurements of interfacial tensions and contact angles. *Colloids and Surfaces*, 43(2):151–167, 1990.

[164] D. G. A. L. Aarts, R. P. A. Dullens, and H. N. W. Lekkerkerker. Interfacial dynamics in demixing systems with ultralow interfacial tension. *New Journal of Physics*, 7:40–40, 2005.

[165] E. A. G. Jamie, R. P. A. Dullens, and D. G. A. L. Aarts. Surface effects on the demixing of colloid-polymer systems. *Journal of Physical Chemistry B*, 115(45):13168–13174, 2011.

[166] D. Bonn and D. Ross. Wetting transitions. *Reports on Progress in Physics*, 64(9):1085–1163, 2001.

[167] J. O. Indekeu. Introduction to wetting phenomena. *Acta Physica Polonica B*, 26:1065, 1995.

[168] J. W. Cahn. Critical point wetting. *The Journal of Chemical Physics*, 66(8):3667, 1977.

[169] E. M. Blokhuis. Wetting. In *Lecture Notes: Han-sur-Lesse Winter School*. Belgium, 2000.

[170] M. R. Moldover and J. W. Cahn. An interface phase transition: Complete to partial wetting. *Science*, 207(4435):1073–1075, 1980.

[171] E. A. G. Jamie, H. H. Wensink, and D. G. A. L. Aarts. Probing the critical behavior of colloidal interfaces by gravity. *Soft Matter*, 6(2):250–255, 2010.

[172] E. A. G. Jamie, R. P. A. Dullens, and D. G. A. L. Aarts. Fluid-fluid demixing of off-critical colloid-polymer systems confined between parallel plates. *Journal of Physics. Condensed Matter : an Institute of Physics Journal*, 24(28):284120, 2012.

[173] P. P. F. Wessels, M. Schmidt, and H. Löwen. The contact angle of the colloidal liquid-gas interface and a hard wall. *Journal of Physics: Condensed Matter*, 16(38):S4169–S4184, 2004.

[174] C. Rascón, A. O. Parry, and D. G. A. L. Aarts. Geometry-induced capillary emptying. *Proceedings of the National Academy of Sciences*, 113(45):12633–12636, 2016.

[175] M. C. Stewart and R. Evans. Wetting and drying at a curved substrate: Long-ranged forces. *Physical Review E*, 71(1):011602, 2005.

[176] B. P. Binks and T. S. Horozov, editors. *Colloidal Particles at Liquid Interfaces*. Cambridge University Presss, Cambridge, 2006.

[177] R. Aveyard, B. P. Binks, and J. H. Clint. Emulsions stabilised solely by colloidal particles. *Advances in Colloid and Interface Science*, 100-102:503–546, 2003.

[178] S. U. Pickering. Emulsions. *J. Chem. Soc., Trans.*, 91:2001–2021, 1907.

[179] P. Finkle, H. D. Draper, and J. H. Hildebrand. The theory of emulsification. *Journal of the American Chemical Society*, 45(12):2780–2788, 1923.

[180] B. P. Binks. Particles as surfactants: Similarities and differences. *Current Opinion in Colloid and Interface Science*, 7(1-2):21–41, 2002.

[181] B. P. Binks and J. H. Clint. Solid wettability from surface energy components: Relevance to pickering emulsions. *Langmuir*, 18(4):1270–1273, 2002.

[182] H. Tanaka, A. J. Lovinger, and D. D. Davis. Pattern evolution caused by dynamic coupling between wetting and phase separation in binary liquid mixture containing glass particles. *Physical Review Letters*, 72(16):2581–2584, 1994.

[183] A. O. Parry and C. Rascón. Scaling properties of fluid adsorption near the base of a cylinder. *Physical Review E - Statistical, Nonlinear, and Soft Matter Physics*, 85(3):1–11, 2012.

List of Publications

To date the following publications based upon work in this thesis are to be submitted or are in preparation:

Huzaifah H. Abdul Razak, Kira E. Klop, Roel P. A. Dullens, Andrew O. Parry, Carlos Rascón and Dirk G. A. L. Aarts. *Droplets of phase-separated colloid-polymer mixtures at polymer-coated walls.* Soft Matter. To be submitted. (Chapter 4).

Huzaifah H. Abdul Razak, Roel P. A. Dullens and Dirk G. A. L. Aarts. *Wetting transition in colloid-polymer mixtures at polymer-coated walls.* Physical Review E. In preparation. (Chapter 5).

Huzaifah H. Abdul Razak, Adam E. Stones, Roel P. A. Dullens and Dirk G. A. L. Aarts. *Wetting of colloid-polymer mixtures at curved surfaces.* Soft Matter. In preparation. (Chapter 6).

Acknowledgements

In the name of Allah, the Most Gracious and the Most Merciful.

Alhamdulillah. All praises to Allah. For everything He has given me, words could never be enough.

I would like to express my sincere gratitude to my supervisor, Dirk Aarts, for his continuous support throughout my DPhil studies, for his guidance, patience, motivation and understanding. His encouragement, knowledge and ideas always inspire me to explore the experiments in a different way. I appreciate his style of supervision, making it enjoyable and productive to be in the lab, and in the group in general. He is a natural and high-spirited supervisor, and I wish him great success in his career. A huge thank you also to Roel Dullens, for always offering me additional guidance and encouragement when needed.

Special thanks to Carlos Rascón, Martin Grossel, Andrew Parry, Benoit Loppinet and Antonio Giuliani for our collaborations. All the discussions on the theory, as well as the experimental support, are highly appreciated. To Kira and Adam, I owe them a great deal. The analysis of the experimental data would not be actualised without their impressive knowledge and help in the theory.

Being in Oxford, and being a part of this group in particular, leaves wonderful memories for me. This beautiful place has helped me discover more about science, knowledge, and life. This is where I have met beautiful people with beautiful minds.

Special thanks goes to Kira, for all the discussions and help, on work and life, over the past years. My DPhil journey would definitely be different without her. I enjoy her company in the lab, especially when Mathematica does not cooperate with me, as well as the fun outside activities with her family. For the friendship, encouragement, intellectual and casual chats, and

boterkoek, I thank Kira.

I would also like to thank Lia for the tips and tricks in the synthesis of the colloid-polymer mixtures, and for her expertise in the microscopes. From her, I also gained more introduction to Dutch tradition and a friendship. Oli and Min are thanked for helping me to get started with microfluidics at the very beginning. Min has shown that the way to deal with the miniaturisation of experimental glassware is through patience.

I wish to thank the other members of the Aarts-Dullens group, past and present, who have made my time here memorable and meaningful, be it in the labs or the group outings, and especially the people I share the office with: Raam for being very helpful since I started the journey and for always offering the moral support during the writing up stage, Michael for extra encouraging words during my thesis writing, Adam for entertaining my theoretical questions, Mike, Paola, François, Colin, Julia, Yanyan, Josh, Siyu, Louis, and definitely to everyone else in the group, for being supportive and helpful.

This appreciation also extends to the other people in the department that have been very kind and helpful: Paul and Martin from Lab Services, the stores, Tom and John from IT Services, the workshop, Nita from the undergraduate teaching labs, Eleni the receptionist, and many other friendly people I get to know in the building and across the road.

My memories in Oxford is not complete without the mention of a good friend of mine, Nazri, who has been sharing the journey with me since the first day I arrived Oxford. I thank him for always being there for me, for all the intellectual discussions and sincere advice, for always being ready to laugh out loud and cracking more jokes, for motivating and for helping me looking at things in a simpler way. Equal thank goes to my good friend and confidante, Amalina, who is always ready to laugh at my jokes, as well as to listen to my deep thoughts, and for being very understanding and fun. I will always cherish all those good times together, from dining to shopping to just even chatting. For all the shared tears, joy and laughter started from Randolph House, I hope this friendship will continue for many years to come.

I would also like to thank my Malaysian friends: Raihan and Arshad, Hanis and Aizat, Min and Azad, Syarif and Hayati, Firdaus and Amana, Suzana and Azlan, Juliana, Najiah, and all the Malaysian students at the University of Oxford for always offering a helping hand to me, and for all the exciting weekend gatherings.

I am really grateful to have my sister, Rabeah, by my side during the final stages of my project. She has been a great help, a source of motivation, a partner for sisterly talks, and most importantly, to bring home here to me. If it was not for her, my final year would have been much more difficult. I wish her the very best in her DPhil journey, and I hope she will continue to enjoy Oxford as much as I have.

My parents are always the best gifts in my life. To my mother, Zainab Ismail, and father, Abdul Razak Jaafar, to whom my life is indebted to, thank you for all the prayers, unconditional love, support, sacrifices, encouragement, and faith in me. Thank you for being the greatest source of motivation and encouragement, for giving me the freedom to choose the life I want to be in, for encouraging me to stand out and be different, for shaping the way I think and react, and for bringing the best out of me. Without them, I would not be the person I am right now. A special mention also goes to my siblings, Maria, Rabeah, and Tariq, whom I share everything with. Thank you for the love and continuous support, for the ridiculous discussions and intellectual debates, for always putting up with me, and for making our home the best place to be. Lifting and encouraging one another has always been the secret to shining together, and I am grateful for that. I would like to extend my gratitude to my grandparents, for all the love, prayers and additional wisdom that make me feel complete. Thank you also to my brother-in-law, Azhar, for being a great family member and a loving father to my niece, Muazzah, and nephews, Muzakkir and Muazzir, who always putting a smile on my face. I am blessed to be in this family.

Last but not least, I would like to express my sincere gratitude to Majlis Amanah Rakyat Malaysia and St. Hilda's College for financial support. An extra warm thank you to everyone who has helped me in making this study a reality.

Thank you for always being with me, physically, or in spirit.

So which of the favours of
your Lord would you deny?
The Quran (55:13)